

**THE INTERACTION OF CALCIUM PHOSPHATE BASED CERAMICS  
PRODUCED VIA COMBUSTION SYNTHESIS  
WITH SIMULATED BODY FLUIDS.**

ARLENDA LAKES LIBRARY  
COLORADO SCHOOL OF MINES  
GOLDEN, CO 80401

**By**

**Guglielmo Gottoli**

ProQuest Number: 10794667

All rights reserved

INFORMATION TO ALL USERS

The quality of this reproduction is dependent upon the quality of the copy submitted.

In the unlikely event that the author did not send a complete manuscript and there are missing pages, these will be noted. Also, if material had to be removed, a note will indicate the deletion.



ProQuest 10794667

Published by ProQuest LLC (2018). Copyright of the Dissertation is held by the Author.

All rights reserved.

This work is protected against unauthorized copying under Title 17, United States Code  
Microform Edition © ProQuest LLC.

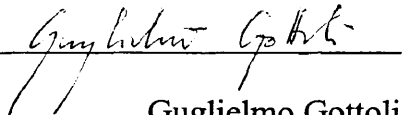
ProQuest LLC.  
789 East Eisenhower Parkway  
P.O. Box 1346  
Ann Arbor, MI 48106 – 1346

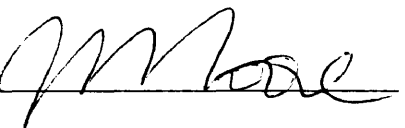


A thesis submitted to the Faculty and Board of Trustees of the Colorado School of Mines in partial fulfillment of the requirements for the degree of Master of Science (Materials Science).

Golden, Colorado

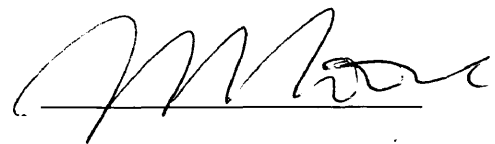
Date 10/29/02

Signed:   
Guglielmo Gottoli

Approved:   
Dr. John J. Moore  
Thesis Advisor

Golden, Colorado

Date 10/29/02

  
Dr. John J. Moore  
Professor and Head,  
Department of Metallurgical  
& Materials Engineering.

## ABSTRACT

For the last thirty years ceramic-based materials have been studied extensively for their bioactive nature i.e. their capacity to bond to bone without encapsulating connective tissue. It has been hypothesized that their bonding ability to living bone depends on the formation of a calcium phosphate (CaP) layer having a carbonate hydroxyapatite (HCA) structure on the surface. In addition, studies have demonstrated that the formation of these CaP layers is affected by the composition of the original constituents of the ceramic material.

These ceramics can be manufactured via the sintering or sol-gel routes. However, an alternative method is that of Self-Propagating High Temperature (Combustion) Synthesis (SHS). This new method promises to produce equivalent materials rapidly with no need of secondary processing. This has the considerable advantage for real-time, on-site production of personalized bone implants in the surgical ward. The work presented herein seeks to characterize five different calcium phosphate based ceramics produced via this method and elucidate their bioactivity when placed in a simulated body fluid (SBF).

The CaP materials manufactured via the SHS process were found to be very heterogeneous in phase constitution. The treatment in SBF was observed to have profound effects on the powder surfaces (except for the control system). The presence of globular agglomerations on these surfaces indicated the likelihood of an amorphous HCA

bioactive layer depositing. These features developed from both precipitation and dissolution reactions occurring at the material-SBF solution interface. The SBF treatment has thus proven that SHS-fabricated CaP compounds possess a high potential as bioactive materials for future biomedical applications.

## TABLE OF CONTENTS

<b>ABSTRACT.....</b>	<b>iii</b>
<b>LIST OF FIGURES.....</b>	<b>viii</b>
<b>LIST OF TABLES.....</b>	<b>xi</b>
<b>ACKNOWLEDGEMENTS.....</b>	<b>xiii</b>
<b>1. INTRODUCTION.....</b>	<b>1</b>
<b>2. LITERATURE RESEARCH.....</b>	<b>3</b>
2.1. Physical and chemical considerations in the degradation process of CaPs.....	4
2.2. Biological processes involved in the degradation of CaPs.....	6
2.3. The formation of the CaP layer and its bioactive function.....	9
2.4. The adsorption of proteins onto the HCA bioactive layer.....	11
2.5. Cell involvement and participation in the regeneration of new bone tissue.....	12
2.6. Analytical techniques adopted for the characterization of CaPs.....	13
2.7. Concluding remarks.....	16

<b>3. MATERIALS AND EXPERIMENTAL METHOD.....</b>	<b>18</b>
3.1. Sample Preparation.....	19
3.2. Characterization of the Powders.....	25
3.2.1. X-ray Diffraction Analysis.....	25
3.2.2. Fourier Transform Infrared Spectroscopy Analysis.....	26
3.2.3. Scanning Electron Microscopy Analysis.....	26
3.2.4. X-ray Photoelectron Spectroscopy Analysis.....	27
3.2.5. The Inductively Coupled Plasma Analysis.....	28
<b>4. RESULTS .....</b>	<b>29</b>
4.1. Scanning Electron Microscopy Analysis (SEM).....	29
4.1.1 The NT samples.....	29
4.1.2. The T samples.....	31
4.2. X-ray Diffraction Analysis (XRD).....	34
4.3. Fourier Transform Infrared Spectroscopy Analysis (FTIR).....	41
4.4. X-Ray Photoelectron Spectroscopy (XPS).....	48
4.5. Inductively Coupled Plasma (ICP).....	52
4.6. Electron Dispersive Spectroscopy (EDS).....	54
4.7. pH Data.....	56
4.8. Atomic Force Microscopy (AFM).....	58

<b>5. DISCUSSION AND CONCLUSIONS.....</b>	<b>60</b>
<b>6. FUTURE WORK.....</b>	<b>65</b>
<b>REFERENCES.....</b>	<b>67</b>

## **LIST OF APPENDICES**

<b>Appendix 1. SEM data.....</b>	<b>69</b>
<b>Appendix 2. XRD data. ....</b>	<b>74</b>
<b>Appendix 3. FTIR data. ....</b>	<b>83</b>
<b>Appendix 4. XPS data. ....</b>	<b>107</b>
<b>Appendix 5. ICP data. ....</b>	<b>117</b>
<b>Appendix 6. EDS data. ....</b>	<b>119</b>
<b>Appendix 7. AFM data. ....</b>	<b>129</b>

## LIST OF FIGURES

- Figure 3.1.** A schematic diagram of the Self-Propagating High-temperature Synthesis (SHS) reaction method.....20
- Figure 3.2.** Illustrates the five cylindrical pellets that result from the SHS reaction. The five CaP systems are numbered S1-S5 from left to right.....21
- Figure 3.3.** Illustrates a simple schematic of the general experimental set-up.....23
- Figure 4.1.** 10 SEM photomicrographs. The top five represent the non-treated (NT) systems S1 to S5. The bottom five represent the respective treated (T) systems. All micrographs were taken at 10,000x.....30
- Figure 4.2.** The empirical ranking system utilized to determine the globular agglomeration surface coverage of the CaP treated systems.....32
- Figure 4.3.** This XRD figure depicts peak matches for the S1 NT system .....36

**Figure 4.4.** This XRD figure depicts peak matches for the S5 NT system .....36

**Figure 4.5.** This XRD figure depicts peak matches for the S1 T system.....37

**Figure 4.6.** This XRD figure depicts peak matches for the S5 T system.....37

**Figure 4.7.** FTIR spectrum peak matches for the S2 NT sample.....43

**Figure 4.8.** FTIR spectrum peak matches for systems S2 T sample.....44

**Figure 4.9.** ICP analysis on the SBF solutions after the 10-day treatment [S1-S5 and the Control SBF].....52

**Figure 5.1.** EDS analysis performed on the S1 T sample. Mg and Cl ions confirm the presence of salts on the surface that crystallize from the SBF solution.....55



**Figure 5.2.** pH curves for S1-S5 during the 10-day SBF treatment.....56

**Figure 5.3. (a)** Shows the AFM analysis of a  $5 \times 5 \mu\text{m}^2$  area of the S3 NT system. **(b)** Is a structural representation of this analysis.....59

**Figure 5.4. Figure 5.3. (a)** AFM analysis of a  $1 \times 1 \mu\text{m}^2$  area of the S3 NT system. **(b)** Is a structural representation of this analysis.....59

## LIST OF TABLES

<b>Table 3.1.</b> The chemical constituents in each of the five CaP systems (S1 to S5) .....	19
<b>Table 3.2.</b> Illustrates the chemical constituents of the simulated body fluid (SBF) solution.....	22
<b>Table 4.1.</b> XRD peak matches for systems S1 and S5 T and NT samples. $\alpha$ -TCP matches were predominantly found with some apatitic peaks being present.....	35
<b>Table 4.2.</b> XRD peak matches for systems S2 to S4 T and NT samples. The tables attribute specific hkl peak values to certain phases that were identified in both NT and T samples. The material results in being very heterogeneous.....	38

**Table 4.3.** Wave number matches identified for specific chemical bond types and phases for standard FTIR values for S2. The NT, T and subtracted spectra values are also included. The areas highlighted in gray are the most significant and are representative of an A/B-type HCA structure.....42

**Table 4.4.** Atomic compositions of the CaP powders of both NT and T systems calculated from the wide scan data from XPS analysis.....49

## ACKNOWLEDGEMENTS

Due to the interdisciplinary nature of this research project, four departments of the Colorado School of Mines (CSM) have been involved. Different people in those departments have been very helpful and their role has been extremely appreciated.

In Materials Science, Dr. Kleebe, Giuliano Gregori, Bob McGrew together with Darin Aldrich have been very supportive and their collaboration has been extremely important during the phases of the Scanning Electron Microscopy (SEM) training and analysis.

In Physics, Dr. Williamson has given the author a first introduction to X-ray diffraction (XRD) analysis.

In Chemistry, Dr. Wildeman and his graduate students have kindly helped with the Inductively Coupled Plasma procedure, whilst Dr. Cowley was consulted for his Fourier Transform Infrared Spectroscopy expertise and training.

In Metallurgy, advice was sought from the following people: Dr. Olson and Dr. Martins for academic matters.

All the friends in the Center for Commercial Applications of Combustion in Space (CCACS) and Biomaterials Group have been an asset because of their culture and support. In particular, Douglas Burkes, Denise Belk, Martin Castillo, Xiaolan Zhang and Sheldon Newman. A Special “Grazie Mille” goes to the “Empress” Mindy Gewuerz.

Within the students of the materials science department a key figure was Douglas Burkes, who very patiently assisted the author with the experimental set-up and aspects of the completion of this project, not to mention numerous academic problems. This became the basis of a good friendship and professional relationship.

Last but not least, the author is very thankful to his research advisor Dr. John Moore, and the committee members Dr. Frank Schowengerdt and Dr. Reed Ayers.

Very important figures, not directly involved in the research, were the author's family members and friends such as Anne Dinan, Dottor Vincenzo Furfaro and the Leith Family.

A particular recognition is necessary for the opportunity that the sponsor CCACS has given the author to experience the world of biomaterials and space research at CSM. Two people have been vital in allowing the author to pursue these studies: Dr. Frank Schowengerdt and Dr. John Moore. Thank you once again!

## CHAPTER 1

### INTRODUCTION

Human calcified tissues in the form of bone and teeth are constituted primarily of a mineral crystalline phase of a deficient apatite: hydroxyapatite (HA) that possesses the following structural formula  $\text{Ca}_{10}(\text{PO}_4)_6(\text{OH})_2$ <sup>1</sup>. This phase contains variable proportions of hydrogen phosphate ( $\text{HPO}_4^{2-}$ ) and carbonate ( $\text{CO}_3^{2-}$ ) ions. During a normal healthy life these tissues undergo permanent transformations via a continuous remodeling process that allows bone to adapt to certain physiological constraints. This explains why we “change our skeleton” several times during the course of our existence. So sophisticated is this mechanism, that when particular pathological events arise, an alteration in this delicate equilibrium may result in the insufficient production of bone tissue. Two examples of these pathologies are: *Osteoporosis*.<sup>2</sup> In this diseased state, the organism reduces the overall amount of skeletal bone production resulting in bone fragility and multiple fractures for the patient. *Localized Bone Loss*. This results from localized trauma or from the insurgence of a bone tumor. The treatment of these illnesses are not straightforward, but are usually dealt with by either undertaking traditional medical therapies that increase the natural bone remodeling process or, by delivering alternative bone material to the damaged site to replace and consolidate the defiant bone<sup>2</sup>.

CaP based Biomaterials represent the hope for the above problems. In fact, HA and other members of the CaP family have been developed via diverse manufacturing routes for these very reasons. They can be directly implanted into bone and are generally well tolerated by undergoing two types of transformations: the degradation of the biomaterial itself and the colonization of the new bone tissue<sup>3,4</sup>.

Bearing this in mind, the aims of this study were multiple: firstly, to determine if the alternative manufacturing process of combustion synthesis can produce CaPs of equivalent biological properties to those manufactured via other routes. Secondly, to discover to what extent the constituents of these materials can affect the neo-formation of a specific CaP layer; very important in rendering a material bioactive. Finally, a clarification of the mechanistic aspects involved in both the biodegradation and bone tissue regeneration processes (previously studied by other authors) was attempted.

## CHAPTER 2

### LITERATURE RESEARCH

The following section has the intent of supplementing the reader with specific background information obtained from previous studies pertaining to CaP materials. It should help to gain an understanding of the mechanisms involved in both the physico-chemical and biological processes of degradation of these materials. Additional details of the neo-formation of a CaP layer in the *in-vitro* and *in-vivo* environments are given. Its importance in determining the bioactivity of a biomaterial is emphasized. Finally, aspects of the different characterization techniques are highlighted. An attempt to link the physico-chemical information obtained from them to other biological parameters is also discussed.



## 2.1. Physical and chemical considerations in the degradation process of CaPs.

This *Physico-chemical* degradation of CaPs is associated with both physical and chemical phenomena. It is related to the instability of these compounds to aqueous media. Various researchers have performed studies based on solubility measurements indicating HA as being the least soluble and hence the most stable of all CaP compounds<sup>5</sup>. Other phases identified in these materials such as: octacalcium phosphate (OCP), alpha tricalcium phosphate ( $\alpha$ -TCP) and beta tricalcium phosphate ( $\beta$ -TCP), transform into apatite as a result of hydrolytic action<sup>6</sup>. The rate of this transformation is determined by the surface area exposed to the aqueous media and by the solubility of each phase. Hence, the nature of each phase within a biomaterial is intimately linked with its physico-chemical degradation. However, additional factors, such as the environment to which the biomaterial is subjected e.g. local concentrations of calcium ( $\text{Ca}^{2+}$ ) and phosphate ( $\text{PO}_4^{3-}$ ) ions and pH, have been critical in determining the rate of dissolution/precipitation of CaP biomaterials<sup>7,8</sup>. *In-vivo* studies also have demonstrated the involvement of specific proteins in these processes because of their adsorption properties<sup>9-11</sup>.

Compositional differences in apatites seem to alter the solubility properties of these compounds<sup>12</sup>. The cohesiveness of CaPs can be attributed to the electrostatic interactions that occur between ions and to the presence/absence of certain vacancies within their structure. In the former case, the larger the ions incorporated into these CaP structures, the lower their stability and the higher their solubility. For example, strontium ( $\text{Sr}^{2+}$ ) ions

are known to substitute for  $\text{Ca}^{2+}$  ions in stoichiometric HA (S-HA) increasing its solubility. Conversely, when fluoride ( $\text{F}^-$ ) ions are substituted for hydroxide ( $\text{OH}^-$ ) ions, this reaction leads to less soluble apatites<sup>13</sup>. In the latter case, ionic vacancies have proven to decrease the material's structural stability, thus resulting in more soluble compounds. In addition, the decrease in ionic charge has also been found to have a similar effect<sup>14</sup>, for example, when carbonate ions substitute for phosphate ions<sup>14</sup>. This explains why non-stoichiometric HA (NS-HA) and carbonate containing apatites (HCA) are more susceptible to dissolution than S-HAs. These CaPs are therefore considered as “*non-resorbable*” biomaterials, whilst NS-HAs are not. A note should be made that there is always an exception to the rule, and in this case it would be for Whitlocktite. This CaP mineral has a  $\beta$ -TCP structure that contains a magnesium ( $\text{Mg}^{2+}$ ) ion impurity. Its presence considerably inhibits the hydrolysis of Whitlocktite rendering the material extremely insoluble.<sup>1,15</sup>

Finally, textural parameters such as surface topography and morphology, but more importantly porosity and crystal size can also dramatically affect the degradation behavior of CaP compounds. The size of the implant is an additional consideration that is often neglected. In fact, it has been observed that larger compact pieces will often degrade very slowly even if they are defined “biodegradable”.

## 2.2. Biological processes involved in the degradation of CaPs.

Biomaterials can also undergo biological degradation processes commonly known as “*biodegradation*”. The transformation of the material can occur via two types of cellular action: one involving osteoclasts and the other involving phagocytes.

One cellular mechanism is defined as an *osteoclastic resorption response*. Osteoclasts are giant multi-nucleated cells that are amongst the first protagonists to interact with a biomaterial surface. These cells perform a specific phagocytic action that degrades solely bone tissue. Their action involves producing an acidic environment (pH range 2-4) sufficient to dissolve any CaP compound (even those of the most insoluble nature e.g. HA).<sup>16</sup>

Shortly after implantation, CaPs suffer the direct consequences of this cellular action. Dicalcium phosphate dihydrate (DCPD) is the most stable CaP phase present in this situation. It has been suggested that CaP surfaces are covered by this phase during the initial stages of implantation<sup>17</sup>.

The parameters that induce the acidic dissolution of CaPs *in vivo* are identical to those mentioned previously in the physico-chemical degradation process section (i.e. the CaP composition, the nature of each phase, the non-stoichiometry of the apatites, the amount of exposed surface, porosity, particle size and the number of sites available for crystal dissolution etc). However, in biological environments, these parameters can differ resulting in changes in trends. For example CaP compounds like HA and  $\beta$ -TCP

(normally insoluble in aqueous media) become very unstable and bio-resorbable in these environments. The bio-response of these compounds in *in-vivo* situations substantially differs from *in-vitro* environments.

In the cellular dissolution process of multiphase CaP materials it has been observed that a preferential dissolution of the most soluble components occurs first, releasing particles that interact with other less soluble phases<sup>18</sup>. These small particles can in turn induce an inflammatory response that enhances even further the degradation phenomenon. In fact, the general trend is that the severity of the inflammatory response is inversely proportional to the size of the particle. Again, textural and crystal size factors remain important parameters to consider in this degenerative response. It has been suggested that the detachment of the CaP particles from the main core of an implant explains the poor attachment of real bone tissue to bone cements and implant surfaces several days after implantation.<sup>19</sup>

Another important cellular mechanism involved in the biodegradation process is known as *phagocytosis* and has been amply observed to occur for many biomaterial systems (whether of CaP origin or not). This mechanism differentiates itself from the prior one because of its more general action. The cells involved, (phagocytes) indiscriminately “digest” foreign particles that are either released from the immediate inflammatory response, or from more specific osteoclast cell actions. It is to be noted that, the latter cell-types are in essence a subset of phagocytes with very specific functions. However, phagocytosis is not always successful, as some of the more insoluble

CaPs are not easily “processed” by the phagocytes. This generally results in the initiation of the cell death mechanism termed Apoptosis.

### **2.3. The formation of the CaP layer and its bioactive function.**

Summarizing from above, all forms of CaP materials, to varying degrees offer the prospect of replacing bone in those pathological conditions where bone locally is insufficient. In order to become an interesting bone substitute, and depending on their application, these CaP materials must possess certain physico-chemical and biological properties. A complete knowledge of how these parameters are linked with mechanisms of biomineralization has not yet been completely elucidated. However, ceramic based CaP materials have been investigated extensively in the last 30 years and as a result of these studies, the following statement can be made: CaP materials are important for their bioactive nature; i.e. their capacity to bond to bone without encapsulating connective tissue or provoking an excessive and uncontrollable immunological response. It has been hypothesized that this bone bonding ability to living bone depends on the formation of specific CaP layers of an amorphous nature, which later develops into a crystalline HCA layer. The formation of this HCA layer is not only affected by the composition of the original constituents of the ceramic material, but also by the manufacturing route adopted and by its substrate characteristics.

The biological activity of bone substituting materials has been extensively documented for CaP compounds<sup>20-22</sup>. The process by which the HCA crystalline layer forms on the surface of any biomaterial in the presence of simulated body fluids (SBF) is analogous to

the natural bone mineralization process<sup>23-25</sup>. This step is fundamental in determining the bioactivity of any material.

Generally, the formation of HCA crystals can occur on any CaP compound. However, nucleation on apatitic substrates is immediate, whilst on CaP compounds an induction period exists<sup>26,27</sup>. This is related to the super-saturation of the Ca/P ion ratio in the surrounding environments. In fact, a high ratio leads to precipitation of an HCA layer on any substrate (be it CaP based or not) with very short induction times. In biological fluids, the Ca/P ratio is known to be very close to the solubility product of OCP<sup>28</sup>. Therefore, in the presence of more soluble CaP compounds e.g.  $\alpha$ -TCP, DCPD and amorphous calcium phosphate (ACP), this ratio increases. It has been found that the dissolution of these phases increases this ratio locally, promoting the precipitation of the HCA crystals and the constitution of the “bioactive” layer<sup>29,30</sup>.

The formation of the bioactive layer is succeeded by two other phenomena: the adsorption of cell adhesion proteins e.g. osteopontin and osteocalcin and the adhesion and expression of osteoblast cells for the regeneration of new bone tissue. These are phenomena, which *in-vivo* can occur both simultaneously or one as a consequence of the other. Nevertheless, how efficiently these processes occur is believed to be intimately linked to all the physical, chemical and biological parameters discussed in prior paragraphs.

#### **2.4. The adsorption of proteins onto the HCA bioactive layer.**

The adsorption of specific proteins on CaP substrates is a complex phenomenon. This mechanism generally operates after the formation of the HCA bioactive layer. However, it has also been known to occur on freshly sintered apatitic surfaces. Presumably the mode of interaction of similar proteins on these two surfaces differs because of their differing physico-chemical properties. In fact, sintered materials tend to exhibit less surface irregularities and thus expose a lower surface area when compared to poorly crystalline apatites formed via a precipitation process from Simulated Body Fluids (SBF). However, one must note that adsorbing a greater number of proteins on a substrate might not necessarily be an advantage. In doing so, the hydrolysis process of the biomaterial might be inhibited.

Porosity is another important parameter that can affect protein adsorption onto biomaterial surfaces. In fact, CaPs produced via the sintering route present macropores that are larger in diameter than the proteins that might adhere to them. Other CaP compounds produced via different routes exhibit micropores especially on the neoformed HCA layer. How is this important? In *in-vivo* situations, pore size could discriminate which proteins would adhere to these surfaces and thus influence the overall biological activity of an implant. The occupation of porous materials by cells and/or specific proteins could depend on this porosity parameter, but no specific studies have been published as of yet on this concept.



## **2.5. Cell involvement and participation in the regeneration of new bone tissue.**

After implantation, multi-nucleated cells similar to osteoblasts are observed on the surface of CaP biomaterials. Other studies utilizing osteoclasts have shown again that substrate composition is important for cell activity. The HCA layer is known to be a good support for osteoclast adhesion and expression. The cells that adhere to these substrates create resorption pits in the immediate vicinity of the border of their cell membranes. S-HA surfaces however, tend not to favor this mode of attachment as biodegradation is very slight<sup>31</sup>. As clearly indicated in *in-vivo* cell culture experiments have indicated this clearly.

Osteoblast adhesion and activity on CaP materials has been extensively studied in cell culture experiments. It is an established and well-recommended test to assess biological activity of the material. This activity is, once again related to the physico-chemical parameters of surface energy, surface charge, etc. For example, the nature of the crystal surface exposed is important and studies have clearly shown that cell adhesion and expression is dependent on this factor<sup>32</sup>.

All these parameters are involved simultaneously, especially as the HCA layer gradually matures in the process of biomineralization. As a result, the direct relationship between the chemical characteristics of a surface and its bioactivity is difficult to decipher from cell-culture experiments, because CaP material solubility and crystal nucleation phenomena can change considerably depending on the media to which they

are exposed. In addition, identical materials may act differently in *in-vivo* situations depending on: where the implant is situated in the body; the animal species that hosts it; its health state; and its gender etc.

## **2.6. Analytical techniques adopted for the characterization of CaPs.**

The above paragraphs have discussed the validity of CaPs as biomaterials. Unfortunately, all the studies to date concerning their structure, composition and surface properties have resulted in an incomplete and insufficient characterization. Consequently, the biological and clinical studies performed utilizing these samples have been inaccurate because of contradicting trends. This has prevented researchers precisely linking the physico-chemical information to the biological properties of these materials thus failing to identify those that are relevant for biomedical applications.

Although there must be a correlation between the physico-chemical characteristics of a biomaterial and its biological properties, the influence of specific parameters is very difficult to discriminate from others. In fact, this is why often poorly characterized samples do not shed light on the matter. However, some studies have found links between physico-chemical properties and biological behavior, especially with regards to the phenomena of biodegradation and bioactivity.

It is important to adopt the correct analytical techniques in order to identify the physico-chemical properties of CaPs. It is also fundamental to understand what

characterization method is required. Answering the following questions is often useful: What is the material's structure, composition and texture? What are its physical and chemical properties? How does it behave in *in-vitro* and *in-vivo* situations; e.g. its biological properties? By solely answering the first of the above questions, all others are resolved. Thus, the following analytical techniques were chosen for the analysis of CaP materials produced via SHS: X-ray diffraction (XRD), Fourier Transform Infra-red Spectroscopy (FTIR), Scanning Electron Microscopy (SEM) with the Electron Dispersive X-ray Spectroscopy (EDS) function, inductively coupled plasma (ICP) and X-ray photoelectron spectroscopy (XPS) and atomic force microscopy (AFM).

XRD was performed in order to obtain structural information of these biomaterials i.e. the nature and amount of mineral phase present<sup>33</sup>. Crystalline compounds are easily identified and quantified by using this method. However, complications arise when considering heterogeneous apatitic materials in the presence of amorphous phases, as was the case with the CaPs produced via SHS. Similarly, FTIR was adopted for its ability to determine both chemical and structural information<sup>34</sup>.

SEM on the other hand, was utilized as an image analysis technique. This method was used to directly observe surface texture; i.e. parameters of macro and micro-porosity, surface morphology and topography (both before and after treatment) etc.

XPS was used to determine the surface composition. This technique is sensitive to the first atomic layer of the surface of a material and can identify the surface location of

particular ions that may appear only as trace elements in the other bulk characterization techniques<sup>33</sup>.

AFM was used to determine surface topography. However, as prior studies have shown, atomic resolution is difficult and generally produces pictures that can lead to ambiguous interpretations<sup>35,36</sup>.

## 2.7. Concluding remarks.

Previous studies have demonstrated that the formation of the HCA bioactive layer is not only affected by the composition of the original constituents of the biomaterial, but also by the manufacturing process adopted e.g. sintering or sol-gel processing<sup>37,38</sup>. In this study an experiment was designed in which five different “dopants” (SiO<sub>2</sub>, TiO<sub>2</sub>, Al<sub>2</sub>O<sub>3</sub> and MgO) were introduced into the TCP-based SHS synthesized ceramics. This was done in order to observe if their biological activity, in terms of HCA formation, is in fact related to the addition of each dopant when placed into a SBF solution.

The new method of combustion synthesis has the potential to produce equivalent CaP porous materials very rapidly. This synthesis process is defined as one wherein an exothermic chemical reaction produces a desired product. The process is self-sustaining and generally results in the formation of at least one solid-phase product. The exothermicity of the reaction is what provides the drive and most of the energy required to complete the synthesis of new material. This type of synthesis can be performed in two modes depending on the medium involved in the reaction. When the reactants are in the condensed phase the mode is termed: *self-propagating high temperature synthesis (SHS)*. However, when the medium is primarily gaseous the mode is termed *gas-combustion synthesis*. In this study the Self-propagating high temperature synthesis mode was utilized.

The work presented in this thesis seeks to characterize CaP-based ceramics produced via SHS and to elucidate their biological activity when subjected to the simulated *in-vitro* environment. Some insight on the mechanisms involved in rendering these materials more bioactive is acquired.

## CHAPTER 3

### MATERIALS AND EXPERIMENTAL METHODS

The information gained from the extensive literature review on CaP biomaterials was fundamental in order to formulate and design an experiment that would fulfill our objectives. The general experimental outline of this study was structured in the following manner, in an effort to elucidate the mechanisms involved in the formation of the HCA layer when placed into SBF solution.

- The production of five different CaP systems manufactured via the SHS method.
- Their bulk analysis utilizing XRD, FTIR and other experimental techniques.
- The creation of a simulated body fluid (SBF) solution in order to “simulate” the inorganic part of blood plasma i.e. a physiological *in-vitro* environment.
- The 10-day placement of the SHS samples in the SBF environment and the monitoring of pH during this time period.
- The observation and comparison of surface modifications of these samples via traditional surface analytical techniques e.g. SEM and XPS

### 3.1. Sample Preparation.

Five Ca-P based chemistries were prepared with identical chemical compositions as presented in Table 3.1. The reactant powders had the following characteristics: CaO (325 mesh = 45  $\mu\text{m}$ , 99.99% pure),  $\text{P}_2\text{O}_5$  (100 mesh = 150  $\mu\text{m}$ .), 99.99% pure),  $\text{SiO}_2$  (325 mesh, 99.6% pure),  $\text{TiO}_2$  (325 mesh, 99.99% pure),  $\text{Al}_2\text{O}_3$  (325 mesh, 99.99% pure), and  $\text{MgO}$  (325 mesh, 99.95% pure). [Where 325 mesh = 45  $\mu\text{m}$  and 100 mesh = 150  $\mu\text{m}$ .]

**Table 3.1.** The chemical constituents in each of the five CaP systems (S1-S5) are presented in Table 3.1. 20 g batches were made with a molar ratio of 3:1:1 respectively for CaO:  $\text{P}_2\text{O}_5$ : dopant. The table shows the mol% and wt% of each component in the mixture.

Theoretical Values				
Pellet #	Chemical	M. required (g)	Wt%	Mol%
S1	CaO	10.85	54.24	19.35
	$\text{P}_2\text{O}_5$	9.15	45.76	6.45
S2	CaO	9.09	45.45	16.21
	$\text{P}_2\text{O}_5$	7.67	38.35	5.40
	$\text{SiO}_2$	3.25	16.25	5.40
S3	CaO	8.63	43.15	15.39
	$\text{P}_2\text{O}_5$	7.28	36.40	5.13
	$\text{TiO}_2$	4.09	20.45	5.12
S4	CaO	8.16	40.82	14.55
	$\text{P}_2\text{O}_5$	6.89	34.44	4.85
	$\text{Al}_2\text{O}_3$	4.95	24.74	4.85
S5	CaO	9.60	48.00	17.12
	$\text{P}_2\text{O}_5$	8.09	40.49	5.69
	$\text{MgO}$	2.30	11.50	5.70

Chemical	R.m.m(g)
CaO	56.08
$\text{P}_2\text{O}_5$	141.94
$\text{SiO}_2$	60.09
$\text{TiO}_2$	79.88
$\text{Al}_2\text{O}_3$	101.96
$\text{MgO}$	40.31

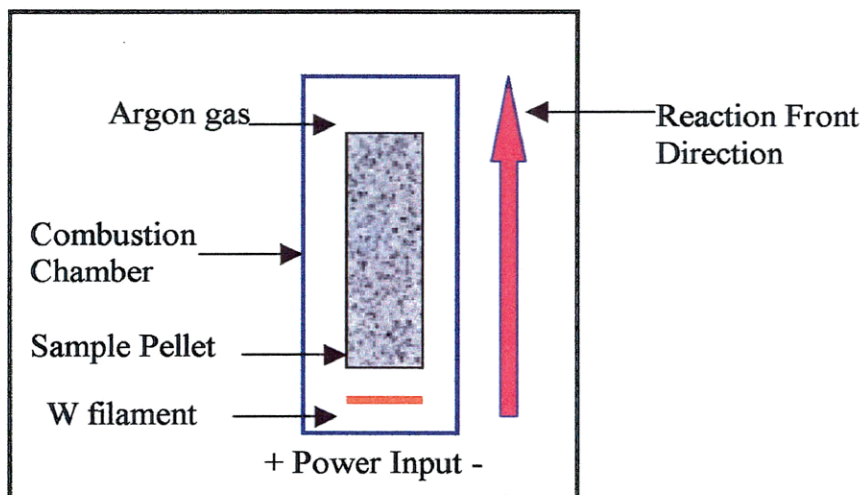
  

Note:

Chemical	Ideal Ratio
CaO	3
$\text{P}_2\text{O}_5$	1
Diluent	1



Each chemistry was prepared in an argon atmosphere due to the strong hygroscopic nature of the phosphorus pentoxide ( $P_2O_5$ ) and was pressed into a cylinder of the following dimensions: diameter =12mm and height =18mm. The sample was reacted via the SHS method in argon gas and allowed to cool in air (Figure 3.1). The resultant cylindrical reaction product was ground into powder form using a pestle and mortar and manually sieved to a particle size of  $<53\mu\text{m}$  (Figure 3.2 on page 21). The powder was then stored in an oven at a constant temperature of  $50^\circ\text{C}$  so as to stabilize its condition prior to any treatments or analyses.



**Figure 3.1.** A schematic diagram of the Self-Propagating High-temperature Synthesis (SHS) reaction method.

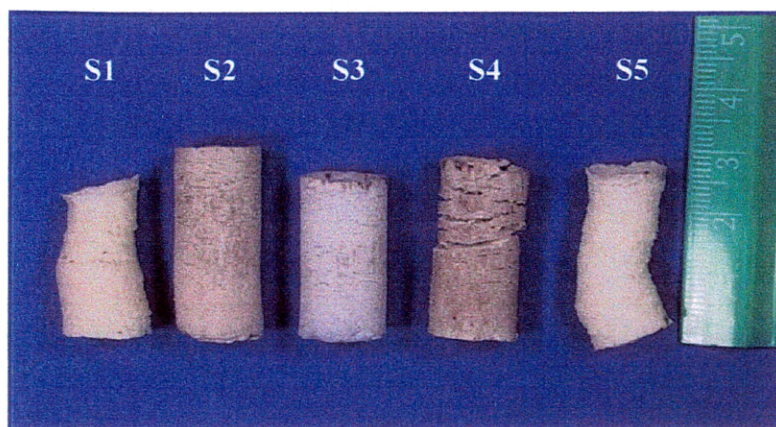


**Figure 3.2.** A schematic diagram of the Self-Propagating High-temperature Synthesis (SHS) CaP-based products.

In order to evaluate the effect of the material's composition when placed in the "physiological" environment, 5 mg from each system was soaked individually into 10 ml volume of SBF at 37°C, under static conditions, for a total of 10 days. The reason for adopting these parameters was to standardize the experimental set-up and best simulate the inorganic environment of human blood plasma.

The SBF solution was made by dissolving reagent-grade compounds (NaCl, K<sub>2</sub>HPO<sub>4</sub>, MgCl<sub>2</sub>, CaCl<sub>2</sub> and Na<sub>2</sub>SO<sub>4</sub>) into de-ionized water and buffering the solution to a pH of 7.25 (using tris-hydroxy-methyl-ammino-methane (THAM) and hydrochloric acid (HCl)) (Table 3.2 on page 22). This pH value represents the most ideal condition for HCA precipitation to occur in an aqueous media. However, it also falls within the physiological pH range of human blood (pH 7.4).<sup>23</sup>

**Table 3.2.** Illustrates the chemical constituents of the simulated body fluid (SBF) solution.

<b>Theoretical SBF (1liter)</b>					
<b>Chemical</b>	<b>r.m.m.(g)</b>	<b>Conc.<sup>a</sup> (M)</b>	<b>Volume (l)</b>	<b>Moles</b>	<b>Mass (g)</b>
<b>NaCl</b>	57.440	<b>0.1378</b>	1.0	0.1378	7.9152
<b>NaHCO<sub>3</sub></b>	36.009	<b>0.0042</b>	1.0	0.0042	0.1512
<b>KCl</b>	73.550	<b>0.0030</b>	1.0	0.0030	0.2207
<b>CaCl<sub>2</sub></b>	108.980	<b>0.0025</b>	1.0	0.0025	0.2725
<b>K<sub>2</sub>HPO<sub>4</sub></b>	174.178	<b>0.0020</b>	1.0	0.0020	0.3484
<b>MgCl<sub>2</sub></b>	93.210	<b>0.0015</b>	1.0	0.0015	0.1398
<b>THAM</b>	121.030	<b>0.0500</b>	1.0	0.0500	6.0515
<b>HCl</b>	0.000	<b>0.0450</b>	1.0	0.0000	0.0000

**Note:**  
 1. Solution was made up to 1 liter  
 2. Solution was buffered to pH = 7.25  
 3. Mixed for 24 hr with a magnetic stirrer at 300 rpm

During the 10-day period, the pH of each system was recorded using a hand-held Corning pH meter every six hours for the first day and from then on, once daily. On completion of the study, the powders were subsequently filtered using medium grade filter paper and dried in an oven at 50°C for 24 hours. They were then retrieved and prepared for examination using surface, bulk and chemical analytical techniques.(See Figure 3.3 on page 23)

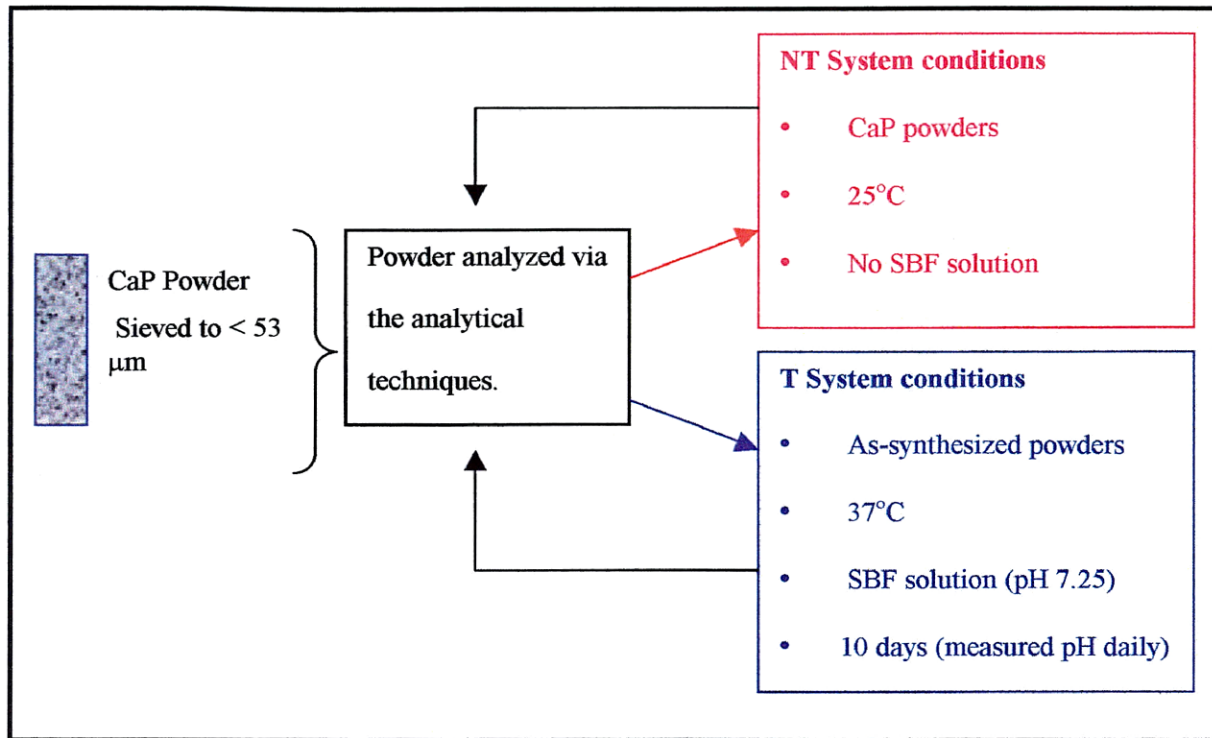


**Figure 3.3.** Schematic illustrating the general experimental set-up.

### 3.2. Characterization of the Powders.

All powders, treated (T) and non-treated (NT) in SBF were studied using the following techniques: XRD, FTIR, SEM, XPS, and ICP. The first two techniques are known as bulk techniques. The second two, give surface information, whilst the last one is a very accurate elemental quantification method.

#### 3.2.1. X-ray Diffraction Analysis.

With regards to XRD, the patterns were obtained by a Siemens Kristalloflex-810 unit using Cu K $\alpha$  in  $2\theta$ - $\theta$  scans ranging from  $5^\circ$  to  $55^\circ$   $2\theta$ . The powders were mounted onto a slide using the double sticky-tape method. The 10 most intense peaks from all resultant spectra were identified. The peak matchings were performed by taking the respective  $2\theta$  values for these peaks and comparing them against the 10 most intense peaks in the standard JCPDS cards for the following materials:  $\alpha$ -TCP,  $\beta$ -TCP, HA, HCA. A tolerance of (+/-) 0.2  $2\theta$  was allowed. (See Appendix 2).

### 3.2.2. Fourier Transform Infrared Spectroscopy (FTIR) Analysis.

FTIR spectra were obtained in a Nicolet IR spectrometer by analyzing potassium bromide (KBr) windows. These were made by mixing 1 mg of powder with 200 mg of KBr and compacting it altogether in a die at 800 MPa for 1 minute. An analysis of each spectrum was performed by matching standard FTIR wave number values for the following materials:  $\alpha$ -TCP,  $\beta$ -TCP, HA, HCA with those obtained. In order to identify what material actually deposits on the surface of the CaP powders due to treatment, a subtraction of the untreated spectra from the treated spectra for each system was performed. The resultant subtraction spectrum was analyzed by comparing wave numbers and matching them against those in standard spectra. (See Appendix 3) Note: prior to the peak identifications each spectrum was put into absorbance mode, smoothed, normalized and auto-baselined. The peak identification were performed with a sensitivity measurement of 75%.

### 3.2.3. Scanning Electron Microscopy Analysis.

Surface information was obtained via SEM and XPS studies. SEM analysis was conducted using a SEM 2000 RJ Instrument. The sample preparation consisted in carbon coating the powders. This coating was chosen to avoid peak overlap of one gold peak with the K line of phosphorus. The energy dispersive spectroscopy (EDS) module of the

SEM machine was used to perform gross quantification of elements that might have been present on the surface. Energy dispersive spectroscopy (EDS) is a typical module available with the SEM. Concentrating the electron beam on a specific area and capturing the scattered signals provides an output spectrum which is the summation of typical peaks of various elements present in the sample. In this study, the quantification of the following elements was performed: Ca, P, O, C, Si, Ti, Al, Mg. From these values, calcium to phosphorus (Ca/P) ratios were calculated. These were compared to those determined from the XPS elemental quantification data, as this method possesses a higher degree of sensitivity. (See Appendix 6)

#### 3.2.4. X-ray Photoelectron Spectroscopy Analysis.

The XPS analysis was performed in a VG ESCALAB MkII unit, with a base pressure of  $8 \times 10^{-10}$  torr in the analysis chamber. The pressure during analysis was  $1 \times 10^{-9}$  torr. 250-Watt Al  $K\alpha$  radiation was used to excite photoelectrons. Survey scans were performed with the three-channel analyzer operating at a constant pass energy of 100 eV. Higher resolution scans over the carbon and oxygen 1s peaks were carried out using a pass energy of 20 eV. A 3 mm (A1) aperture was used. Taking the area under the principal peak of each element in the spectrum and dividing it by an empirically derived sensitivity factor obtained from quantitative data. This value is proportional to the

concentration of that element on the surface. The sensitivity of this technique is about 0.1 atomic percent, (at %) depending on the element under analysis. (See Appendix 4)

### 3.2.5. The Inductively Coupled Plasma Analysis.

The Inductively coupled plasma (ICP) test was used to confirm the presence and the percentage of all elements in SBF samples. The procedure adopted is a variation of the U.S. EPA200.7. The plasma is generated in a magnetic field created inside of the coils of a radio frequency (RF) generator; the heating of the plasma gas is made conductive by a Tesla spark discharge accomplished with the oscillatory current formed inside the RF coil. The liquid sample is delivered to the plasma at a rate of 1 mL/min and sucked into the plasma where three 10-second integration time replications are measured.

This ICP method was performed on all the SBF solutions that had undergone the 10-day treatment, and the original SBF solution was used as the control system. This technique was used because of its very accurate quantitative nature. It could help investigate the presence of dissolution or precipitation phenomena. An indication of the dissolution phenomenon is demonstrated by an increase in the amount of CaP constituents in the SBF solution after the 10-day treatment. Conversely, the precipitation process would be manifested by a severe loss of Ca and P ions from the SBF solution. The sample preparation for this analytical technique is complex and also destructive. However, it is very useful when there is a need to quantify elements accurately.



The sample analysis consists of a two-stage process. The first stage involved the sample digestion, whilst the second, its elemental analysis. In the digestion stage, the 10 solid powder samples were received for elemental analysis (i.e. five untreated and five treated – one from each system). These were each dissolved separately by mixing the material with strong acids followed by gravity settling of any insoluble material before its dilution and quantification by ICP. The amount of material used for each sample analysis was 0.1g. The samples were then subsequently weighed into 50 mL centrifuge tubes followed by approximately 10 g of concentrated trace-metal grade hydrochloric acid (12 M). About 10 g of concentrated trace-metal grade nitric acid (16 M) was added followed by enough 5% nitric/hydrochloric solution to bring the total weight to 25 mL. The solutions were then allowed to digest for 1 hour. Insoluble material was allowed to gravity settle before the digestions were diluted 10x in 1% nitric acid in preparation for analysis.

Two independent calibration check standards were also analyzed. All elements except phosphorus were within acceptable limits (10%). The scandium internal standard added to correct for instrument drift was also within acceptable limits for all samples (10%). The values reported indicate the concentration of the measured elements in mg of element per g of solid digested. (See Appendix 5)

## CHAPTER 4

### RESULTS

#### 4.1. Scanning Electron Microscopy results.

SEM photomicrographs were taken of the five as-synthesized CaP powder systems at both 5000x and 10,000x magnification. These were compared to SEM photomicrographs of the same powder chemistries, but subjected to the 10-day simulated body fluid treatment. The photomicrographs of the as-synthesized systems showed System 1 (the Control System) differing considerably in microstructure from the other surfaces. This observation was valid for all systems (See Figure 4.1. page 30).

##### 4.1.1 The NT samples.

For the as-synthesized (NT) samples, the control surface (S1) was structurally more homogenous when compared to the other four CaP systems. Systems two to five (S2-S5), presented varying and uneven surface characteristics of morphology, topography and rugosity. This heterogeneity was manifested also in terms of the different phases present in these powders (i.e. both crystalline and amorphous). In addition, macro and micro-

pores with varying size distribution were observed. They seem to interconnect with one another resulting in an anastomosis of these features. However, this characteristic is difficult to confirm, as fracturing these powders for examination was problematic.

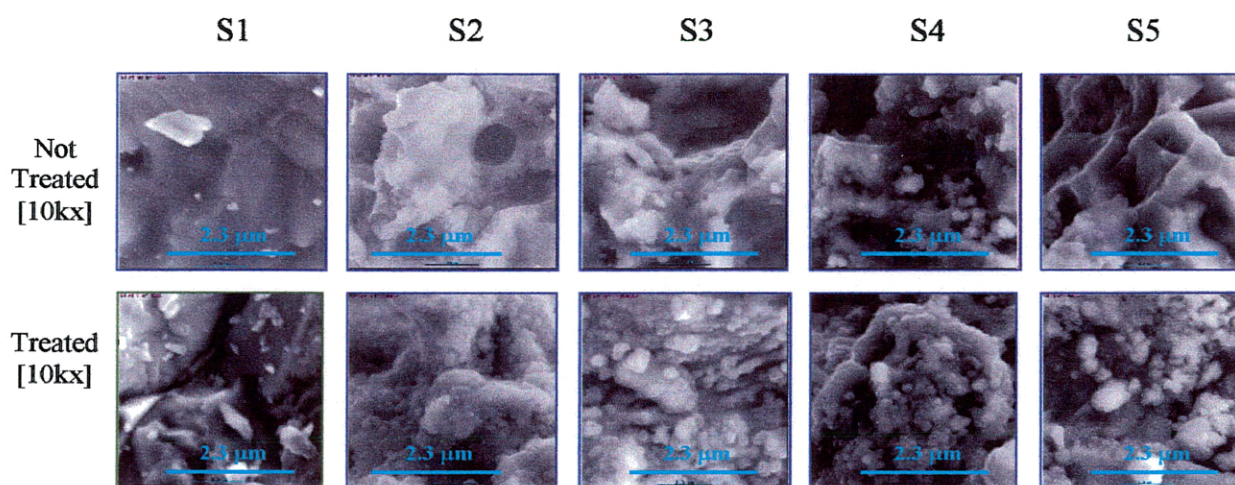


**Figure 4.1.** 10 SEM photomicrographs. The top five represent the non-treated (NT) as synthesized systems S1 to S5. The bottom five represent the respective treated (T) systems. All photomicrographs were taken at 10,000x.

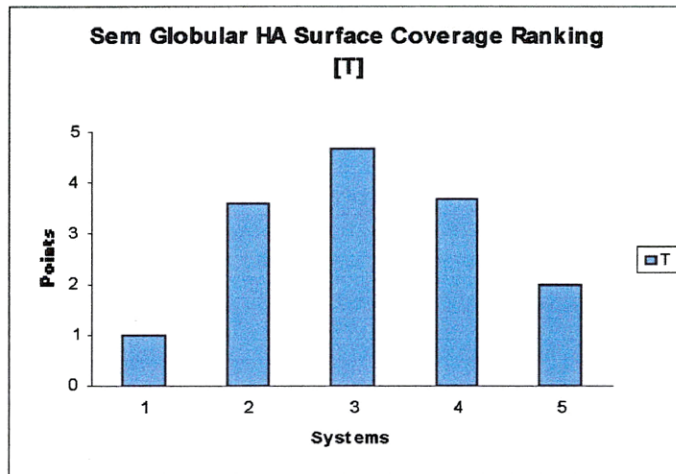
#### 4.1.2. The T samples.

The SEM photomicrographs of the five CaP systems that were subjected to the 10-day SBF solution confirmed that the treatment had dramatic effects on their surfaces. Similarly, as seen for the untreated systems, the control chemistry (S1) showed an atypical behavior since it did not present the same surface characteristics as those of the other CaP powders (S2 to S5). The S1 surface possessed solely crystalline structures of varying size dispersed on it. EDS analysis was later performed and it was found that these crystals pertained to alkali salts that formed as a result of the precipitation of the constituting ions of these salts from the SBF solution. (XPS and ICP analytical techniques later confirmed this result).

Conversely, the S2 to S5 T powders presented surface features in the form of globular agglomerations. The degree to which the powder substrates were covered by these formations varied depending on the CaP chemistry. An empirical ranking was undertaken to quantify the amount of this surface coverage. In the order of most-to-least coverage, the systems were ranked in the following manner: S3 (TiO<sub>2</sub> doped) > S4 (Al<sub>2</sub>O<sub>3</sub> doped) > S2 (SiO<sub>2</sub> doped) > S5 (MgO doped) > S1(Control). (See Figure 4.2 on page 32)

These globular structures were similar in morphology to the expected carbonate hydroxyapatite (HCA) bioactive layer that has been known to form on other CaP-treated

powders fabricated via sintering or sol-gel synthesis routes. This was an indication that the bioactive layer was forming on the CaP powders produced via the SHS method<sup>25</sup>.



T												Av. Rank
S1 T	1	1	1	1	1	1	1	1	1	1	1	1
S2 T	5	3	5	3	3	3	3	5	3	3		3.6
S3 T	4	5	4	5	5	5	5	4	5	5		4.7
S4 T	3	4	3	4	4	4	4	3	4	4		3.7
S5 T	2	2	2	2	2	2	2	2	2	2		2

**Figure 4.2.** The empirical ranking system utilized to determine the globular agglomeration surface coverage of the CaP treated systems.

Heterogeneity is again the key word in describing the nature of these surfaces. Porosity also seems to be a contributing factor to their structural diversity. However, this feature becomes less evident with the increasing coverage of the HCA layer.

Many questions immediately arose when observing these globular formations. Are these features a result of a dissolution or precipitation process? If they are the remnants of a dissolution process, are they the result of the desegregation of the more soluble amorphous phases present in the CaP powders? Conversely, could these surfaces be representative of an amorphous calcium phosphate (ACP) layer that forms via the precipitation of  $\text{Ca}^{2+}$  and  $\text{PO}_4^{3-}$  ions from the SBF solution? It was later found that both processes actually occur, with precipitation being dominant with respect to the dissolution process.

## 4.2. X-ray Diffraction results.

The XRD data analysis was performed by attempting to match the 10 most intense peaks from the NT and T samples, to the 10 most intense standard  $2\theta$  values for the following materials:  $\alpha$ -TCP,  $\beta$ -TCP, HA, and HCA. Out of the 10 peaks not many matches could be identified with the standard data because of the very stringent tolerance values adopted [(+/-) 0.2 of  $2\theta$ ]. However, as a general statement, all the samples, regardless of whether they were untreated or treated showed the presence of numerous phases. Thus, the SHS method produced CaP powders of varying phase constitution.

More specifically: S1 and S5 showed a high number of  $2\theta$  peak matches for  $\alpha$ -TCP. (See Table 4.1 page 35 and Figures 4.3. to 4.6. on pages 36 and 37). Both the NT and T samples indicated a strong presence of the  $\alpha$ -TCP phase, particularly S1. Apatitic peaks were also identified, although not in prevalent quantity. This suggested that these chemistries possess a lower SHS combustion temperature ( $T_c$ ), resulting in the production of the higher temperature phase of tricalcium phosphate ( $\alpha$ -TCP).

Systems S2 to S4 demonstrated a higher degree of heterogeneity when compared to the two prior systems. (See Table 4.2 page 38 and Appendix 2 for their specific XRD Spectra). Not only were  $\alpha$ -TCP and apatitic peaks from both HA and HCA identified, but these systems also presented a higher incidence of the  $\beta$ -TCP phase. The diluents present in these CaP systems (respectively  $\text{SiO}_2$ ,  $\text{TiO}_2$  and  $\text{Al}_2\text{O}_3$ ) notably had the effect of

increasing each chemistry's overall  $T_c$ , thus explaining the formation of the lower temperature tricalcium phosphate  $\beta$  phase.

**Table 4.1.** XRD peak matches for systems S1 and S5 (T) and (NT) samples.  $\alpha$ -TCP matches were predominantly found with some apatitic peaks being present.

Peak	Phase	S1 NT	S1 T	Peak	Phase	S5 NT	S5 T
[043]	$\alpha$	1175	-	[080]	$\alpha$	1562	1852
[080]	$\alpha$	-	1395	[510]	$\alpha$	2936	3555
[111]	$\alpha$	570	335				
[132]	$\alpha$	843	475				
[150]	$\alpha$	555	710				
[170]	$\alpha$	2937	2444				
[202]	$\alpha$	1812	-				
[510]	$\alpha$	-	456				
				[222]	HCA	-	932
[111]	HA	-	1145				
[002]	HA	324	210	[002]	HA	1071	1287
[211]	HA	2937	-	[211]	HA	-	-
[112]	HA	361	284	[112]	HA	-	-
[300]	HA	-	-	[300]	HA	348	559
[004]	HA	-	-	[004]	HA	657	1106



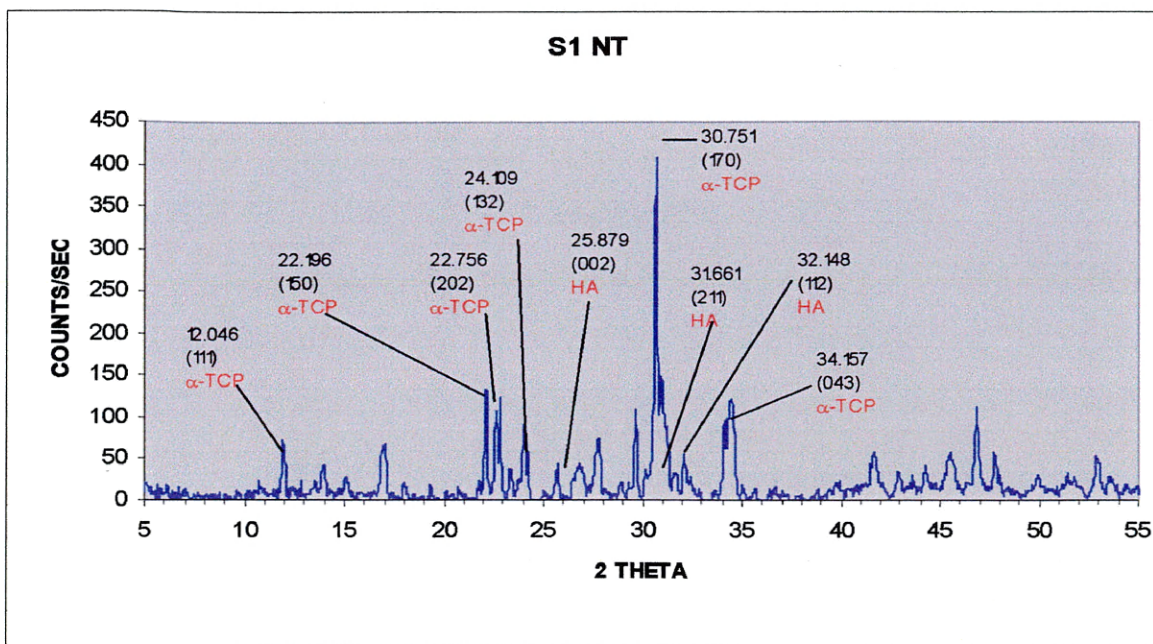


**Figure 4.3.** This XRD figure depicts peak matches for systems S1 untreated (NT) sample.

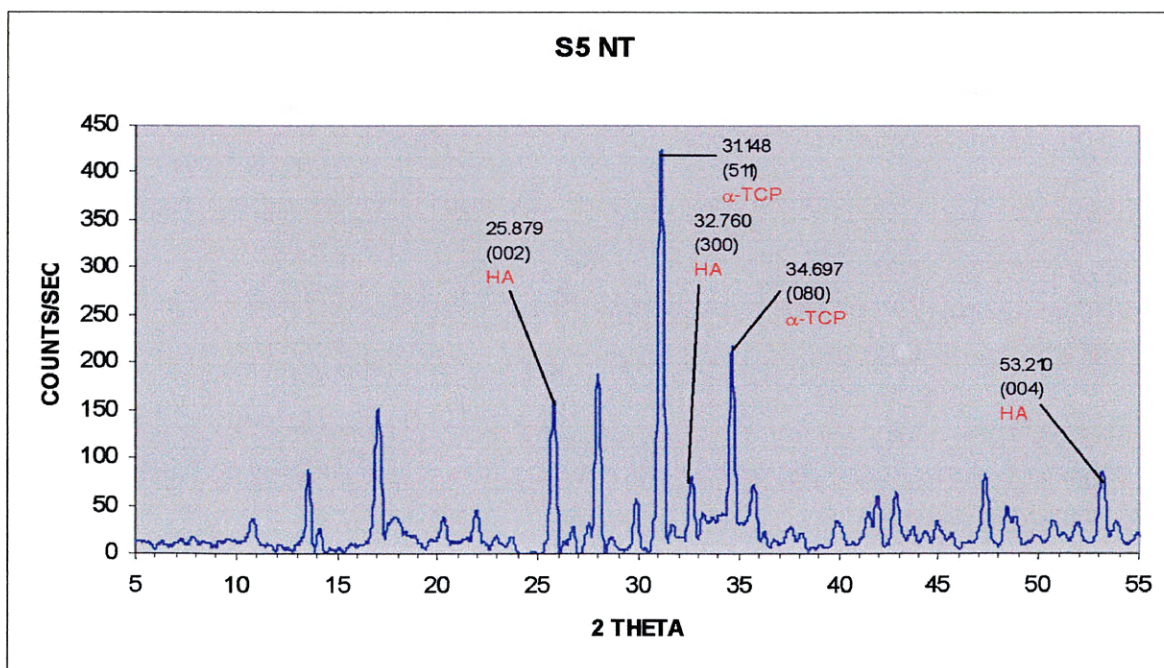


**Figure 4.4.** This XRD figure depicts peak matches for systems S5 untreated (NT) sample

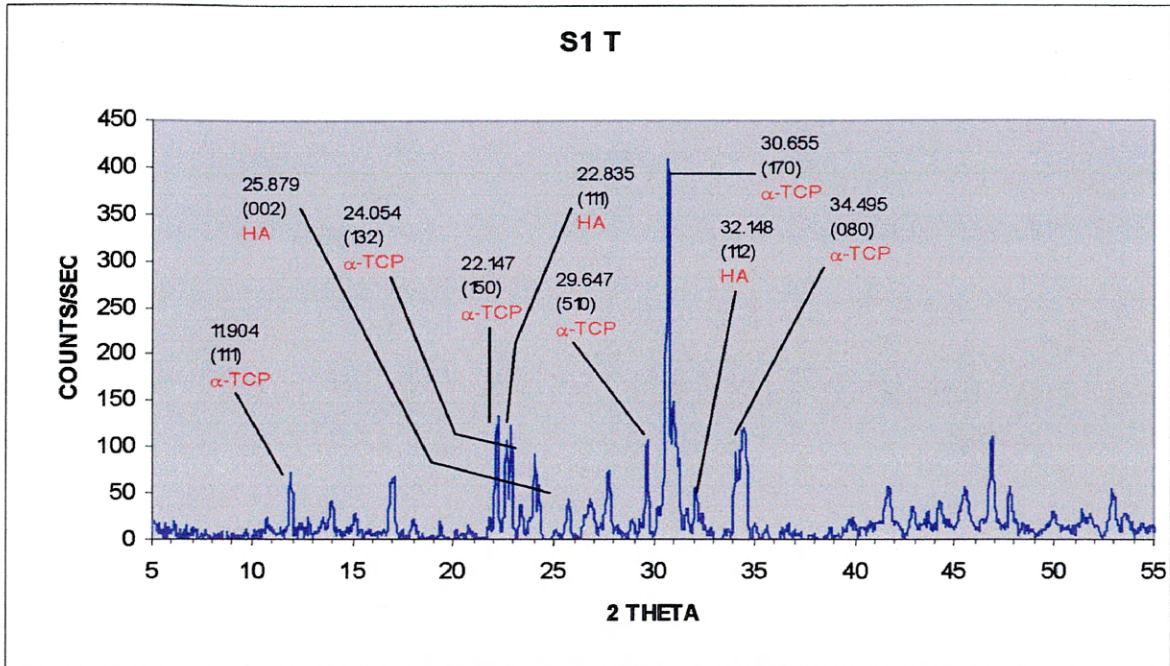


**Figure 4.5.** This XRD figure depicts peak matches for systems S1 treated (T) sample

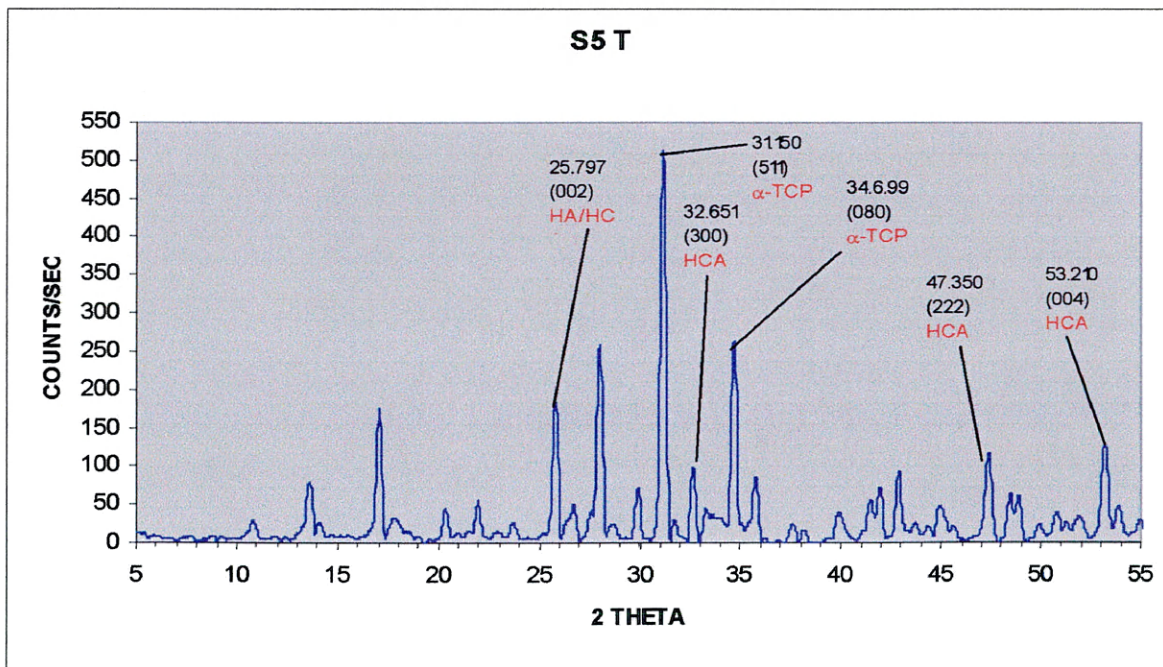


**Figure 4.6.** This XRD figure depicts peak matches for systems S5 treated (T) sample.



**Table 4.2.** XRD peak matches for systems S2 to S4 (T) and (NT) samples. The tables attribute specific hkl peak values to certain phases that were identified. The material results in being very heterogeneous.

Peak	Phase	S2 NT	S2 T	Peak	Phase	S3 NT	S3 T	Peak	Phase	S4 NT	S4 T
[043]	$\alpha$	1860	533	[080]	$\alpha$	641	661	[043]	$\alpha$	2105	-
[170]	$\alpha$	881	569	[170]	$\alpha$	728	555				
[510]	$\alpha$	-	791	[151]	$\alpha$	-	550				
[212]	$\beta$	677	-	[202]	$\beta$	1063	922	[002]	$\beta$	1037	1113
[400]	$\beta$	518	398	[220]	$\beta$	907	1320	[212]	$\beta$	-	568
[510]	$\beta$	491	-	[510]	$\beta$	275	339	[412]	$\beta$	961	1385
								[510]	$\beta$	614	729
				[210]	HCA	-	991	[202]	HCA	-	2148
								[210]	HCA	524	-
				[202]	HA	-	621				
[002]	HA	-	210	[210]	HA	569	-	[002]	HA	1037	1113
[211]	HA	612	-	[002]	HA	-	405	[211]	HA	899	1116
[112]	HA	-	284	[211]	HA	-	1123	[112]	HA	-	-
[300]	HA	-	-	[112]	HA	-	-	[300]	HA	350	214
[004]	HA	-	-	[300]	HA	-	-	[004]	HA	-	-
				[004]	HA	0	107				

The amount of the  $\beta$ -TCP phase in the above chemistries (S2 to S4) was correlated to the globular features present on the surface of these powders after treatment. Conversely, S1 and S5 that showed absence of the  $\beta$ -TCP phase were the two cases in which the lowest degree of formation of these features was evident.

Five specific hkl peaks were chosen to identify crystalline apatitic structures forming as a result of the SBF treatment. Their peak area values were noted before and after the SBF treatment and compared. The following apatitic peaks were utilized: (002), (211), (112), (300), and (004). They occur at these respective  $2\theta$  values:  $25.879^\circ$ ,  $31.661^\circ$ ,  $32.148^\circ$ ,  $32.76^\circ$ , and  $53.210^\circ$ . This latter peak is often used when looking at HA, as there are no overlapping diffraction peaks from other CaP phases.

The results showed that all the samples, regardless of whether they were treated or not, presented some of the five standard apatitic peaks. For the NT samples, a general increase in their peak areas with treatment was observed. The exception to the rule was the control system (S1). The same applied for the T systems. The numbers of identified apatitic peaks increased, but again, this was not so for S1. Therefore, as a general rule, all CaP systems except for the control exhibited an increase in the area of the standard apatitic peaks identified prior to treatment, and an increase in the number of new apatitic peaks with treatment. (Refer to Tables 4.1. and 4.2. on pages 33 and 36 respectively)

The (004) peak (the critical peak for the specific identification of crystalline HA) was identified only for the S3 ( $\text{TiO}_2$ ) and S5 ( $\text{MgO}$ ) treated chemistries. It was not detected for the other systems. (See Tables 4.1 and 4.2 – pink highlighted areas on pages 33 and 36) However, new apatitic peaks, not pertinent to the standard five HA peaks were also identified. These were specific to the carbonate form of HA and were seen in the S3 to S5 T chemistries.

Finally, all the apatitic peaks identified were broad and low in intensity with respect to the standard crystalline peaks seen in the literature. This indicated their low degree of crystallinity or conversely, their high amorphous nature. This suggesting that an ACP structure had most likely deposited onto the surface of the treated chemistries. This certainly, was a possibility as it agreed with previous studies on the maturation process HA undergoes in an aqueous environment. These have demonstrated an ACP phase developing into a more crystalline HA phase<sup>31</sup>.

In this study, it is proposed that the bioactive layer does not have sufficient time to “mature” to a crystalline HA structure. This is why crystalline HA peaks are not detected by XRD.

### 4.3. Fourier Transform Infra-red Spectroscopy results.

FTIR spectroscopy gives information on the chemical composition and on the degree of crystallinity of the precipitates. Table 4.3 on page 42 and Figures 4.7 and 4.8 on pages 43 and 44, present the absorption data for S2 NT and T samples, as representative of the main general changes observed during this work. (FTIR data for the other systems are listed in Appendix 3) It appears from the general results that CaP powders produced via SHS are very heterogeneous confirming prior XRD results. The absorption bands observed for the NT samples indicate the presence of  $\alpha$  and  $\beta$ -TCP and of apatitic peaks from HA and HCA. CaO bands also appear in every system indicating that the reaction has not gone to completion. In addition, no  $\text{OH}^-$  or  $\text{H}_2\text{O}$ , bonds in the  $3400\text{-}3500\text{ cm}^{-1}$  range or  $\text{CO}_3^{2-}$  absorption peaks are present at the  $876$  and  $1400\text{ cm}^{-1}$  band positions. This indicates that the apatitic phases that form in the NT samples are probably not of the HA or HCA form.

**Table 4.3.** Wave number matches identified for S2. The NT,T and subtracted spectra values are also included. The areas highlighted in gray are the most significant and are representative of an A/B-type HCA structure.

Bond Description	Phase Identified	S2 NT	S2 T	Subtracted S2
	$\alpha$ -TCP/CaO	3642.64	3643.04	3805.50
OH Stretch/O-H-O stretch	HA		3429.47	3687.50
	Hydrocarbon			3391.07
CO <sub>2</sub>	HCA			2361.61
CO <sub>3</sub>	HCA			1651.02
CO <sub>3</sub>	HCA		1426.9	1462.75
PO <sub>4</sub> <sup>3-</sup> $\gamma$ 3 P-O anti-sym stretch	$\alpha$ -TCP	1160.91	1214.05	
PO <sub>4</sub> <sup>3-</sup> $\gamma$ 3 P-O anti-sym stretch	HA	1063.90	1042.45	1040.73
PO <sub>4</sub> <sup>3-</sup> $\gamma$ 1 P-O sym stretch	$\beta$ -TCP	970.92	971.07	
PO <sub>4</sub> <sup>3-</sup> $\gamma$ 1 P-O sym stretch	$\beta$ -TCP	939.55		
CO <sub>3</sub>	HCA			871.65
	[?]	795.83	796.01	775.91
	[?]	726.55	726.27	742.61
PO <sub>4</sub> <sup>3-</sup> $\gamma$ 4 P-O anti-sym bend	$\beta$ -TCP		605.4	606.27
PO <sub>4</sub> <sup>3-</sup> $\gamma$ 4 P-O anti-sym bend	$\beta$ -TCP			576.83
PO <sub>4</sub> <sup>3-</sup> $\gamma$ 4 P-O anti-sym bend	HA	564.24	564.94	
O-P-O Deformation		494.48	495.91	

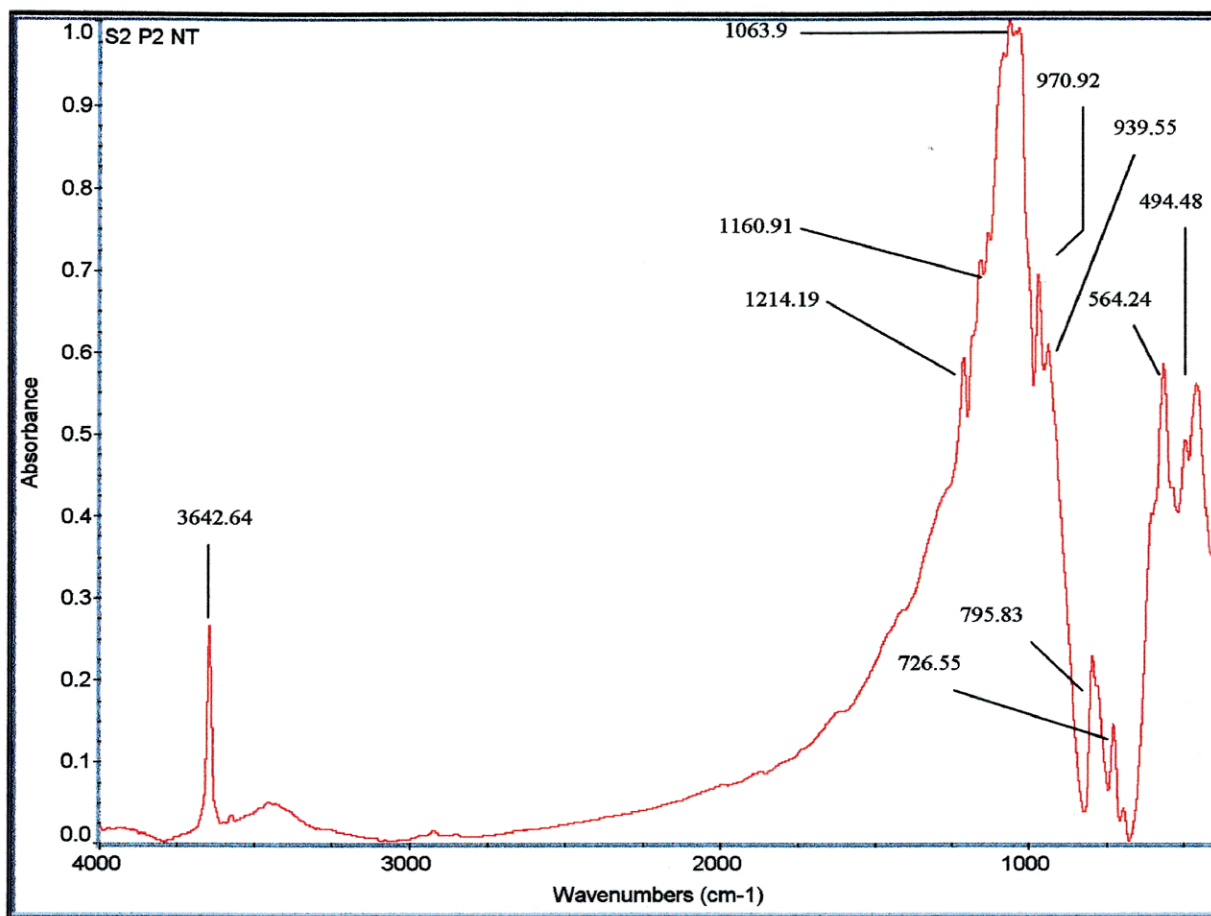


**Figure 4.7.** FTIR spectrum peak matches for systems S2 untreated (NT) sample.



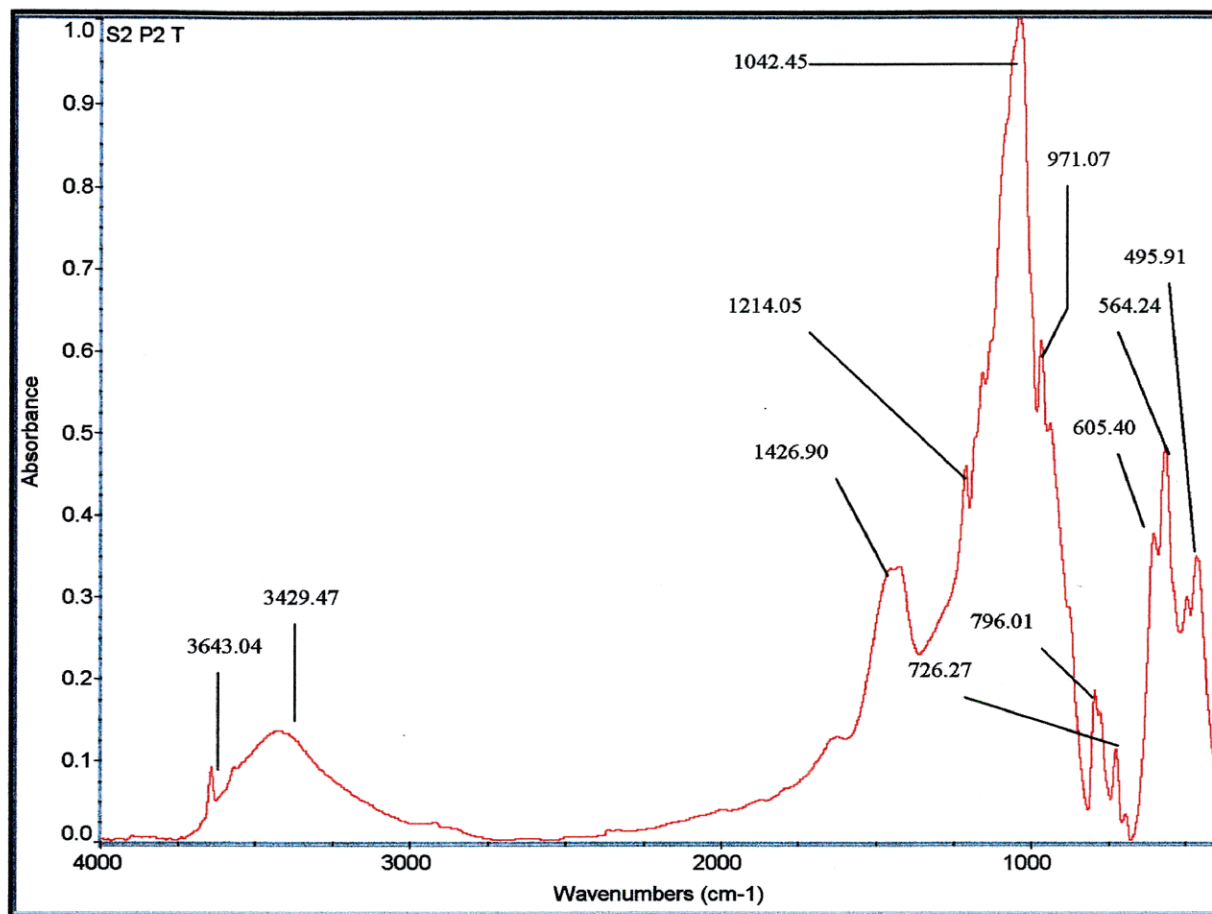


**Figure 4.8.** FTIR spectrum peak matches for systems S2 treated (T) sample.

The absorption bands for the treated spectra are typical of non-stoichiometric HA (NS-HA). These showed that the SBF Treatment does indeed have an effect. In fact, in all the treated systems (and the subtracted spectra also demonstrates this), one can note the presence of  $\text{OH}^-$ ,  $\text{H}_2\text{O}$ , and  $\text{CO}_3^{2-}$  bonds. This is strong evidence that HCA has deposited in the SBF-treated samples. In addition, the HCA is probably of A/B-type as indicated by the presence of  $\text{CO}_3^{2-}$  and  $\text{OH}^-$  bonds coupled to the increasing presence of HA peaks with SBF treatment. It should be noted that when  $\text{CO}_3^{2-}$  groups are incorporated into  $\text{PO}_4^{3-}$  lattice sites in apatitic structures, the apatite formed is then termed a B-type-HCA. When  $\text{CO}_3^{2-}$  groups substitute for  $\text{OH}^-$  species, the apatitic structure is termed an A-type HCA. When both of these events occur either independently or simultaneously, the apatite is termed an A/B-type HCA. The latter case is what seems to be present in all the T CaP powders. This apatite is probably of amorphous nature simply because the HA crystals are not detected by XRD technique. (Except for S3 and S5).

The nature of these precipitates can be deduced from the specific anti-symmetrical stretch ( $\gamma_4$ ) bands of the phosphate ( $\text{PO}_4^{3-}$ ) group. The absorption bands in the ranges of  $560\text{ cm}^{-1}$  and  $601\text{ cm}^{-1}$  coincide with the values for the HA from previous studies and thus confirms the apatitic nature of the phases formed. The typical split bands in this region come from the degeneration of the  $\gamma_4$  vibration with the increasing order in the crystal lattice. This split region is not seen for the Control S1 system. This would make sense as the treatment had no effect on this CaP powder and thus no HA is expected to have deposited onto its surface. Prior SEM and XRD data confirmed this.

$\gamma_1$  and  $\gamma_3$  vibrations in the range of 1130-1030  $\text{cm}^{-1}$  can bring complementary information about the chemical nature of the phase. The broadness of this band was found to decrease with increasing purity of the HA phase in the range 1097-1032  $\text{cm}^{-1}$ . In this study, all the treated systems had fairly broad bands within this range and confirming the heterogeneity of the CaP phases present and the degree of amorphous phase of our final product. It should be noted that the degree of crystallinity can also be affected by the shear size of the HA crystals and the stage of their development they are in. In the treated cases, the presence of crystals was only seen for systems S3 and S5 (indicated by the detection of the (004)-hkl peak from XRD analysis). The appearance of these HA crystals for these systems could mean that the HA material “matures” at different rates on differing surface chemistries

All the above factors render the detailed interpretation of the results and characterization of very similar CaP powders very difficult. For example: many absorption bands in these spectra are very close and overlap with each other, so deconvolution programs would be ideal for a quantitative analysis of the sample composition.

When analyzing the absorption bands from the subtracted spectra data, similar trends were obtained. (See Appendix 3) HA and HCA compounds were found to be precipitated on the treated surfaces and these were identified by the presence of the resultant bands in the ranges of 1043 and 602  $\text{cm}^{-1}$ . The presence of carbonate ions was also noted at 876 and 1400  $\text{cm}^{-1}$  and provides additional evidence that a HA-like bioactive layer was

present on the surface of the S2-S4 CaP powders after the SBF treatment. Systems S1 and S5, (that possessed primarily the  $\alpha$ -TCP phase), demonstrated the tendency not to induce HA/HCA formation. XRD confirmed these chemistries as being more homogenous by possessing a high number of one kind of peak i.e. the  $\alpha$ -TCP peaks. This may explain their morphological and topographical differences when compared to systems S2-S4. The questions then arose to whether surface morphology plays an important role in the formation of the bioactive layer? Does the presence of  $\alpha$ -TCP on these surfaces require longer time frames to develop the HCA layer or will this phenomenon not occur on these surfaces?

#### 4.4. X-Ray Photoelectron Spectroscopy results.

XPS is a surface analytical technique that investigates the first atomic layer of a material. It conducts a very accurate and sensitive elemental investigation of the surface on a nano-scale. The primary purpose of utilizing this method was to determine which phases are present on the CaP surfaces both prior and post treatment. Identifying the surface modifications that result from the SBF treatment and whether they occur because of a dissolution or precipitation process is important since this could help elucidate the mechanisms for the formation of the HCA bioactive layer.

The 10 CaP powder samples were submitted for analysis using the above technique. Five of these were untreated and the other five were treated with the SBF solution. The wide scan spectra showed the presence of expected species and allowed the composition of the powder surfaces to be estimated. Detailed scans over the carbon (C1s) peak showed a complex set of features. The main peak, representing a C-C, C-O and C-H bonding showed clear evidence of broadening after the treatment with the formation of a lower kinetic energy peak. This broadening is most probably related to C-O bond and thus the formation of a carbonate. The nature of the samples (powders with a low probability of carbide formation), would indicate that the peak broadening is due to increased oxidation after treatment. The wide scan spectra and detailed scans of the C1s peak are attached separately in the Appendix. The atomic compositions of the powders have been calculated from the wide scan data and are given in Table 4.4. page 49

**Table 4.4.** Atomic compositions of the CaP powders of both NT and T systems calculated from the wide scan data from XPS analysis.

Surface Composition (At%)												
Sample	O1s	C1s	Ca2p	F2p	F1s	Si2p	Ti2p	Al2p	MgKLL	Na1s	Cl2p	N1s
S1	51.19	22.43	14.04	11.70	0.64	0.00	0.00	0.00	0.00	0.00	0.00	0.00
S1T	36.83	41.96	7.76	5.41	0.00	0.00	0.00	0.00	0.44	1.38	3.26	2.95
S2	51.48	22.24	11.84	11.45	0.00	2.99	0.00	0.00	0.00	0.00	0.00	0.00
S2T	49.55	24.86	13.86	5.32	0.00	2.53	0.00	0.00	1.54	0.75	1.13	0.45
S3	51.67	23.45	12.57	9.85	0.00	0.00	2.45	0.00	0.00	0.00	0.00	0.00
S3T	43.49	34.34	11.46	4.72	0.00	0.85	1.18	0.00	0.87	0.72	0.62	1.75
S4	52.09	24.34	11.06	10.55	0.00	0.00	0.00	1.97	0.00	0.00	0.00	0.00
S4T	46.59	29.66	13.29	5.26	0.00	0.00	0.00	1.18	1.16	0.75	1.47	0.65
S5	47.70	24.64	13.76	10.00	0.00	0.00	0.00	0.00	3.90	0.00	0.00	0.00
S5T	41.52	31.24	10.70	3.51	0.00	0.00	0.00	0.00	7.46	0.82	1.90	2.85

Sample	Ca/P	STDCa/P	
S1	1.20	1.33	OCP
S1T	1.43	1.50	TOP
S2	1.03	1.00	DOPD/DOPA
S2T	2.61	2.00	TTCP
S3	1.28	1.33	OCP
S3T	2.43	2.00	TTCP
S4	1.05	1.00	DOPD/DOPA
S4T	2.53	2.00	TTCP
S5	1.38	1.33	OCP
S5T	3.05	2.00	TTCP

The following trends were observed as a result of the SBF treatment: (See orange region in Table 4.4). The at % of the O1s peaks decreased whilst those of C1s increased (except for the S2 SiO<sub>2</sub>-containing CaP system) indicating CO<sub>3</sub><sup>2-</sup> groups adsorbed onto the surface. The at. % of Ca2p increased with the treatment of systems S2 and S4 signaling a precipitation phenomenon from the SBF solution. Conversely, systems S1, S3, and S5 indicated a decrease in the at % of Ca2p suggesting the dissolution of these

ceramics in solution. With regards to the at % of P2p, this value decreases for all systems. This is thought to be due to the ACP adsorbate layer forming on the surface of the powders that is thick enough to obstruct the phosphate element detection by XPS. This possibly signifies a reorganization of phosphate groups on the surface of these materials.

The green area in Table 4.4 indicates the presence of the following ions on the surface of all the CaP T systems: Mg, Na, Cl, and N. Since these elements were not present in the NT powders, it is deducted that they originated from the SBF solutions. Ions of these elements form the constituents of the alkali salts that deposit onto the CaP surfaces via a precipitation process. Their presence was also confirmed by SEM and EDS analysis.

The yellow region of Table 4.4 demonstrates the presence of the “dopant” elements on the surfaces of each T system. A general decrease in at % for these elements occurs, (except for the S5 MgO-doped system). This decrease is explained by the dissolution of material or simply that XPS is not able to detect the “dopant” because of the large quantity of ACP material that deposits from the SBF solution.

With system S5 some peculiarities were noted. With treatment there was an increase in at % of the Mg element detected. This is a contrasting trend when compared to the other systems. Previous studies indicate that CaPs in aqueous media containing Mg form a very insoluble compound called Whitlocktite. In this study a similar event is believed to occur, i.e. the  $Mg^{2+}$  ions coming from the SBF solution bind to the powder surface to form salts, but more importantly rearrange to form Whitlocktite. Its formation is critical in inhibiting the precipitation of other surface bioactive apatite layers because this compound is highly

insoluble in aqueous media. This result explains the increased at % presence of this element on the surface of S5 after treatment.

The Ca/P at% ratios were calculated respectively for the untreated and treated systems. (See the blue region in Table 4.4. on page 47). It was found that the NT samples presented Ca/P ratios of less than 1.67 (the standard value for HA). These values ranged from 1.03 to 1.43 i.e. very close to other standard values for calcium phosphate materials e.g. octacalcium phosphate (OCP) = 1.33, dicalcium phosphate dihydrate (DCPD) and dicalcium phosphate anhydrous (DCPA) = 1.00. On this basis, systems S1, S3 and S5 tended to form an OCP-like compound on SHS synthesis whilst S2 and S4 formed DCPD/DCPA-like compounds.

The Ca/P ratios of the treated systems showed dramatic increases. These values ranged from 1.43 to 3.05. The standard Ca/P values for TCP and tetracalcium phosphate (TTCP) are respectively 1.50 and 2.00, and are much lower than those obtained experimentally. Literature reviews have also shown that carbonate and hydroxide ion substitutions within HA structures result in compounds with much higher Ca/P ratios (>2.00). Therefore, solely based on the Ca/P ratio calculated from XPS, S2 to S5 present values that could be attributed to the TTCP or HA/HCA structures, whilst the S1 system presents a Ca/P ratio closest to the TCP compound.<sup>39</sup>



#### 4.5. Inductively Coupled Plasma results.

Inductively coupled plasma (ICP) analysis was used to confirm the percentage of the elements present in the SBF samples after the 10-day treatment. These percentages were compared to the control SBF solution in order to determine whether either the dissolution or precipitation phenomenon occurred. If dissolution had occurred then an increase in the amount of elemental constituents would have been expected. Conversely, if the precipitation process had been manifested then a severe % elemental loss would be expected, as was the case. (See Figure 4.9. and Appendix 5 for the ICP data)

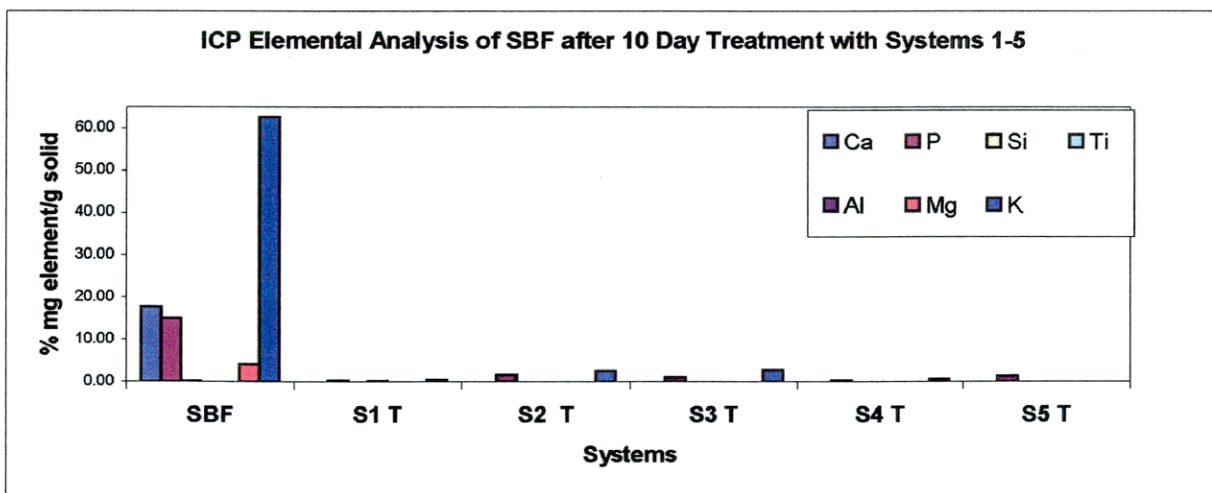


**Figure 4.9.** ICP analysis on the SBF solution after the 10-day treatment.

In fact, both phenomena had occurred, precipitation to the greater extent. A dramatic drop of all elements was seen when compared to their control SBF solution. This indicated the precipitation phenomenon as being predominant. The significant drop in Ca and P ions seen from SBF-treated samples indicated that precipitation occurred until equilibrium saturation. The “dopant” elements from each CaP chemistry are present only in trace amounts in the final SBF solutions. (See Appendix 5). This indicates that little or no dissolution of these phases occur. The presence of all these dopant materials in the final systems is evidence of slight cross contamination during the sample preparation stage of ICP. Perhaps improvements could be made on the handling of these samples during analysis. The low % of Na, Mg, K in the final SBF solutions indicated that deposition of alkaline salts is also a possibility on the surfaces of the CaP powders.

#### 4.6. Electron Dispersive Spectroscopy results.

The EDS module of the SEM was utilized to perform gross quantification of elements that might be present on the powder surfaces. The results of this study were as follows: the presence of (Na, Cl, and Mg) elements was detected on all surfaces and confirmed the precipitation of these species from the SBF solution. (See Figure 5.1. page 55)

In addition, the “dopant” elements present for each system did not vary in weight % (wt %) with SBF treatment, especially for S2 and S3. Systems S4 and S5 showed a decrease in their dopant element amounts. In the latter cases, this would signify dissolution of these CaP powders due to treatment. (See Appendix 6)

The surface wt % of Ca did not fluctuate much with treatment. Its slight increase, indicated its precipitation onto the surface of the CaPs. Conversely, the wt % of P decreased more significantly with treatment, indicating that the dissolution phenomenon was occurring.

Finally, when the Ca/P ratio was calculated, an increase in this ratio with treatment was identified (with exception for the S2 system). All other trends mentioned earlier in the above paragraphs showed good consistency with the XPS data trends.

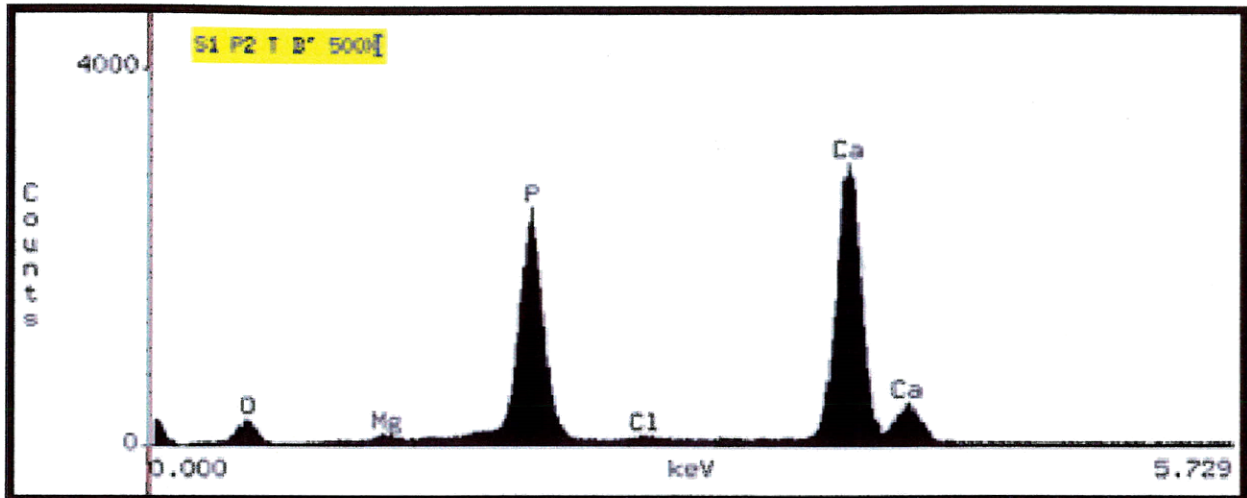


**Figure 5.0.** EDS analysis performed on the S1 T sample. Mg and Cl ions confirm the presence of salts on the surface that crystallize from the SBF solution.

#### 4.7. pH Data results

During the 10-day SBF treatment period, the pH of each system was recorded every six hours for the first day and from then on, once daily. The results of this study were as follows: (See Figure 5.1.) The S1 control chemistry was the least affected by the SBF treatment. In fact, this system shows negligible changes in pH with respect to the original pH of the SBF solution (pH = 7.25). Conversely, all other systems at different rates during the first day show an increase in pH. During this time frame, it is believed that the CaP powders react with the solution and release large quantities of OH<sup>-</sup> ions to increase its pH.

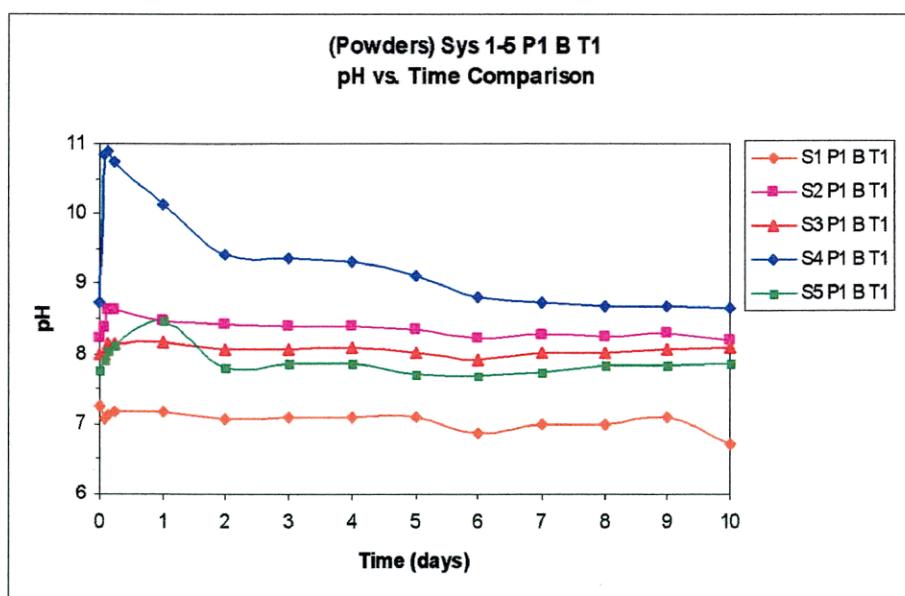


**Figure 5.1.** pH curves for S1-S5 during the 10-day SBF treatment.

Previous analyses of the powders produced via SHS have shown that they possess phase heterogeneity. The dissolution of the amorphous matrix contained in these powders is thought to be responsible for the increase in the pH values and the increase has occurred at different rates for the differing chemistries. The rates at which these surface precipitation reactions developed were estimated by determining how quickly each system reached its highest pH value. For example: S4 showed the highest change in pH value (The maximum being at pH=11) in the shortest amount of time. Systems S2, S3 and S5 reach similar pH values in the range of 8.0-8.5. Of these three systems, S2 seems to do so at the fastest rate. Finally, during and after the first day, all systems eventually “plateaued” to a stable pH value. S4 and S5 seem to require more time to reach this equilibrium state.

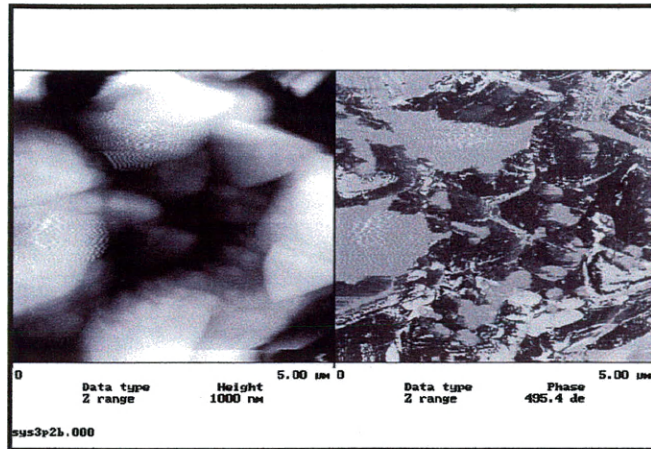
#### 4.8. Atomic Force Microscopy results.

Surface texture was observed using AFM. Surface irregularities can play an important role in the biological behavior of CaP materials, in particular surface roughness. A few studies have been made by the use of this technique on these compounds, but good atomic resolution is difficult to obtain. The produced pictures can be rather deceiving.

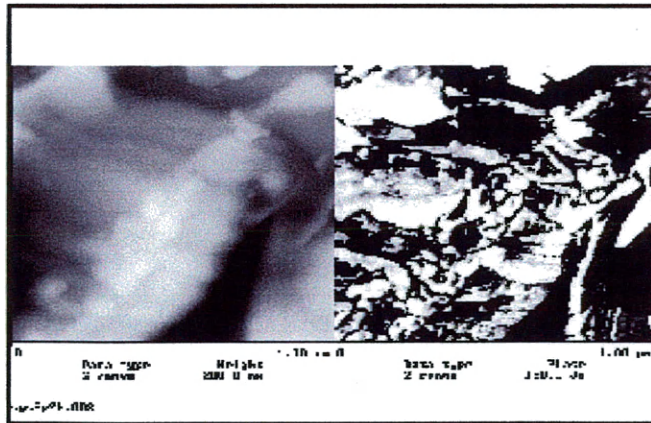
This was the case for our study (See Figure 5.3. on page 59). However, from this analysis, the heterogeneity of the powders was confirmed once again. Figure 5.3. (a) presents two types of surface features: straight-edged formations representing crystalline phases and rounder edges corresponding to amorphous phases.

Figure 5.3. (b) represents differences in structure in the powder. These features were measured by using a probe tip, scanning across the sample and detecting the electrostatic charges present on the surface. The computer is then able to process these signals and convert them into a graphical representation of structural differences across the whole powder.

Figure 5.4. shows similar information as Figure 5.3. but at a higher degree of magnification ( $1 \times 1 \mu\text{m}^2$ ), Figure 5.4. (a) provides an outline of a dendritic crystal. Perpendicular to the vertical axis of this feature, striations exist all along its length. This is an indication that crystal growth had occurred on these surfaces, more specifically of apatitic nature. Figure 5.4. (b) corresponds to its structural information.



**Figure 5.2.** (a) Shows the AFM analysis of a  $5 \times 5 \mu\text{m}^2$  area of the S3 NT system. (b) is a structural representation of this analysis.



**Figure 5.3.** (a) AFM analysis of a  $1 \times 1 \mu\text{m}^2$  area of the S3 NT system. (b) is a structural representation of this analysis.



## CHAPTER 5

### DISCUSSION AND CONCLUSIONS

It can be concluded that the entire five CaP based chemistries investigated in this study and produced via SHS are very heterogeneous materials. The SHS *untreated* samples all possessed varying amounts of the following CaP phases:  $\alpha$ -TCP,  $\beta$ -TCP, OCP, HA and HCA. XPS also determined the presence of two other CaP phases. These were DCPD and DCPA as identified by the matching of their Ca/P ratio with standard values. Nevertheless, the least heterogeneous material was found to be the control system (S1). This chemistry consisted predominantly of the  $\alpha$ -TCP phase. This was confirmed by the XRD and FTIR analyses. The SEM and pH data, determined that this phase ( $\alpha$ -TCP) was reluctant in forming a bioactive layer. This was confirmed by the lack of globular formations precipitated onto this surface and by the unvaried pH values when placed in the SBF treatment. Therefore, the question answered is: are the oxides in systems (S2-S5) important in determining the formation of the globular morphologies and hence in determining the material's bioactivity? Or, could the control system just require more time for the bioactive layer to form?

The *treated* chemistries also presented a high degree of structural heterogeneity. They too possessed  $\alpha$ -TCP,  $\beta$ -TCP, HA, and HCA phases. These were primarily identified by the XRD and FTIR techniques. XPS analysis allowed the identification of one other CaP phase i.e. TTCP. This is a high temperature phase that was expected to form during this type of high temperature synthesis reaction.

XRD confirmed an increase in peak areas and in the presence of new peaks pertaining to apatitic structures. This showed the treatment's involvement in the formation of a HA-like structure. However, the apatitic peaks identified were low in intensity and often too broad. This indicated that the layer forming on the surface exhibited some amorphous character. This conclusion is in accordance with previous studies i.e. for a bioactive layer to form, firstly an amorphous calcium phosphate layer must precipitate, and then, it later develops and mineralizes into its crystalline form.

FTIR identified characteristic HA and HCA peaks in both the *treated* and *subtracted* spectra for all the CaP systems. This confirmed the SBF treatment as having an effect on the powders produced via this method. Again, the control system constituted an exception, as these peaks were not detected. More importantly, this technique was extremely useful in determining the presence of both  $\text{CO}_3^{2-}$  and  $\text{OH}^-$  bond types in the treated samples. XPS confirmed the presence of the carbonate group by detecting the increase in C1s at % values with treatment. This information strongly indicated that a carbonate hydroxyapatite (HCA) had formed on the surface of these materials.

The types of HCA layers that have been known to form in these conditions are: of A-type, B-type or A/B-type-HCAs. A-type-HCAs represent apatitic layers in which the OH<sup>-</sup> species substitutes for the PO<sub>4</sub><sup>3-</sup> group, whilst B-type-HCAs are ones in which the CO<sub>3</sub><sup>2-</sup> species substitutes for the PO<sub>4</sub><sup>3-</sup> group. Both these substitutions occur in the A/B-type-HCAs, but are very hard to quantify.

The above FTIR data confirmed that all the CaP systems, except the control, showed the existence of these bond types only after SBF treatment. This suggests that the HCA layer that formed could be of A/B type. However, this was difficult to confirm in an absolute manner. So, a more detailed look was taken in the literature to attempt to understand the mechanisms that might be occurring.

Examination of the research literature indicated proposed that the complex substitution mechanisms involved in forming these A, B and A/B-type-HCA structures, could be reduced to linear combinations of six mechanisms.<sup>40</sup> These are shown in Table 5.1. on page 63. Mechanisms 1,2 and 5 represent the B-type CO<sub>3</sub><sup>2-</sup> species incorporation. Mechanism 3 involves the dual substitution of both alkali metal (M<sup>+</sup>) and CO<sub>3</sub><sup>2-</sup> ions. Mechanism 4 includes the sole incorporation of the M<sup>+</sup> ion whilst the A-type CO<sub>3</sub><sup>2-</sup> incorporation is represented by mechanism 6<sup>40</sup>.

Other studies have shown that HCAs prepared in aqueous solution closely resemble biological apatites in lieu of their metal and carbonate ion content. The carbonate species present in metal-HCA systems are known to predominantly substitute for phosphate groups i.e. B-type substitution. This incorporation mainly occurs independently with

mechanism 1 or it is coupled to the alkali metal mechanism 3. It should be noted that if sodium is involved, it is often incorporated in these apatite lattices in an independent manner according to mechanism 4. It is important to be aware of this, as this alkali metal is also involved in the mineral phase of biological calcifications.

**Table 5.1.** Six fundamental mechanisms believed to be involved in the formation of the HCA bioactive layers in biomaterials. ( $M^+$  = metal ion, V = vacancy).

Symbol	Fundamental Mechanism	Type of HCA produced
I	$Ca^{2+} + PO_4^{3-} + OH^- \leftrightarrow V^{Ca} + CO_3^{2-} + V^{OH}$	B-type
II	$Ca^{2+} + 2PO_4^{3-} \leftrightarrow V^{Ca} + 2CO_3^{2-}$	B-type
III	$Ca^{2+} + PO_4^{3-} \leftrightarrow M^+ + 2CO_3^{2-}$	M-B-type
IV	$Ca^{2+} + OH^- \leftrightarrow M^+ + V^{OH}$	M-type
V	$PO_4^{3-} \leftrightarrow CO_3^{2-} + OH^-$	B-type
VI	$2OH^- \leftrightarrow CO_3^{2-} + V^{OH}$	A-type

In this study, the experimental parameters were very similar to those mentioned in the above paragraph. The presence of alkali metals in an aqueous media (in this case SBF solution) would suggest that the HCA layer that formed in these conditions involves the incorporation of not only  $\text{CO}_3^{2-}$  and  $\text{OH}^-$  species, but also of  $\text{M}^+$  ions. Therefore, in our study it is believed a metal-HCA amorphous layer formed in the presence of the SBF solution. The formation of this bioactive layer would resemble very closely the structure of biological apatites and thus would indicate these materials as strong candidates for future medical applications.

The extent to which the powder substrates were covered by these HCA formations varied depending on the original CaP chemistry. The empirical ranking quantified this surface coverage and has allowed the determination of an order of bioactivity for these CaP systems based on the oxide they contain. The ranking was as follows: S3 ( $\text{TiO}_2$ ) > S4 ( $\text{Al}_2\text{O}_3$ ) > S2 ( $\text{SiO}_2$ ) > S5 ( $\text{MgO}$ ) > S1 (Control). Thus according to this ranking the  $\text{TiO}_2$ -based CaP systems proved to be the most bioactive and the Control system the least.

Finally, at the interface between the CaP material powder and the SBF solution both precipitation and dissolution reactions occurred. The predominant reaction was indeed the precipitation reaction. This was clearly seen in the ICP data. However, XPS and EDS data also confirmed that the reverse process could occur too i.e. the dissolution process in some instances. These phenomena are also very hard to quantify. However, the above general trends delineated that the above mechanisms were strongly involved in the formation of the ACP bioactive layer.

## CHAPTER 6

### FUTURE WORK

There is always room for improvement and so the following suggestions are made regarding future work that could be implemented from this study:

*Optimizing the reaction parameters.* In order to better control the SHS reaction products it is not only important to accurately determine the reactant chemistries, but also the reaction parameters e.g. temperature, pressure, power input etc. Being able to fix these parameters is essential for experimental reproducibility. The current experimental set-up necessitates this type of optimization in order to achieve this goal.

*Understanding of the mechanistic and kinetic aspects involved in the formation of the HCA bioactive layer.* In order to do so, other approaches must be taken, e.g., due to the similar structural features between the CaP phases, their characterization is extremely difficult. Hence, it would be wiser to adopt more sophisticated methods of analysis that permit a more detailed characterization of these powders on a “nano” scale. By doing so, it should be possible to accurately determine how each of the phases present in the CaP powders are directly linked to bioactivity. If these relationships are well understood, then it might be possible to envisage engineering specific materials surfaces, so that they possess particular bioactive functions.

*Increasing the statistical validity of this study.* This would further validate the trends observed above and can be achieved by increasing the number of samples manufactured and tested (increasing the n population tested).

The final suggestion for future work would be to investigate the validity of the SHS manufactured biomaterials via biocompatibility tests. These could be performed as a two-stage process: firstly by conducting initial *in-vitro* cell culture studies by subjecting the implants to osteoblastic and/or osteoclastic environments, and secondly, if successful, implanting the optimized materials into animals and humans for clinical trials.

## REFERENCES

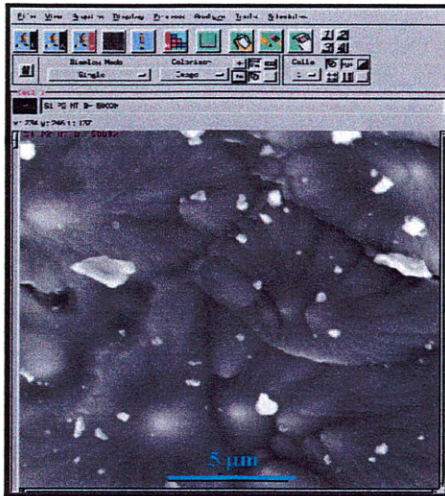
- (1) Elliott, J. C. *Structure and Chemistry of the apatites and the other calcium orthophosphates.*; Elsevier: Amsterdam, 1994.
- (2) Martini F.H.; Ober W.C.; Garrison C.W. *Fundamentals of Anatomy and Physiology*; 5th Edition ed.; Prentice Hall, 1998.
- (3) Rawlings, R. D. *Clinical Materials* **1993**, *14*, 155-179.
- (4) Hench, L. L. In *Society for Biomaterials 24th Annual Meeting*; Award, F., Ed.: San Diego, CA, 1998.
- (5) Heughebaert, J. C.; Zawacki, S. J.; Nancollas, G. H. *J Cryst Growth* **1983**, *63*, 83-90.
- (6) Slosarczyk, A.; Piekarczyk, J. *Ceramics International* **1999**, *25*, 561-565.
- (7) Legeros, R. Z.; Brown., B. P. *Biological and synthetic apatites. In hydroxyapatites and related compounds.*; CRC Press: Boca Raton, 1994.
- (8) Boskley, A. L. *Conn. Tissue Res.* **1996**, *35*, 357-363.
- (9) Woodhouse, K. A.; Weitz, J. I.; Brash, J. L. *J. Biomed. Mater. Res.* **1994**, *28*, 407-415.
- (10) Radin S., D. *J. Biomed. Mater. Res.* **1996**, *30*, 273-279.
- (11) Ijiri, S.; Nakamura, T.; Fujisawa, Y.; Hazama, M.; Komatsudani, S, J. *Biomed. Mater. Res.* **1997**, *35*, 421-432,
- (12) Brink, M.; Turunen, T.; Happonen, R.-P.; Yli-Urpo, A. J. *Biomed. Mater. Res.* **1997**, *35*, 114-121,
- (13) Moreno, E. C.; Kresak, M.; Zahradnick, R. T. *Caries Res* **1977**, *11*, 142-171.
- (14) Okazaki, M.; Moriwak, i. Y.; Aoba, T.; Doi, Y.; Takahashi, J. *Caries Res.* **1981**, *15*, 477-483.
- (15) Schroeder, L. W.; Dickens, B.; Brown, W. E. *J. Solid State Chem.* **1977**, *22*, 252-262.
- (16) Zahid, A. **1998**, 241-243.
- (17) Koerten, H. K.; Meulen, J. *J. Biomed. Mater. Res.* **1994**, *28*, 1455-1463.
- (18) Frassynet, P.; Rouquet, N.; Tourenne, F.; Fages, J., Hardy D.; Bone, l. G. *Cells and Materials* **1983**, *3*, 383-394.
- (19) Prudhommeaux F; Schiltz C; Loite' A; Hina A; Champy R; B, B. *Arth and Rheum* **1996**, *39*, 1319-1326.
- (20) Wilson, J. W. *Science* **1984**, 226-630.
- (21) Hench, L. L.; Splinter, R. J.; Allen, W. C.; Greenlee, T. K.; , () () *J. Biomed. Mater. Res.* **1971**, *2*, 117.
- (22) Hench, L. L. *J. Am. Ceram. Soc.* **1988**, *81*, 1705.
- (23) Kokubo, T.; Kushitani, H.; Sakka, S. *J. Biomed. Mater. Res.* **1990**, *24*, 721-734.



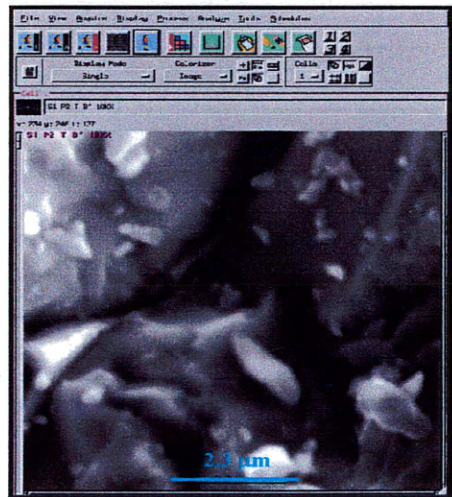
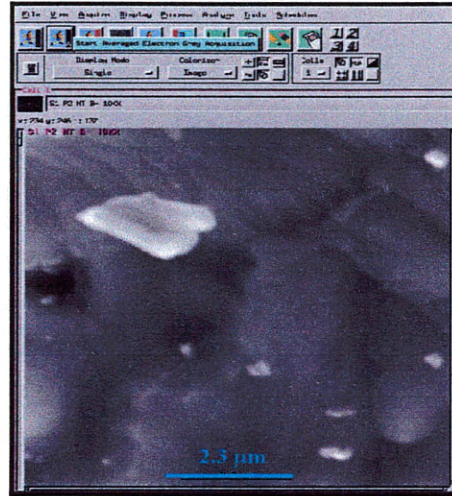
- (24) Kokubo, T.; Ito, S.; Huang, Z. T.; Hayashi, T.; Sakka, S. *J. Biomed. Mater. Res.* **1990**, *24*, 331-343.
- (25) Li, P.; Ohtsuki, C.; Kokubo, T.; Nakanishi, K.; Soga, N.; Nakamura, T.; Yamamuro, T. *J. Biomed. Mater. Res.* **1993**, *4*, 221-229.
- (26) Mullin, J. W. *Crystallization*; 2nd Ed. ed.; Butterworth: London, 1972.
- (27) Rizkalla, A. S.; Jones, D. W.; Clarke, D. B.; Hall, G. C. *J. Biomed. Mater. Res.* **1996**, *32*, 119-124.
- (28) Eidelmann, N.; Chow, L.; Brown, W. E. *Calcif. Tissue Int* **1987**, *40*, 71-78.
- (29) Christoffersen, M. R.; Christoffersen, J. *J. Cryst Growth* **1992**, *121*, 617-630.
- (30) Moreno, E. C.; Varughese, K. *J. Cryst Growth* **1981**, *53*, 20-30.
- (31) Amjad, Z. *Calcium Phosphates in biological and industrial systems*; Kluwer Academic Publishers, 1998.
- (32) Hanein, D.; Yarden, A.; Sabanay, H.; Addadi, L.; Geiger, B. *Cell Adhes Commun* **1996**, *4(4-5)*, 341-354.
- (33) Jha, L. J.; Santos, J. D.; Knowles, J. C. *J. Biomed. Mater. Res.* **1996**, *31*, 481-486.
- (34) Berger, G.; Giebler, M. *Phys. Stat. Sol (a)* **1984**, *53*, 86.
- (35) Leonelli, C.; Lusvardi, G.; Menabue, L. *J. Am. Ceram. Soc.* **2002**, *85*, 487-489.
- (36) Onuma, K.; Ito, A.; Tateishi, T.; Kameyama, T. *J. Cryst Growth* **1995**, *154*, 118-125.
- (37) Tancred, D. C.; McCormack, B. A. O.; Carr, A. J. *Biomaterials* **1998**, *19*, 1735-1743.
- (38) Florence; Boch *Biomaterials* **1998**, *19*, 1451-1454.
- (39) Heughebaert JC; Montel G *Calcif Tissue Int* **1982**, *34*, 103-108.
- (40) De Maeyer, E.; Verbeeck, R. *Bull. Soc. Chim. Belg.* **1993**, *102*, 601-609.

## APPENDIX 1 – SEM DATA

S1 NT [5000x]



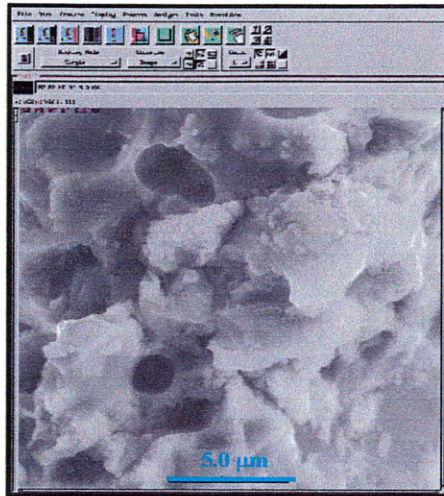
S1 NT [10000x]



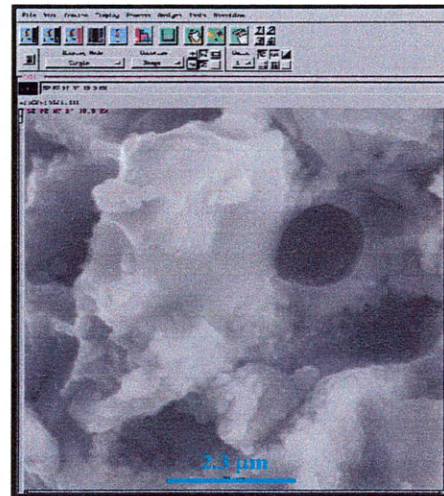
S1 T [5000x]

S1 T [10000x]

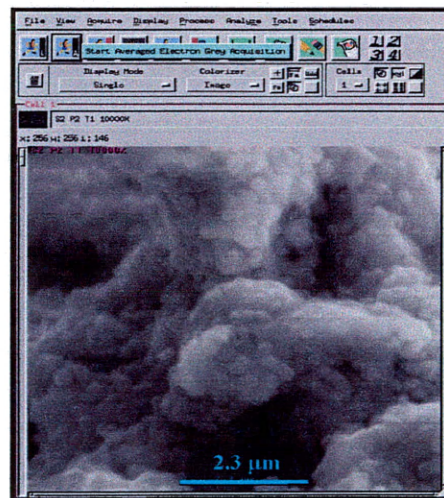
S2 NT [5000x]



S2 NT [10000x]

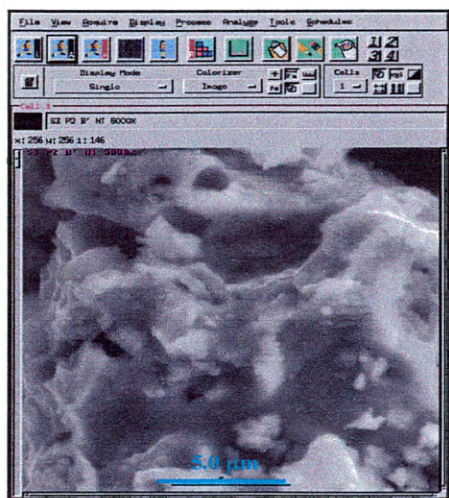
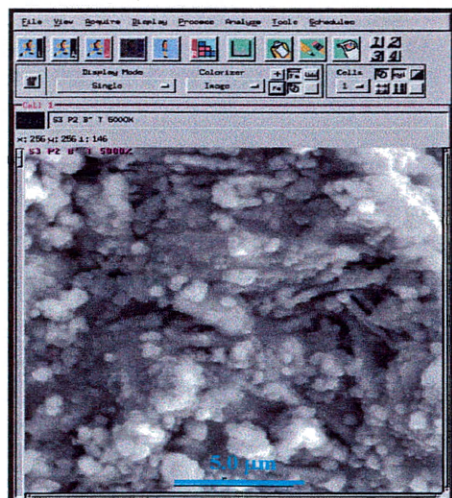
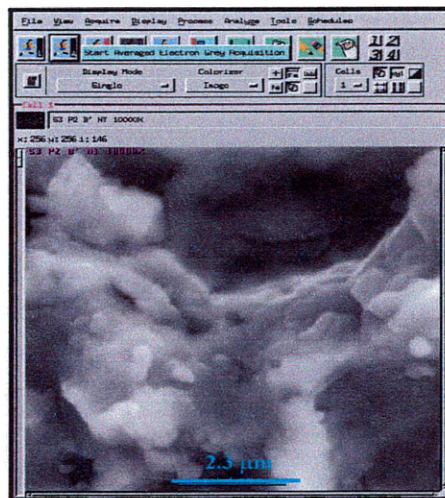
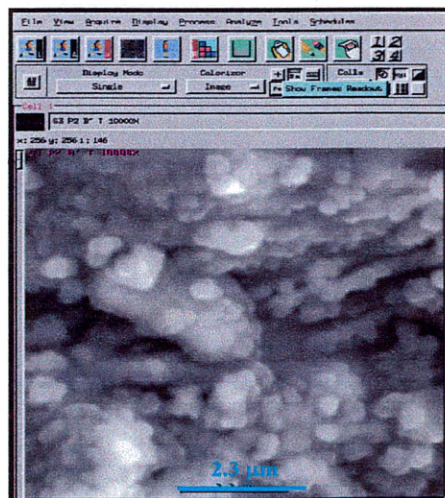


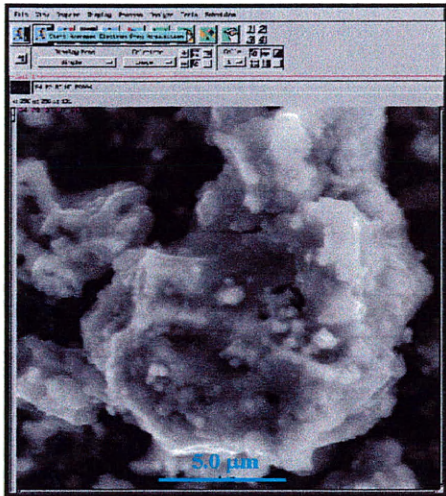
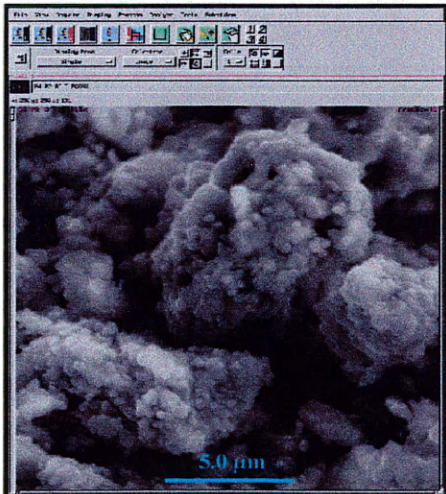
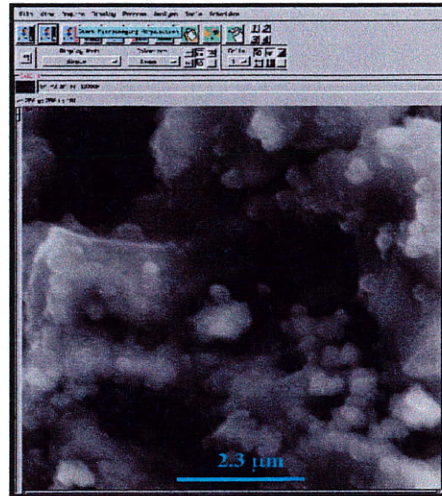
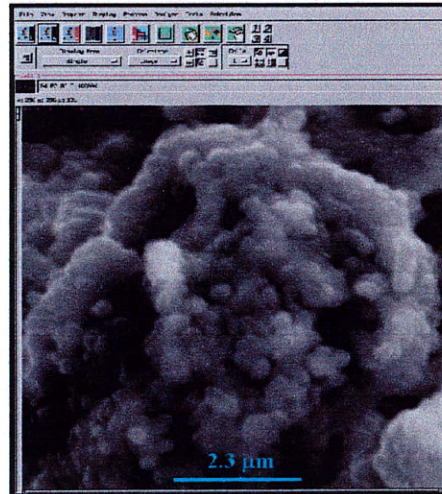
S2 T [5000x]



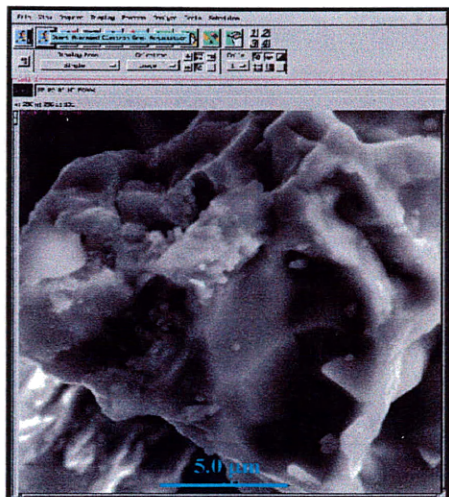
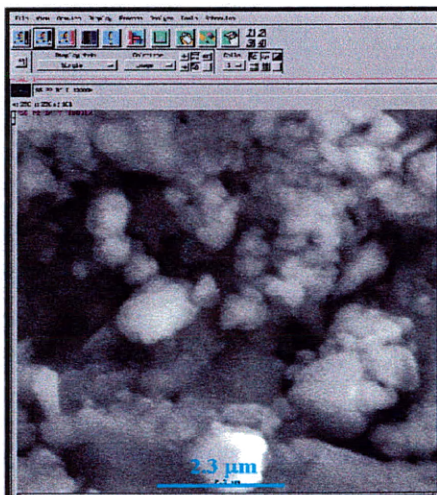
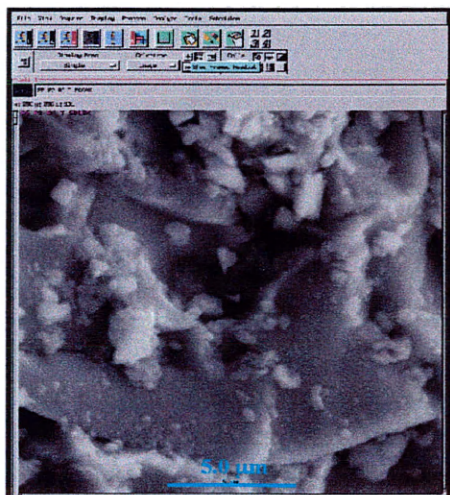
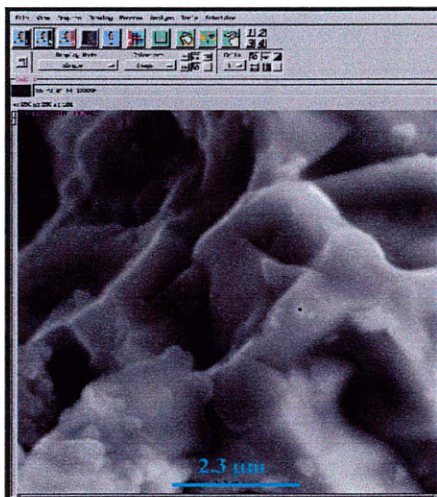
S2 T [10000x]



**S3 NT [5000x]****S3 NT [10000x]****S3 T [5000x]****S3 T [10000x]**

**S4 NT [5000x]****S4 NT [10000x]****S4 T [5000x]****S4 T [10000x]**



**S5 NT [5000x]****S5 NT [10000x]****S5 T [5000x]****S5 T [10000x]**

## APPENDIX 2 - XRD DATA

\*From Standard JCPDS Cards

<b>α1-TCP</b>		
Ranking	2θ	INT.(%)
1	30.753	100
2	34.182	50
3	22.723	40
4	22.902	40
5	24.098	40
6	30.601	35
7	31.249	30
8	34.604	30
9	12.097	25
10	22.206	20

<b>P<sub>2</sub>O<sub>5</sub></b>		
Ranking	2θ	INT.
1	29.416	999
2	22.971	781
3	32.457	765
4	15.672	567
5	24.843	520
6	24.049	460
7	26.416	455
8	36.727	398
9	19.294	377
10	42.084	141

<b>α2-TCP</b>		
Ranking	2θ	INT.(%)
1	30.709	100
2	22.89	48
3	34.209	43
4	22.765	41
5	12.101	39
6	24.105	33
7	34.466	29
8	22.138	24
9	31.26	24
10	30.346	20

<b>β-TCP</b>		
Ranking	2θ	INT.(%)
1	25.354	100
2	28.493	80
3	23.901	65
4	29.878	60
5	19.45	55
6	27.165	55
7	20.884	50
8	34.952	50
9	23.205	45
10	23.643	45

<b>SiO<sub>2</sub></b>		
Ranking	2θ	INT.
1	8.155	999
2	20.336	401
3	24.23	323
4	24.633	224
5	12.786	219
6	10.15	196
7	24.133	182
8	25.734	164
9	19.402	85
10	16.351	17

<b>CaP Silicate</b>		
Ranking	2θ	INT.
1	32.981	999
2	32.981	999
3	32.378	793
4	32.378	793
5	33.095	611
6	32.475	486
7	46.891	277
8	46.891	277
9	40.745	228
10	40.745	228

<b>HA artificial</b>		
Ranking	2θ	INT.(%)
1	31.661	999
2	32.767	723
3	32.148	703
4	10.79	492
5	46.563	337
6	25.879	237
7	34.004	229
8	49.412	226
9	39.632	209
10	22.796	162

<b>HCA</b>		
Ranking	2θ	INT.(%)
1	32.172	100.0
2	33.407	40.0
3	25.726	25.0
4	40.396	16.0
5	47.071	16.0
6	49.554	16.0
7	29.355	10.0
8	34.168	10.0
9	48.985	10.0
10	51.191	10.0

## 20 Rankings for the NT Samples

<b>S1 P2 B NT</b>		
Ranking	20	INT.(%)
1	30.751	100.0
2	34.157	86.6
3	22.756	75.0
4	24.109	42.6
5	12.046	32.7
6	22.196	29.5
7	17.095	27.1
8	27.799	25.6
9	29.701	23.2
10	14.045	19

<b>S3 P2 B NT</b>		
Ranking	20	INT.(%)
1	27.405	100.0
2	25.247	87.4
3	30.997	70.4
4	29.499	57.2
5	16.95	49.7
6	34.441	45.9
7	32.444	40.9
8	17.851	39.6
9	24.391	35.8
10	28.798	32.1

<b>S2 P2 B NT</b>		
Ranking	20	INT.(%)
1	26.599	100.0
2	34.297	35.7
3	30.95	30.4
4	27.7	27.1
5	17.948	26.5
6	29.598	25.9
7	20.75	20.8
8	31.758	20.8
9	28.849	17.9
10	25.751	14.6

<b>S4 P2 B NT</b>		
Ranking	20	INT.(%)
1	21.508	100.0
2	34.052	92.5
3	43.348	89.6
4	35.149	81.5
5	17.855	80.3
6	25.556	61.3
7	29.549	58.4
8	57.501	56.6
9	28.795	48.6
10	25.149	42.8

<b>S5 P2 B NT</b>		
Ranking	20	INT.(%)
1	31.148	100.0
2	34.697	48.3
3	27.998	44.5
4	25.797	37.8
5	17.049	34.9
6	13.597	20.6
7	47.348	18.9
8	53.153	18.7
9	32.65	14.4
10	42.852	13.6



## 20 Rankings for the T Samples

<b>S1 P2 B T</b>		
Ranking	20	INT.(%)
1	30.655	100.0
2	22.147	32.2
3	22.835	30.3
4	34.495	29.9
5	29.647	26.4
6	46.85	25.1
7	24.054	21.1
8	27.745	17.9
9	11.904	17.2
10	17.039	16.4

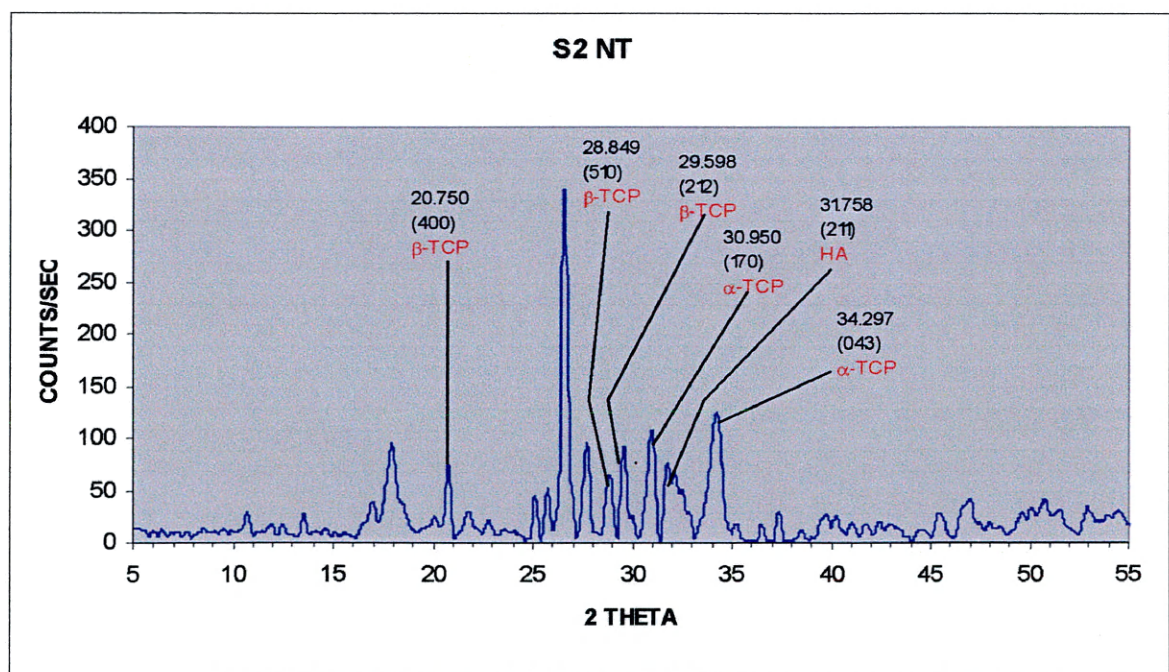
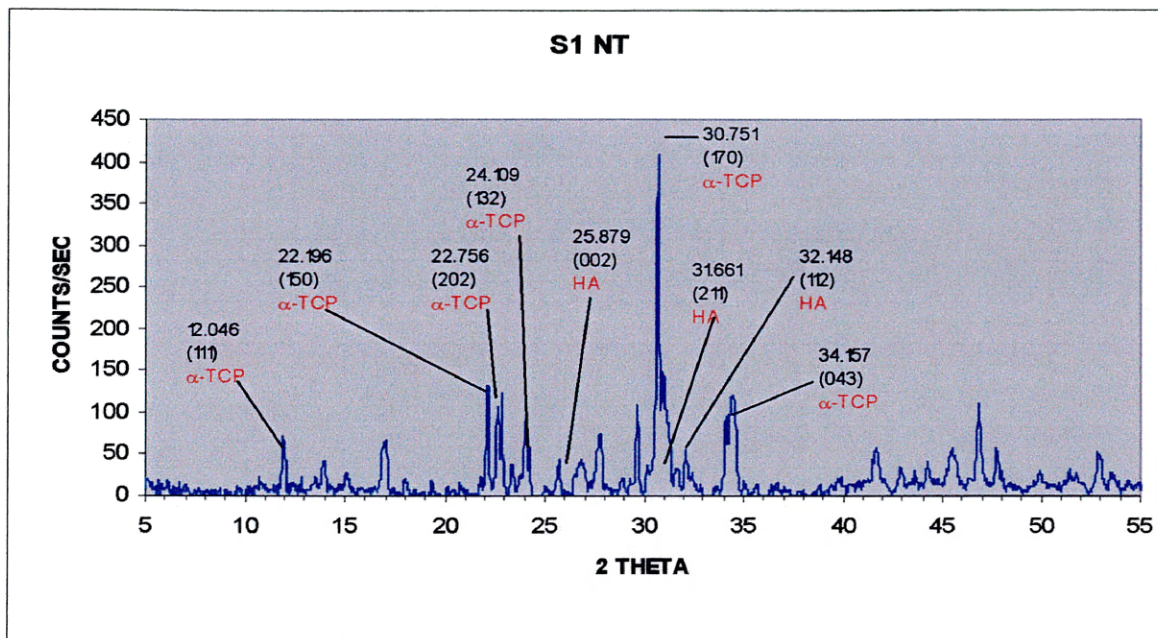
<b>S3 P2 B T</b>		
Ranking	20	INT.(%)
1	25.246	100.0
2	27.409	52.6
3	34.003	52.1
4	29.45	50.7
5	30.994	45
6	24.35	39.8
7	32.446	39.8
8	17.949	38.9
9	34.448	37
10	31.659	35.1

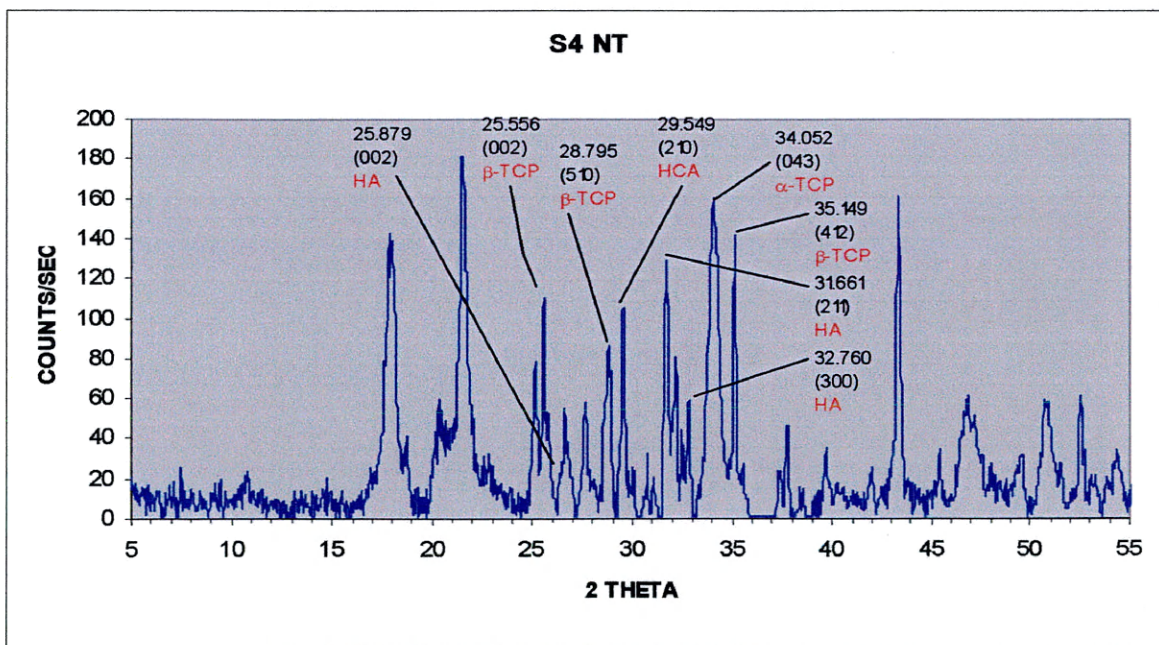
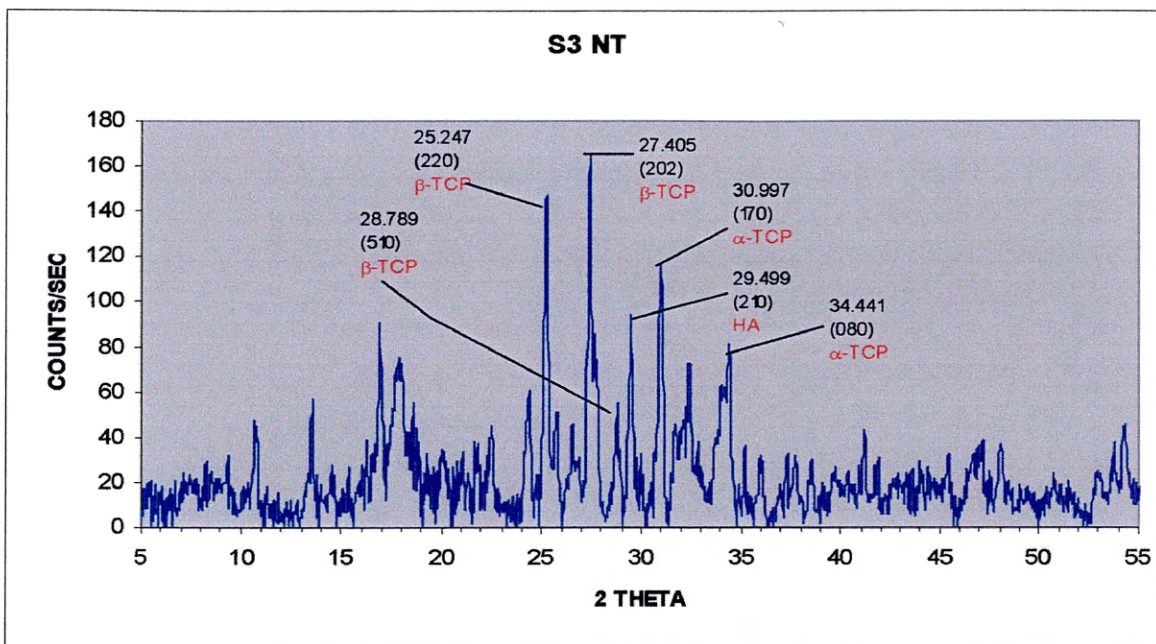
<b>S2 P2 B T</b>		
Ranking	20	INT.(%)
1	26.552	100.0
2	31.754	34.8
3	29.502	27.8
4	27.689	23.2
5	30.9	22.8
6	34.057	19.9
7	20.75	18.5
8	25.748	18.2
9	28.85	13.6
10	17.949	11.9

<b>S4 P2 B T</b>		
Ranking	20	INT.(%)
1	34.05	100.0
2	21.501	97.6
3	43.347	77.5
4	35.149	76.9
5	17.9	73.4
6	31.752	68.6
7	57.501	32.1
8	25.553	49.7
9	28.798	47.9
10	29.549	45.6

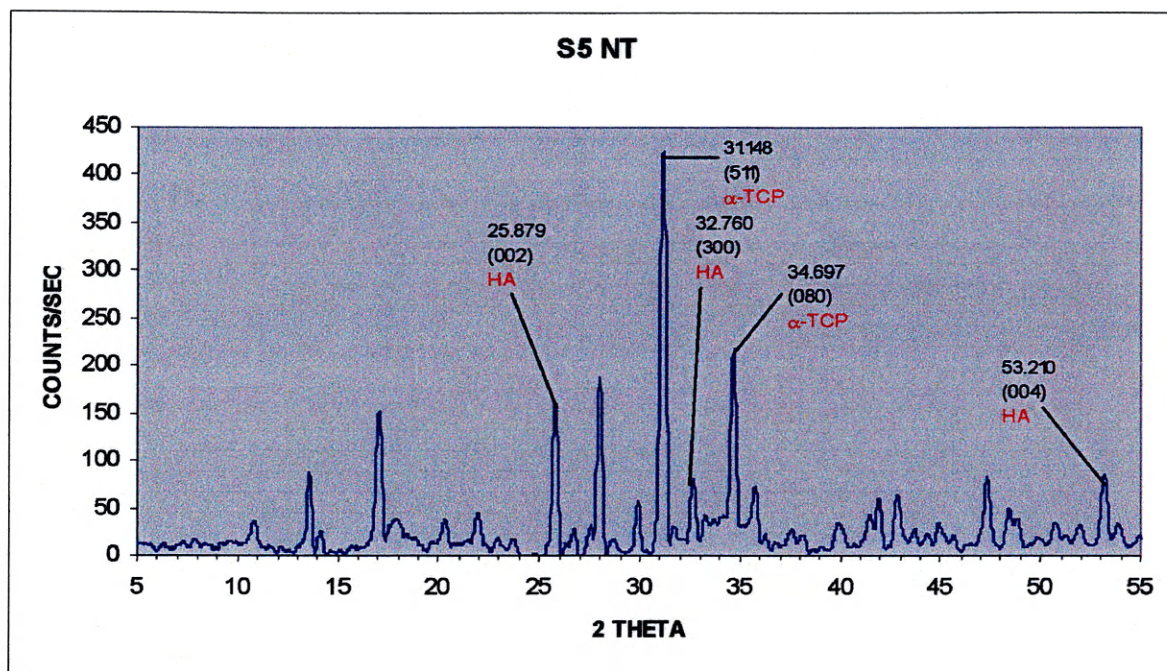
<b>S5 P2 B T</b>		
Ranking	20	INT.(%)
1	31.15	100.0
2	34.699	50.1
3	28	49.9
4	25.797	35
5	17.051	33.3
6	53.198	24.5
7	47.35	22.9
8	32.651	17.8
9	42.852	17.6
10	35.795	15.5

## NT SAMPLES

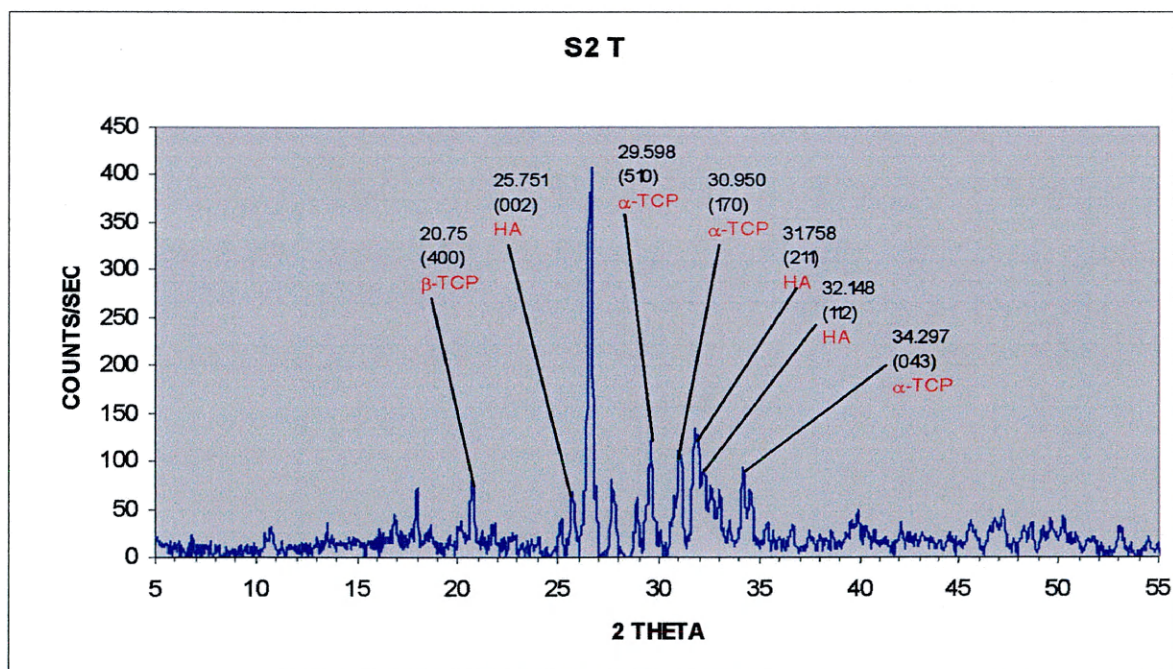
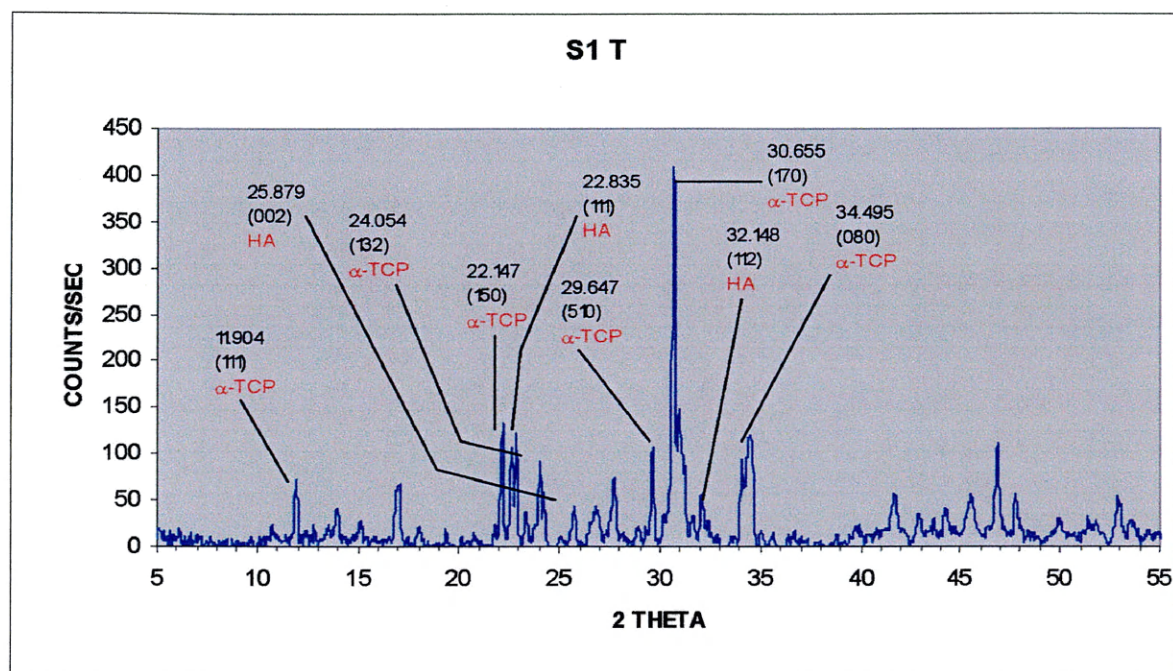




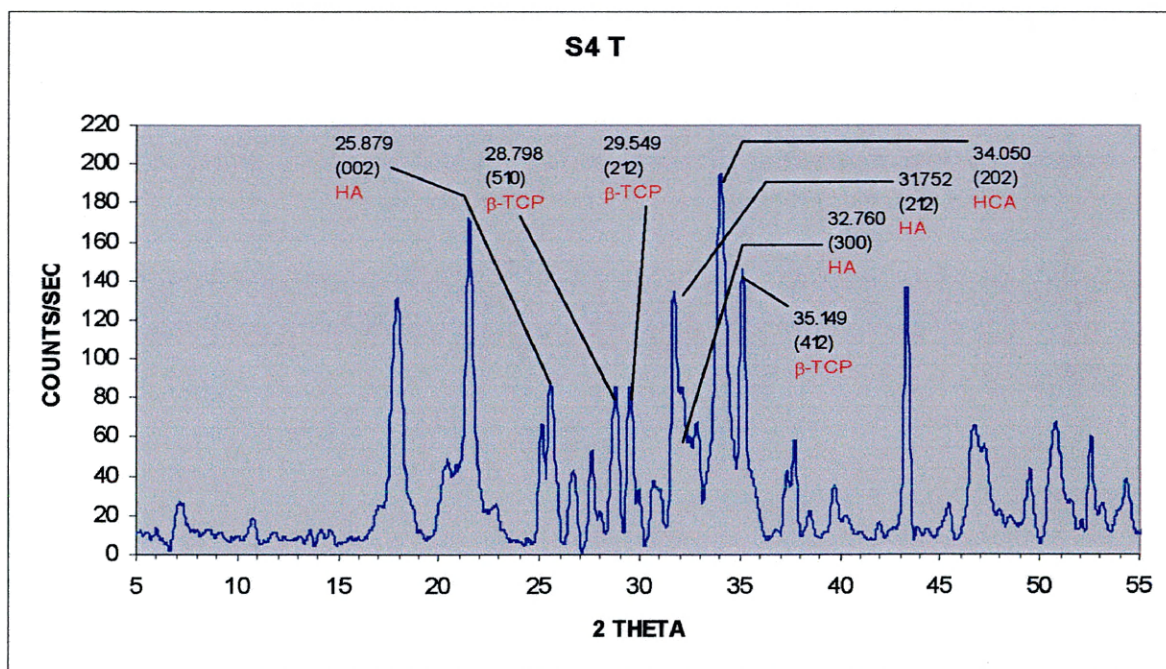
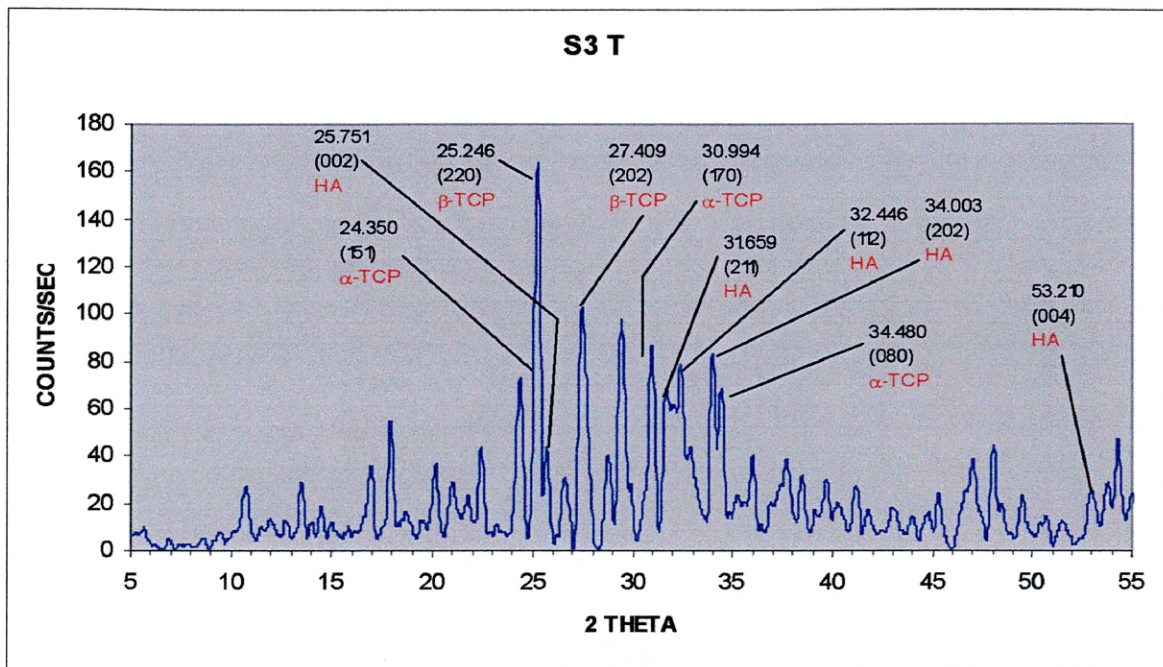


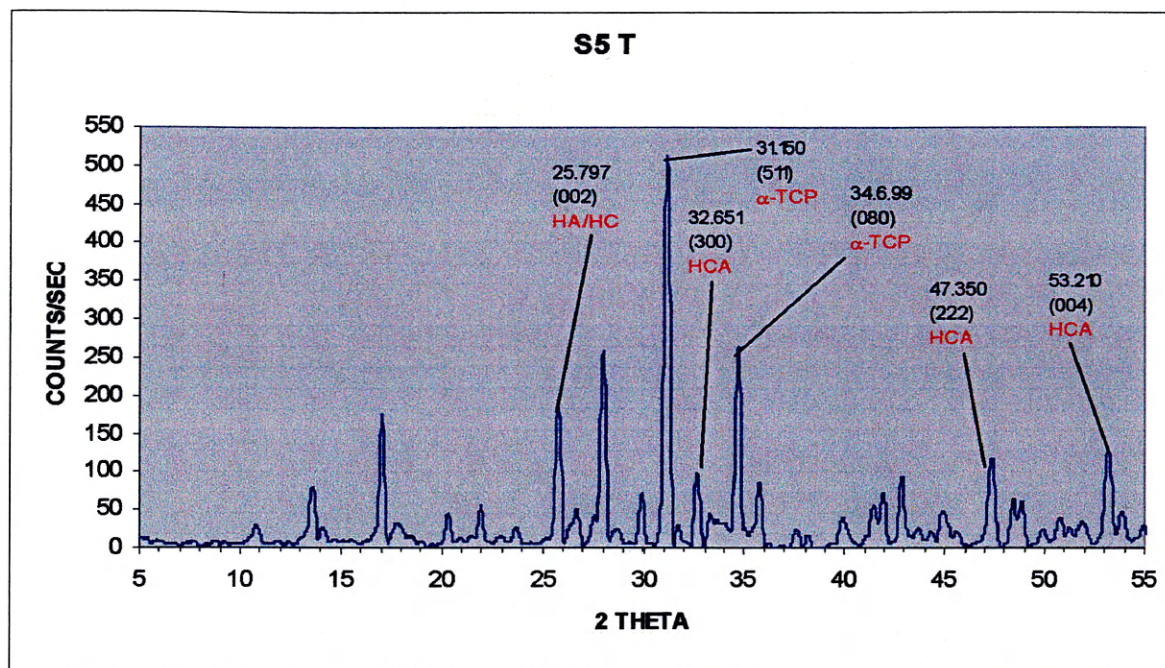


## T SAMPLES









## APPENDIX 3 – FTIR DATA

NT  
SAMPLES

Nat.HA	Cry. HA	a -TCP	b-TCP
3570.60	3571.60	3642.10	3571.30
1634.80			
1455.60			
1415.30			
		1186.00	
1091.30	1090.90		1119.20
1043.80	1044.00	1024.50	
962.30	962.70	988.20	970.40
		955.70	943.70
878.00			
630.20	632.90	610.20	604.80
602.80	602.90	594.60	
		582.60	571.40
565.60	566.10		551.90
472.10	473.20	443.70	

S1 P2 NT	CaO Std
	3642.01
	1421.21
1026.20	
756.45	
580.55	
554.14	
	440.97

S2 P2 NT	SiO2 Std
3642.64	
1214.19	
1160.91	1183.85
1063.90	1097.96
970.92	
939.55	
795.83	799.84
726.55	
564.24	
494.48	492.54
460.19	443.52





## T SAMPLES

Nat.HA	Cry. HA	a -TCP	b-TCP
3570.60	3571.60	3642.10	3571.30
1634.80			
1455.60			
1415.30			
		1186.00	
1091.30	1090.90		1119.20
1043.80	1044.00	1024.50	
962.30	962.70	988.20	970.40
		955.70	943.70
878.00			
630.20	632.90	610.20	604.80
602.80	602.90	594.60	
		582.60	571.40
565.60	566.10		551.90
472.10	473.20	443.70	

S1 P2 B1 T1	Sub S1	CaO Std
3643.71	3644.96	3642.01
		1421.21
	1161.06	
1026.20	1022.41	
756.28	703.99	
580.30	579.18	
554.75		
	465.17	440.97

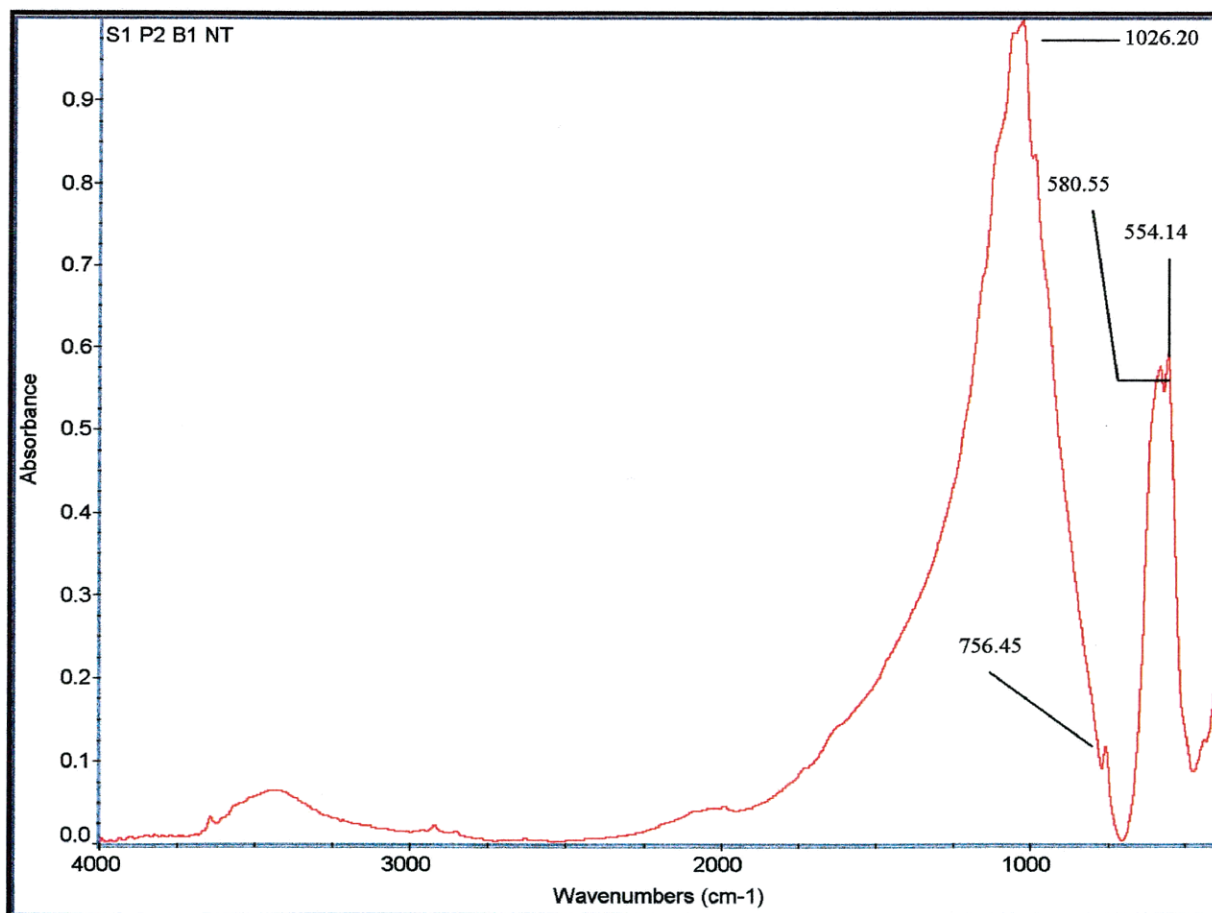
S2 P2 B1 T1	Sub S2	SiO2 Std
3643.04	3805.50	
3429.47	3687.50	
	3391.07	
	2361.61	
	1651.02	
	1462.75	
1426.90		1183.85
1214.05		
		1097.96
1042.45	1040.73	
971.07		
	871.65	
796.01	775.91	799.84
726.27	742.61	
605.40	606.27	
	576.83	
564.94		492.54
495.91		443.52

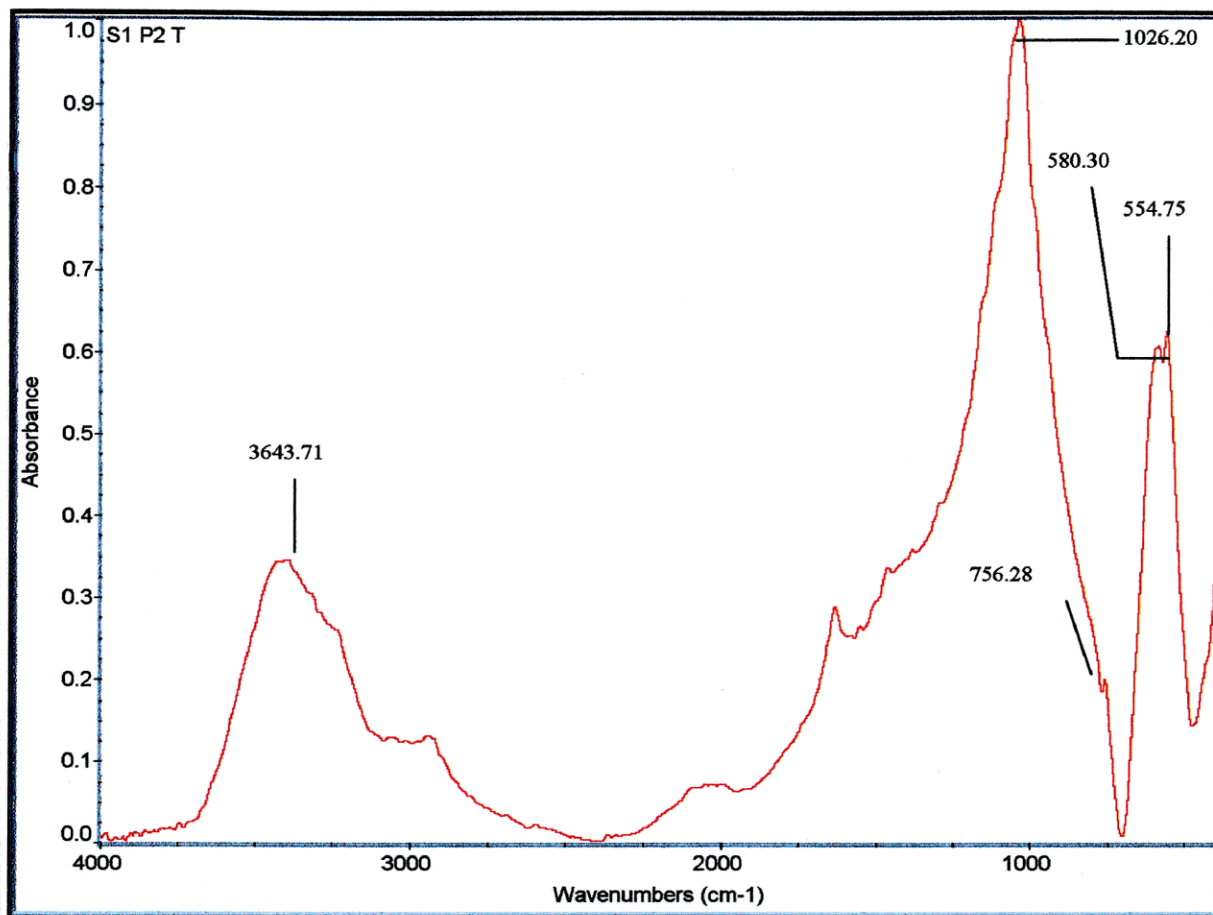
S3 P2 B1 T1	Sub S3	TiO2 Std
3642.67	3994.02	3435.23
3474.22	3501.17	
	3276.87	
1455.03		
1213.57		
1135.95		
1034.02		
972.33		
	829.17	
777.29	746.21	
725.48		
	673.95	689.79
604.62		
562.00	512.54	523.86
493.37	480.28	

S4 P2 B1 T1	Sub S4	Al2O3
3639.57 3482.31	3484.81	
1623.58		
1422.07	1424.17	
1214.18		
1043.63	1044.51	
970.48		
		801.07
783.74 724.75		741.80
		695.92 675.18
601.93	601.24	590.32
	572.06	
568.17		
453.40		466.26

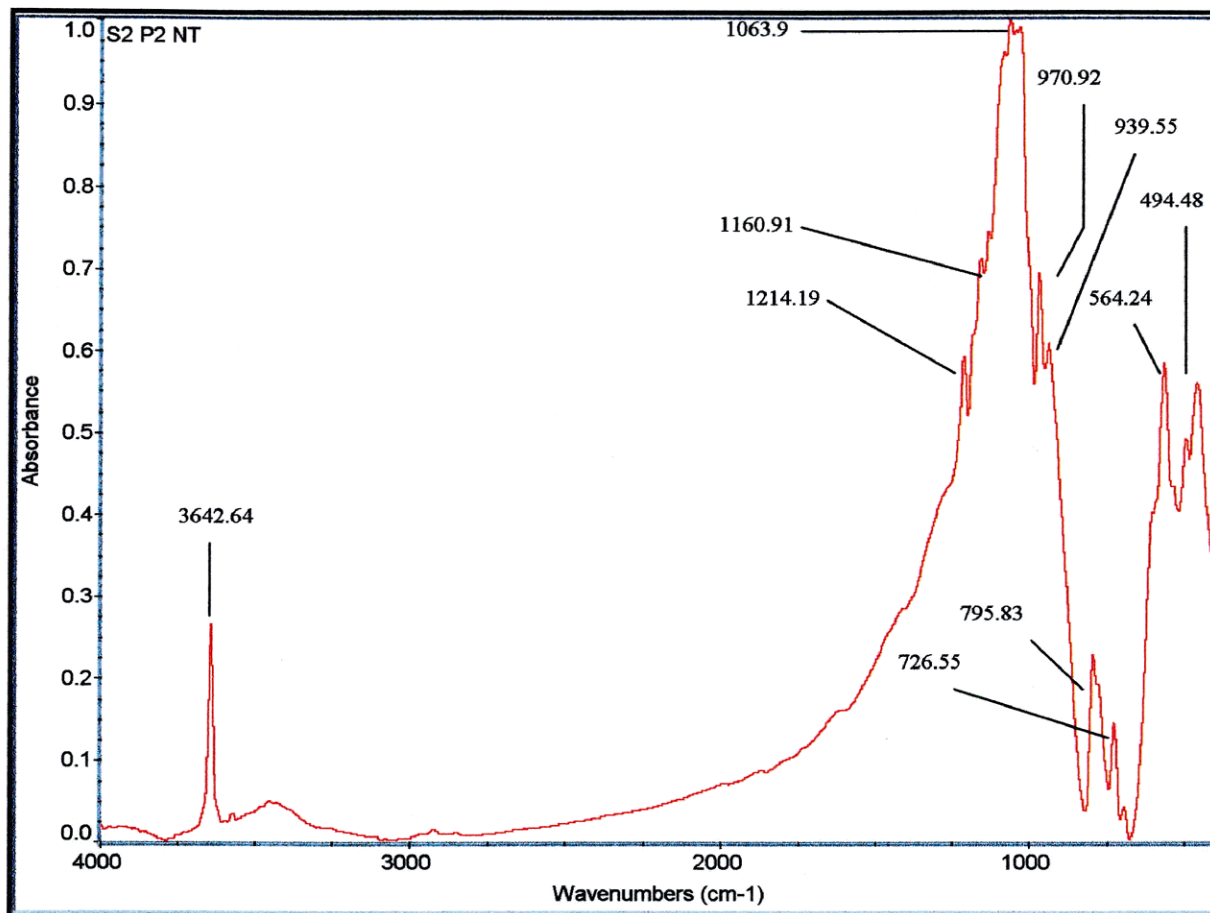
S5 P2 B1 T1	Sub S5	MgO Std
3433.21	3413.12 2918.07 2628.07	3451.46
2361.37	2360.71 2336.95	
1635.23	1635.25	
1456.44	1456.60	1456.87
	1210.79	
1123.03 1037.49	1158.74 1045.22	
	873.48 799.87	
	667.68 601.87	
601.53		
	572.42 527.15	
557.48		
413.96		419.56

Bond Description	Phase Identified	S1 NT	S1 T	Subtracted S1
$\text{PO}_4^{3-}$ $\gamma$ 3 P-O anti-sym stretch	$\alpha$ -TCP/CaO		3643.71	3644.96
$\text{PO}_4^{3-}$ $\gamma$ 3 P-O anti-sym stretch	$\alpha$ -TCP			1161.06
$\text{PO}_4^{3-}$ $\gamma$ 3 P-O anti-sym stretch	$\alpha$ -TCP	1026.20	1026.2	1022.41
	[?]	756.45	756.28	703.99
$\text{PO}_4^{3-}$ $\gamma$ 4 P-O anti-sym bend	$\alpha$ -TCP	580.55	580.3	579.18
$\text{PO}_4^{3-}$ $\gamma$ 4 P-O anti-sym bend	$\beta$ -TCP	554.14	554.75	
O-P-O Deformation				465.17

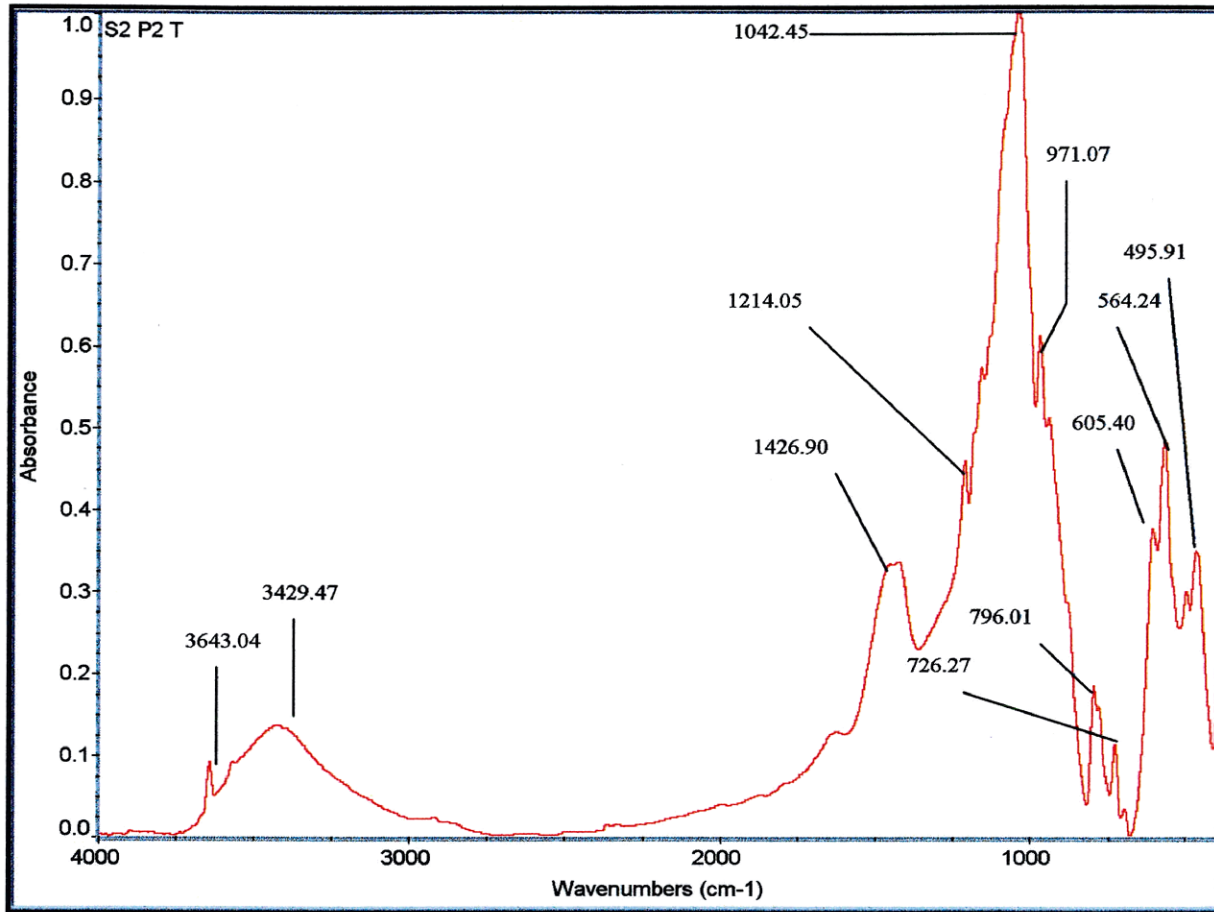




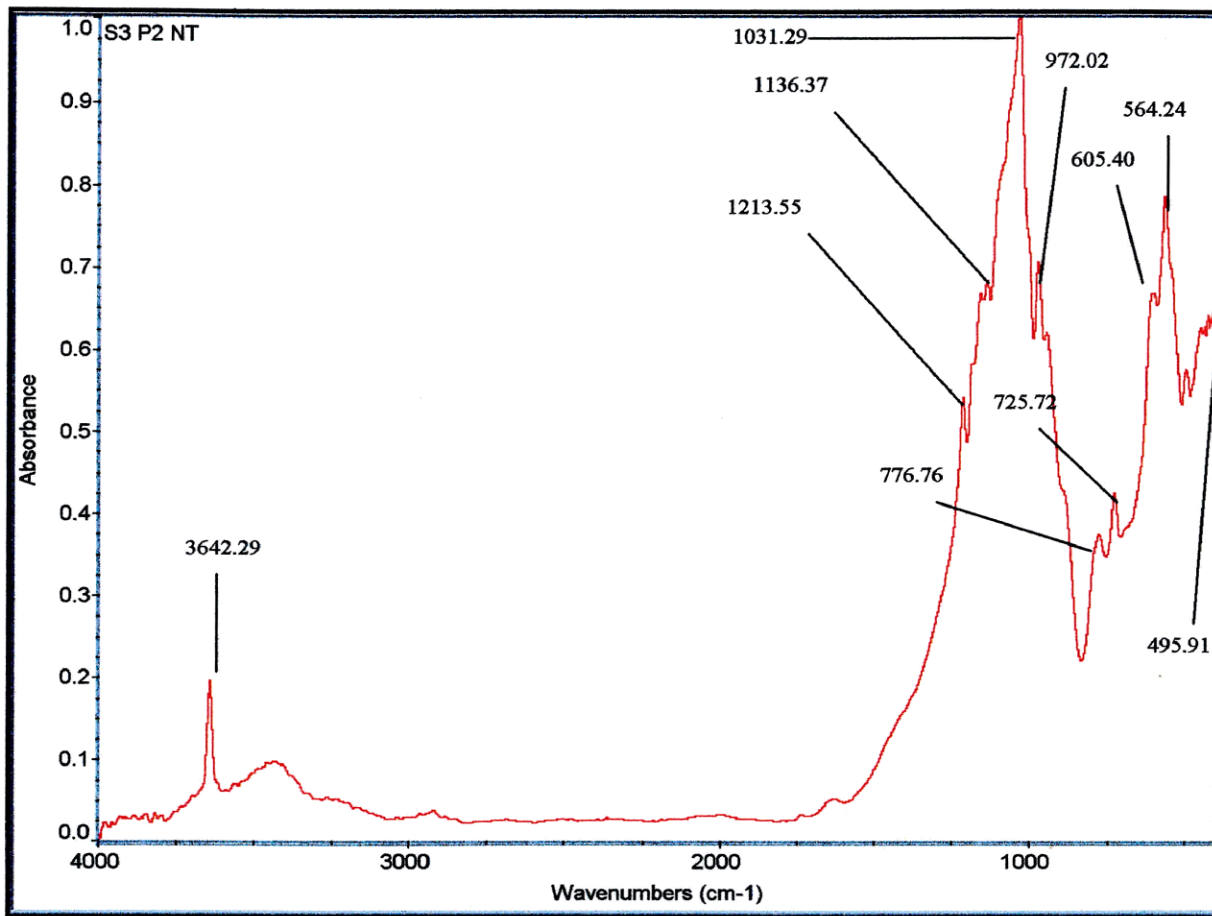
Bond Description	Phase Identified	S2 NT	S2 T	Subtracted S2
	$\alpha$ -TCP/CaO	3642.64	3643.04	3805.50
<b>OH Stretch/O-H-O stretch</b>	<b>HA</b>		<b>3429.47</b>	<b>3687.50</b>
	<b>Hydrocarbon</b>			3391.07
<b>CO<sub>2</sub></b>	<b>HCA</b>			<b>2361.61</b>
<b>CO<sub>3</sub></b>	<b>HCA</b>			<b>1651.02</b>
<b>CO<sub>3</sub></b>	<b>HCA</b>		<b>1426.9</b>	<b>1462.75</b>
<b>PO<sub>4</sub><sup>3-</sup> <math>\gamma</math>3 P-O anti-sym stretch</b>	$\alpha$ -TCP	1160.91	1214.05	
<b>PO<sub>4</sub><sup>3-</sup> <math>\gamma</math>3 P-O anti-sym stretch</b>	<b>HA</b>	<b>1063.90</b>	<b>1042.45</b>	<b>1040.73</b>
<b>PO<sub>4</sub><sup>3-</sup> <math>\gamma</math>1 P-O sym stretch</b>	$\beta$ -TCP	970.92	971.07	
<b>PO<sub>4</sub><sup>3-</sup> <math>\gamma</math>1 P-O sym stretch</b>	$\beta$ -TCP	939.55		
<b>CO<sub>3</sub></b>	<b>HCA</b>			<b>871.65</b>
	[?]	795.83	796.01	775.91
	[?]	726.55	726.27	742.61
<b>PO<sub>4</sub><sup>3-</sup> <math>\gamma</math>4 P-O anti-sym bend</b>	$\beta$ -TCP		605.4	606.27
<b>PO<sub>4</sub><sup>3-</sup> <math>\gamma</math>4 P-O anti-sym bend</b>	$\beta$ -TCP			576.83
<b>PO<sub>4</sub><sup>3-</sup> <math>\gamma</math>4 P-O anti-sym bend</b>	<b>HA</b>	<b>564.24</b>	<b>564.94</b>	
<b>O-P-O Deformation</b>		494.48	495.91	

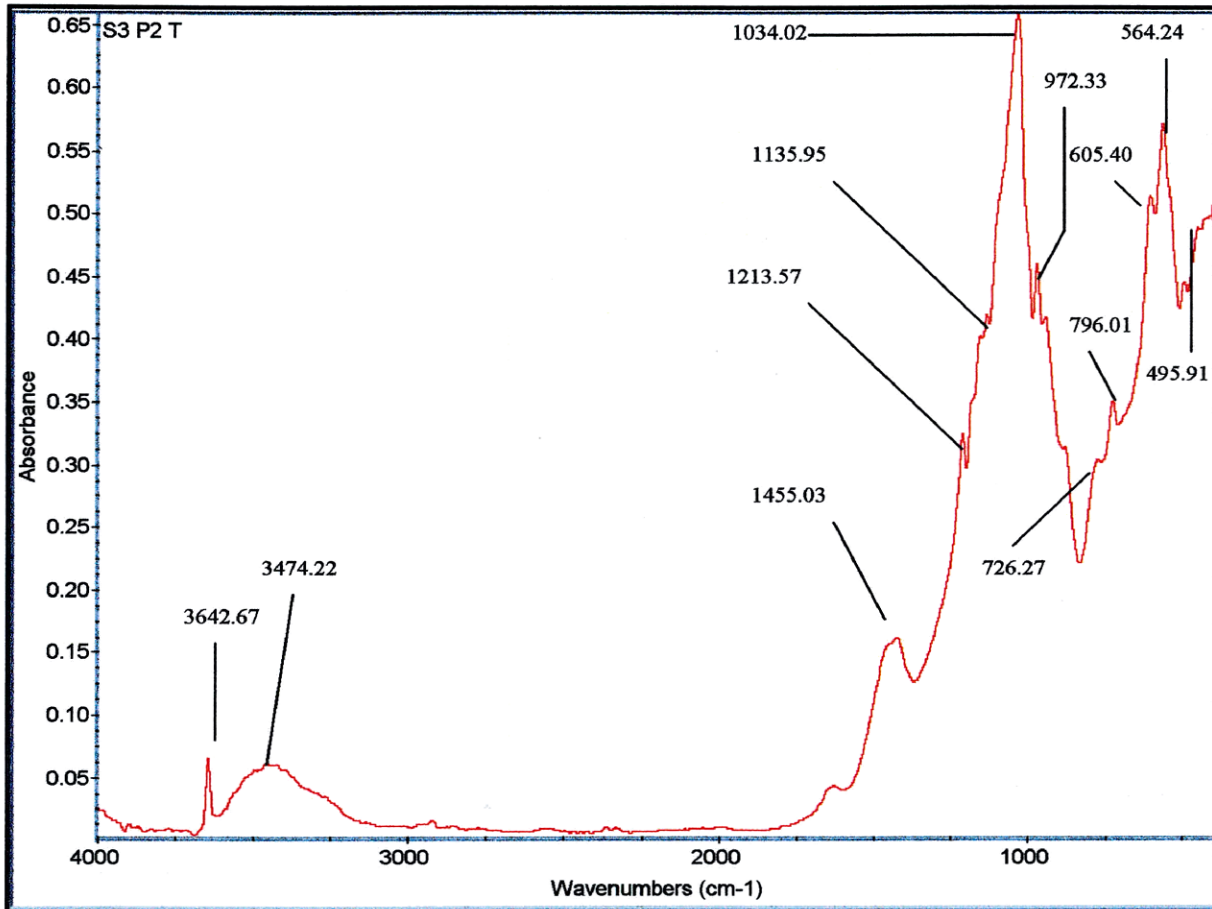




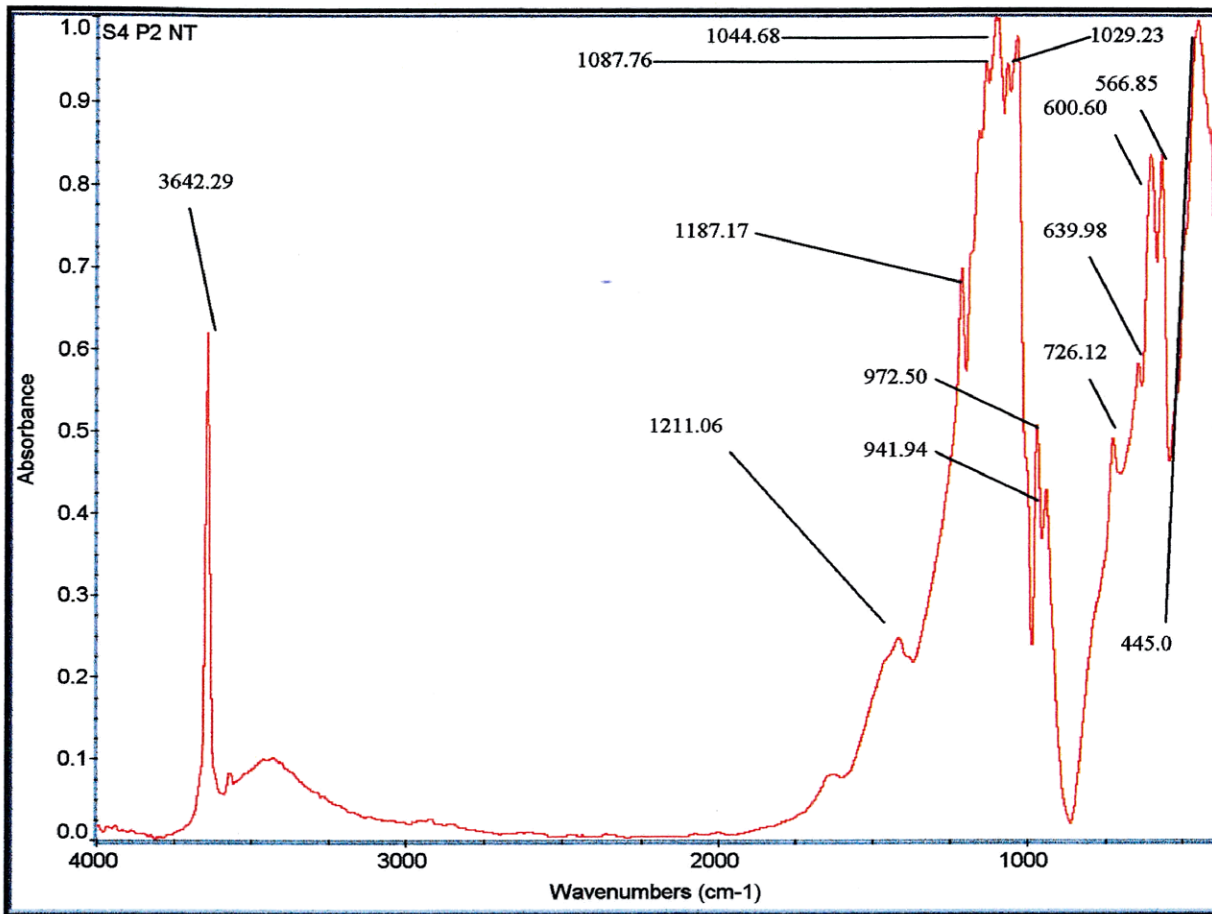


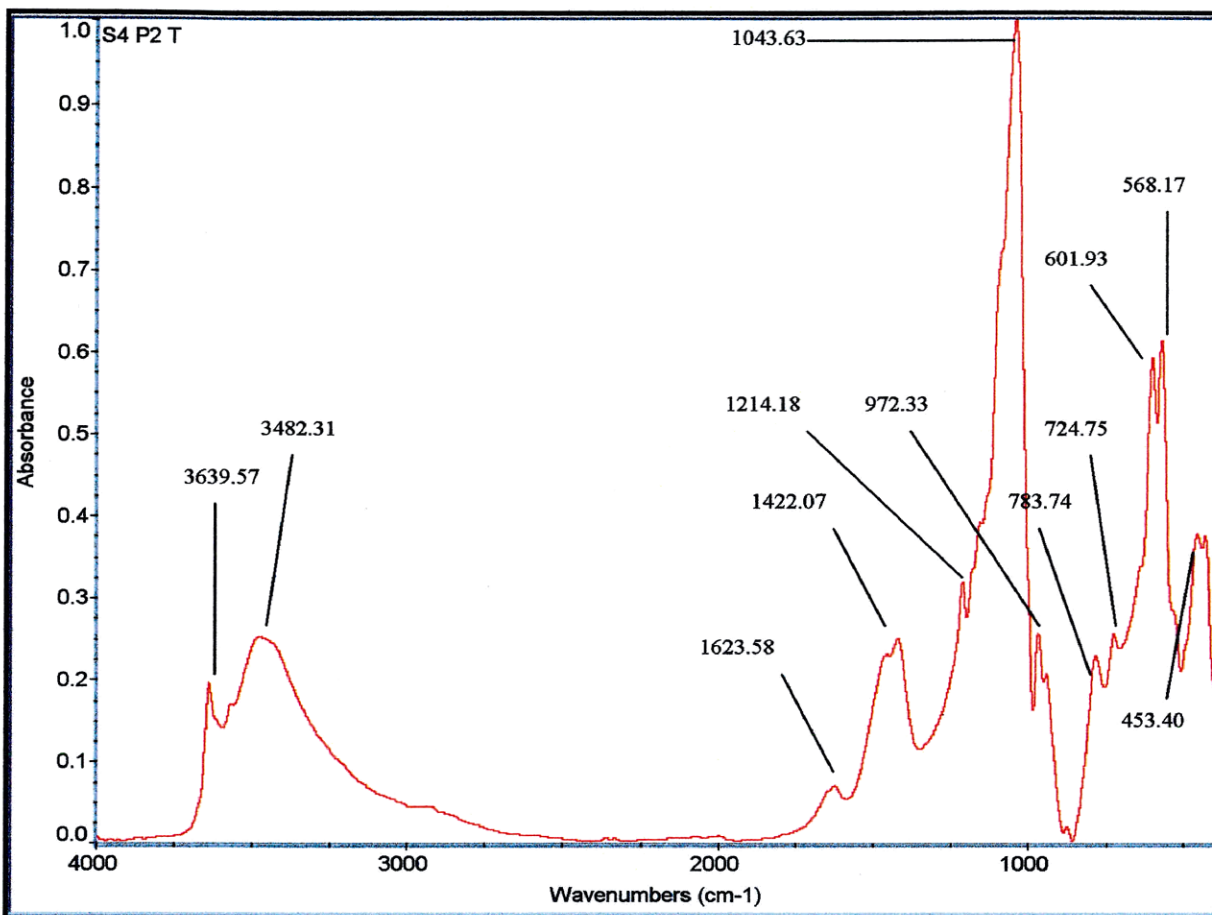
Bond Description	Phase Identified	S3 NT	S3 T	Subtracted S3
	$\alpha$ -TCP/CaO	3642.29	3642.67	3994.02
OH Stretch/O-H-O stretch	HA		3474.22	3501.17
	Hydrocarbon			3276.87
CO <sub>3</sub>	HCA		1455.03	
CO <sub>3</sub>	HCA	1213.55	1213.57	
PO <sub>4</sub> <sup>3-</sup> $\gamma$ 3 P-O anti-sym stretch	$\beta$ -TCP	1136.37	1135.95	
PO <sub>4</sub> <sup>3-</sup> $\nu$ 3 P-O anti-sym stretch	HA	1031.29	1034.02	
PO <sub>4</sub> <sup>3-</sup> $\gamma$ 1 P-O sym stretch	$\beta$ -TCP	972.02	972.33	
PO <sub>4</sub> <sup>3-</sup> $\gamma$ 1 P-O sym stretch	$\beta$ -TCP			
CO <sub>3</sub>	HCA			829.17
	[?]	776.76	777.29	746.21
	[?]	725.72	725.48	673.95
PO <sub>4</sub> <sup>3-</sup> $\gamma$ 4 P-O anti-sym bend	$\beta$ -TCP		604.62	
PO <sub>4</sub> <sup>3-</sup> $\gamma$ 4 P-O anti-sym bend	$\alpha$ -TCP	597.97		
PO <sub>4</sub> <sup>3-</sup> $\gamma$ 4 P-O anti-sym bend	HCA	561.18	562.00	
O-P-O Deformation		493.86	493.37	480.28





Bond Description	Phase Identified	S4 NT	S4 T	Subtracted S4
	$\alpha$ -TCP/CaO	3642.89	3639.57	3484.81
<b>OH Stretch/O-H-O stretch</b>	<b>HA</b>		<b>3482.31</b>	
	<b>Hydrocarbon</b>			
<b>CO<sub>3</sub></b>	<b>HCA</b>		<b>1623.58</b>	
<b>CO<sub>3</sub></b>	<b>HCA</b>		<b>1422.07</b>	<b>1424.17</b>
<b>PO<sub>4</sub><sup>3-</sup> v3 P-O anti-sym stretch</b>	$\alpha$ -TCP	1211.06	1214.18	
<b>PO<sub>4</sub><sup>3-</sup> <math>\gamma</math>3 P-O anti-sym stretch</b>	<b>HA</b>	<b>1087.76</b>		
<b>PO<sub>4</sub><sup>3-</sup> <math>\gamma</math>3 P-O anti-sym stretch</b>	<b>HA</b>	<b>1044.68</b>	<b>1043.63</b>	<b>1044.51</b>
<b>PO<sub>4</sub><sup>3-</sup> <math>\gamma</math>1 P-O sym stretch</b>	$\alpha$ -TCP	1029.23		
<b>PO<sub>4</sub><sup>3-</sup> <math>\gamma</math>1 P-O sym stretch</b>	$\alpha$ -TCP	1187.17		
	[?]		783.74	
	[?]	726.12	724.75	
<b>PO<sub>4</sub><sup>3-</sup> <math>\gamma</math>4 P-O anti-sym bend</b>	$\beta$ -TCP	972.50	970.48	
<b>PO<sub>4</sub><sup>3-</sup> <math>\gamma</math>4 P-O anti-sym bend</b>	$\beta$ -TCP	941.94		
<b>PO<sub>4</sub><sup>3-</sup> <math>\gamma</math>4 P-O anti-sym bend</b>	<b>HA</b>	639.98		
<b>PO<sub>4</sub><sup>3-</sup> <math>\gamma</math>4 P-O anti-sym bend</b>	<b>HCA</b>	<b>600.60</b>	<b>601.93</b>	<b>601.24</b>
<b>PO<sub>4</sub><sup>3-</sup> <math>\gamma</math>4 P-O anti-sym bend</b>	$\beta$ -TCP			572.06
<b>PO<sub>4</sub><sup>3-</sup> <math>\gamma</math>4 P-O anti-sym bend</b>	<b>HA</b>	<b>566.85</b>	<b>568.17</b>	
<b>O-P-O Deformation</b>		445.07	453.4	

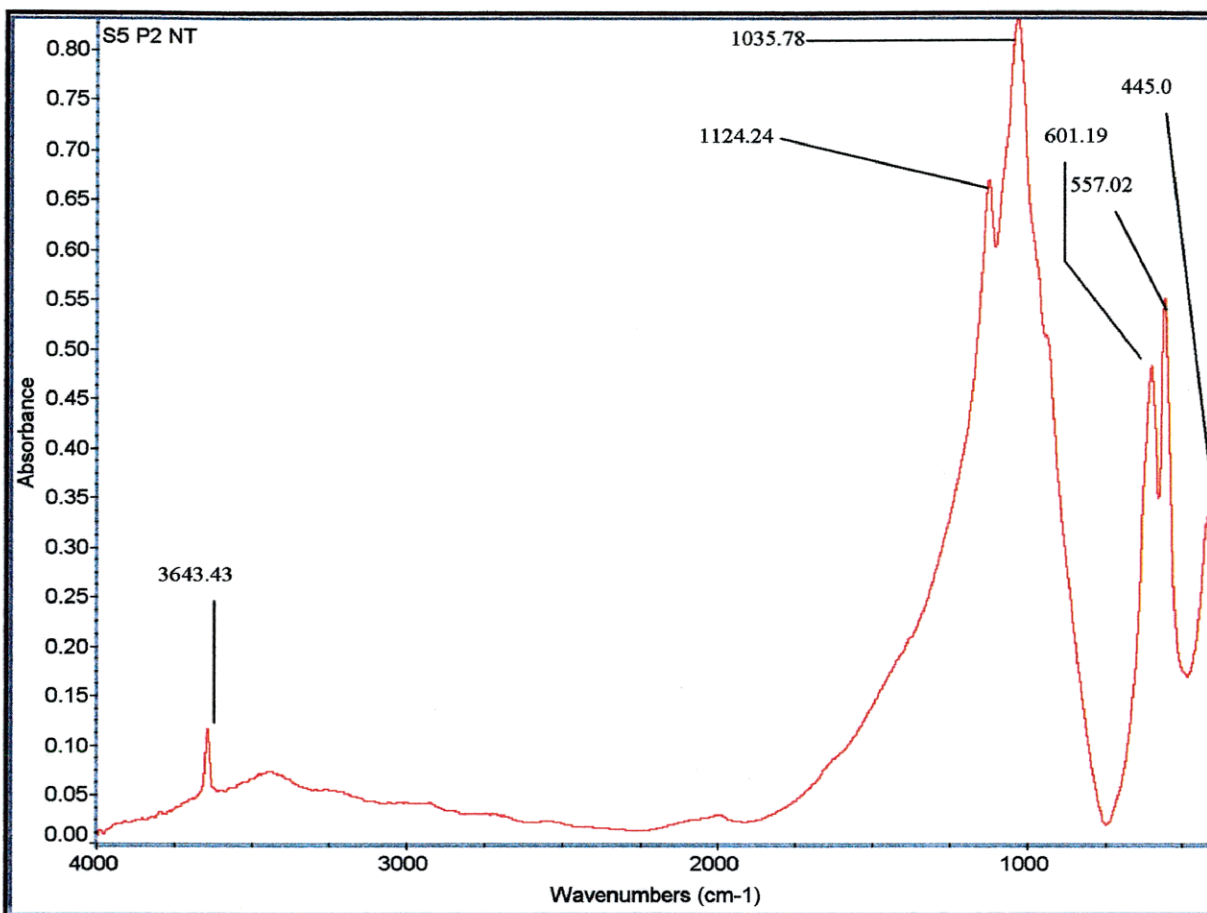


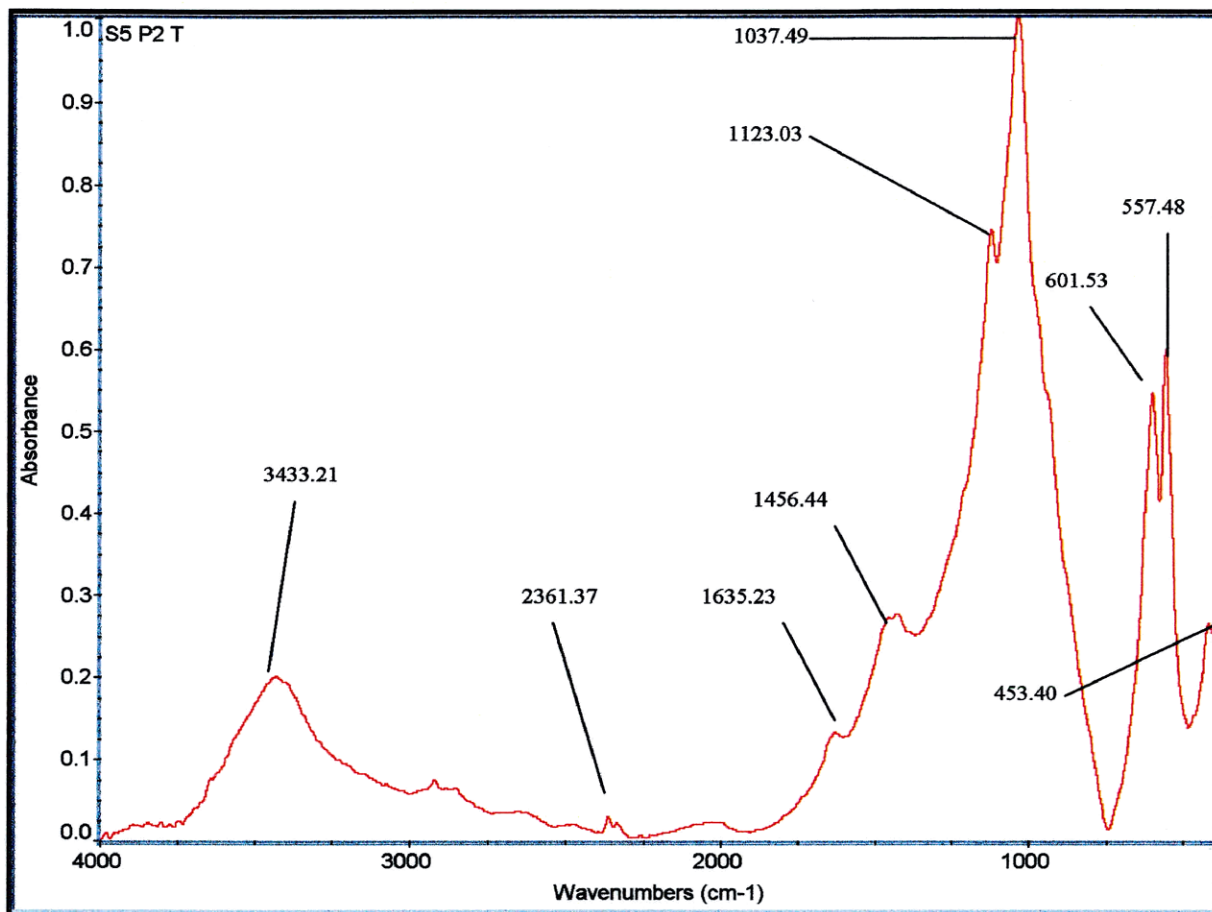


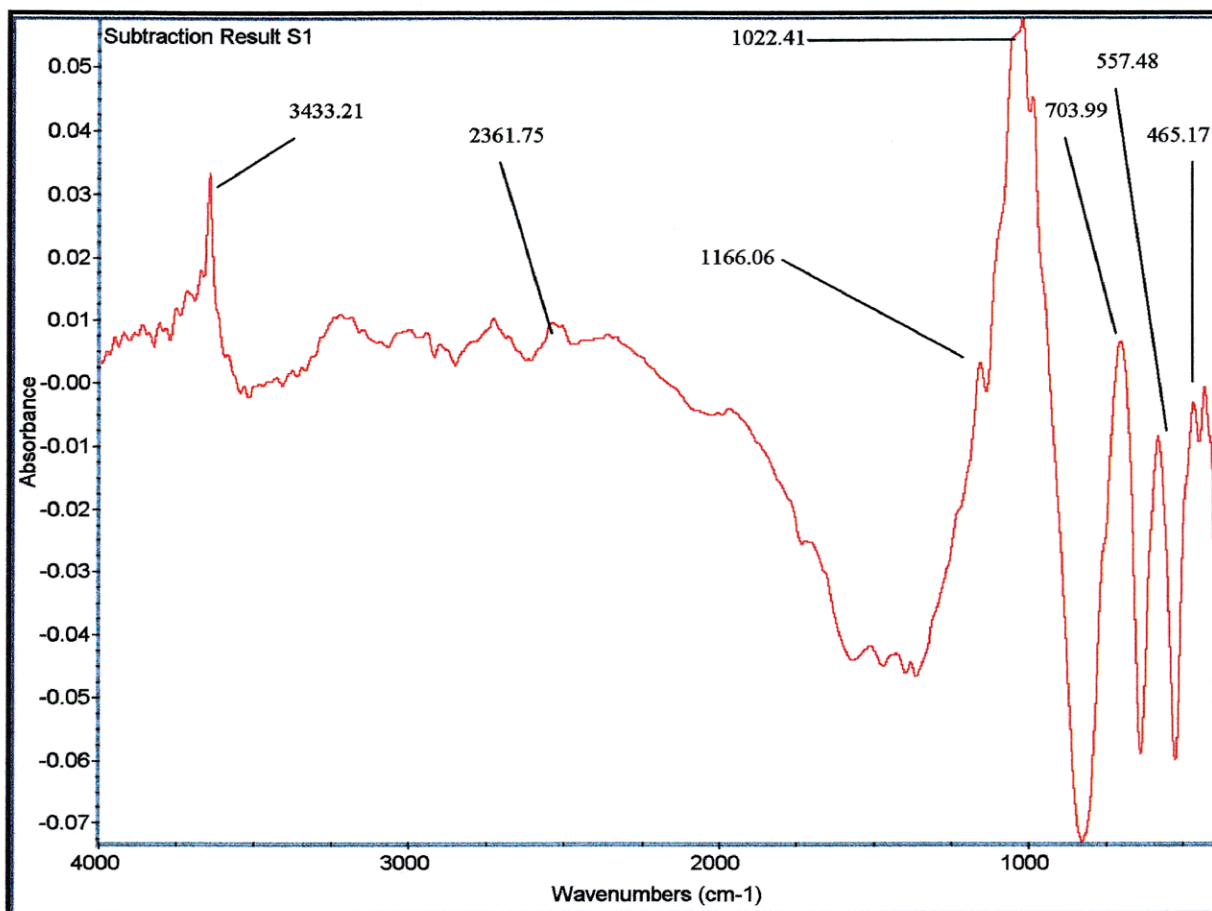


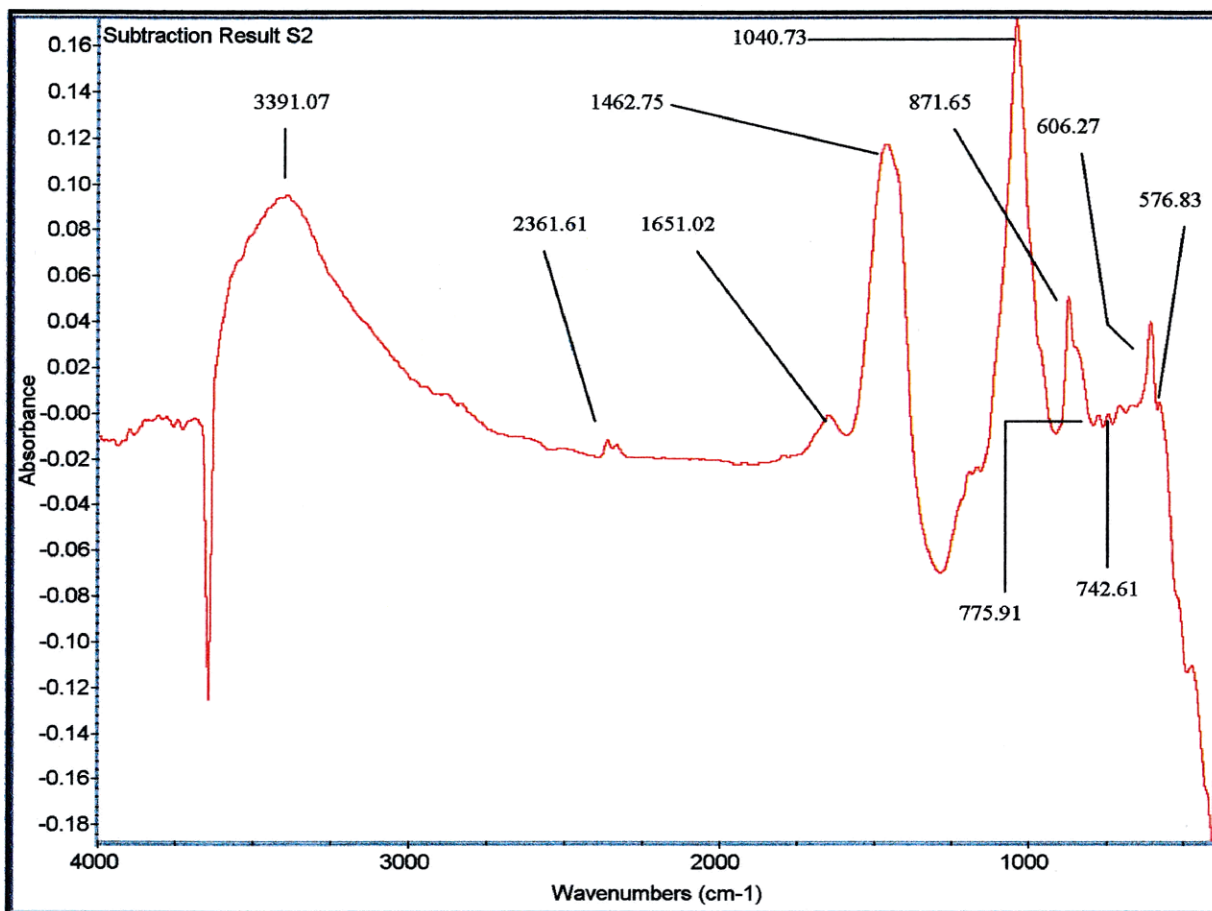
Bond Description	Phase Identified	S5 NT	S5 T	Subtracted S5
	$\alpha$ -TCP/CaO	3643.43	3433.21	3413.12
	Hydrocarbon			2918.07
	Hydrocarbon			2628.07
<b>CO<sub>2</sub></b>	<b>HCA</b>		<b>2361.37</b>	<b>2360.71</b>
<b>CO<sub>3</sub></b>	<b>HCA</b>			<b>2336.95</b>
<b>CO<sub>3</sub></b>	<b>HCA</b>		<b>1635.23</b>	<b>1635.25</b>
<b>CO<sub>3</sub></b>	<b>HCA</b>		<b>1456.44</b>	<b>1456.60</b>
<b>PO<sub>4</sub><sup>3-</sup> <math>\gamma</math>3 P-O anti-sym stretch</b>	$\alpha$ -TCP			1210.79
<b>PO<sub>4</sub><sup>3-</sup> <math>\gamma</math>3 P-O anti-sym stretch</b>	$\alpha$ -TCP			1158.74
<b>PO<sub>4</sub><sup>3-</sup> <math>\nu</math>3 P-O anti-sym stretch</b>	<b>HA</b>	<b>1035.78</b>	<b>1037.49</b>	<b>1045.22</b>
<b>PO<sub>4</sub><sup>3-</sup> <math>\gamma</math>1 P-O sym stretch</b>	$\beta$ -TCP	1124.24	1123.03	
<b>PO<sub>4</sub><sup>3-</sup> <math>\gamma</math>1 P-O sym stretch</b>	$\beta$ -TCP			
<b>CO<sub>3</sub></b>	<b>HCA</b>			873.48
	[?]			799.87
	[?]			667.68
<b>PO<sub>4</sub><sup>3-</sup> <math>\gamma</math>4 P-O anti-sym bend</b>	<b>HCA</b>	<b>601.19</b>	<b>601.53</b>	<b>601.87</b>
<b>PO<sub>4</sub><sup>3-</sup> <math>\gamma</math>4 P-O anti-sym bend</b>	$\beta$ -TCP			572.42
<b>PO<sub>4</sub><sup>3-</sup> <math>\gamma</math>4 P-O anti-sym bend</b>	$\beta$ -TCP	557.02	557.48	527.15
<b>O-P-O Deformation</b>		416.7	413.96	

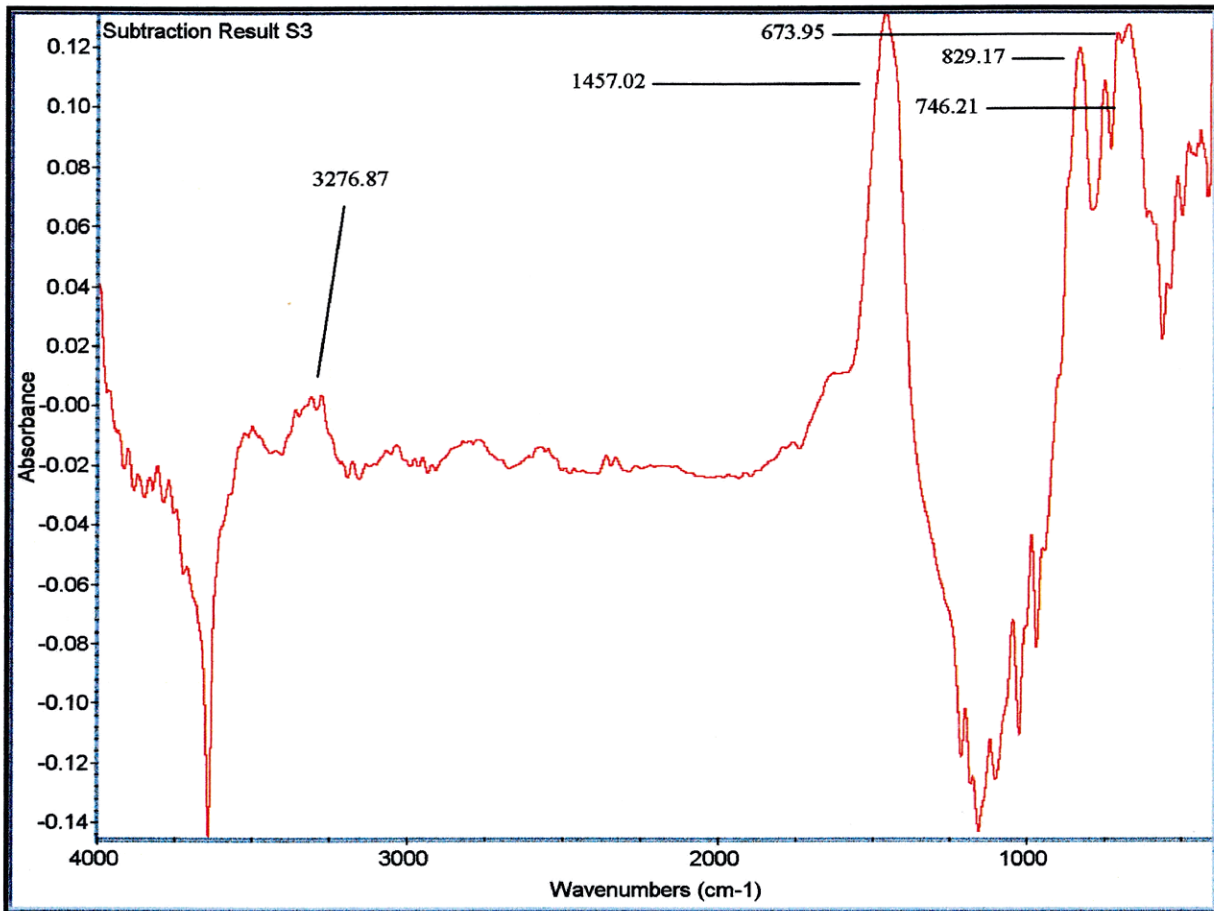


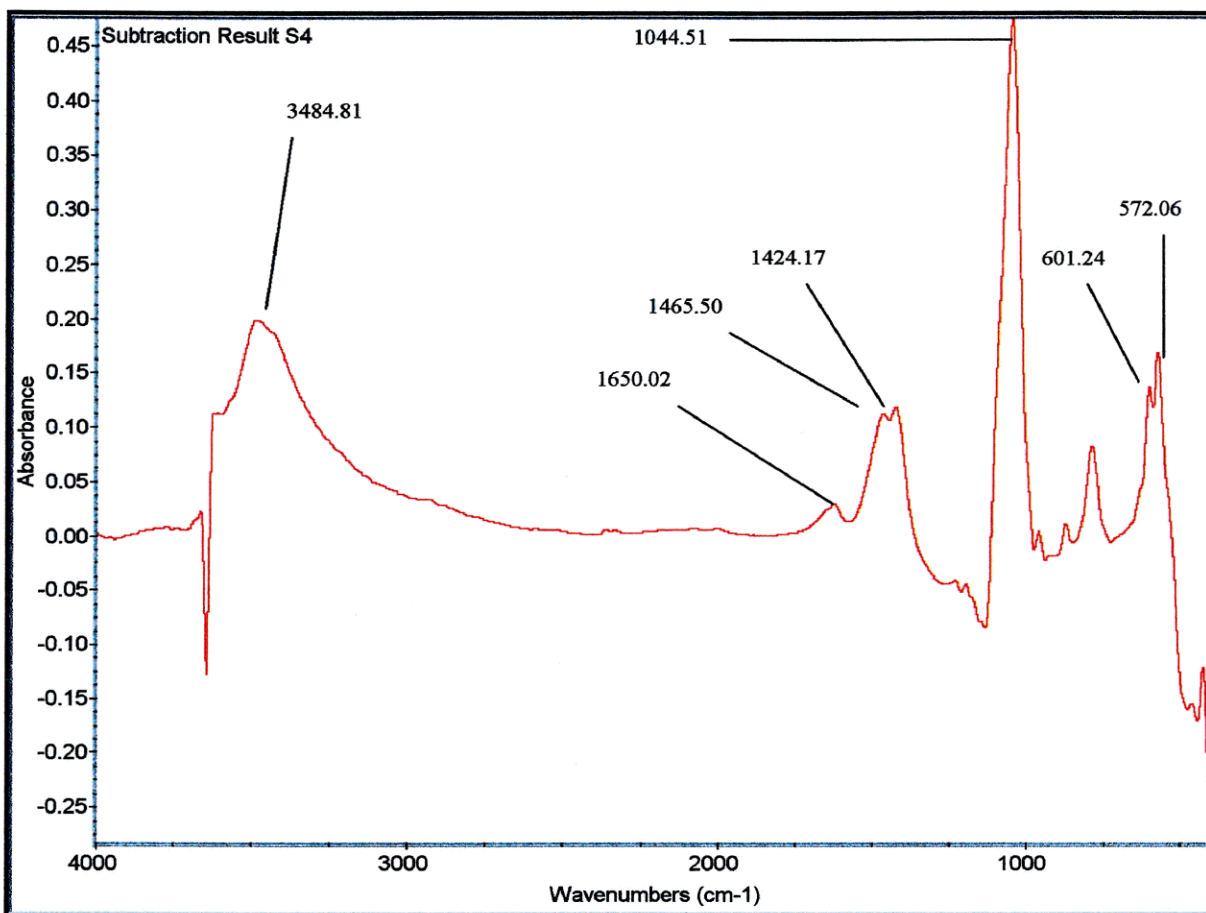


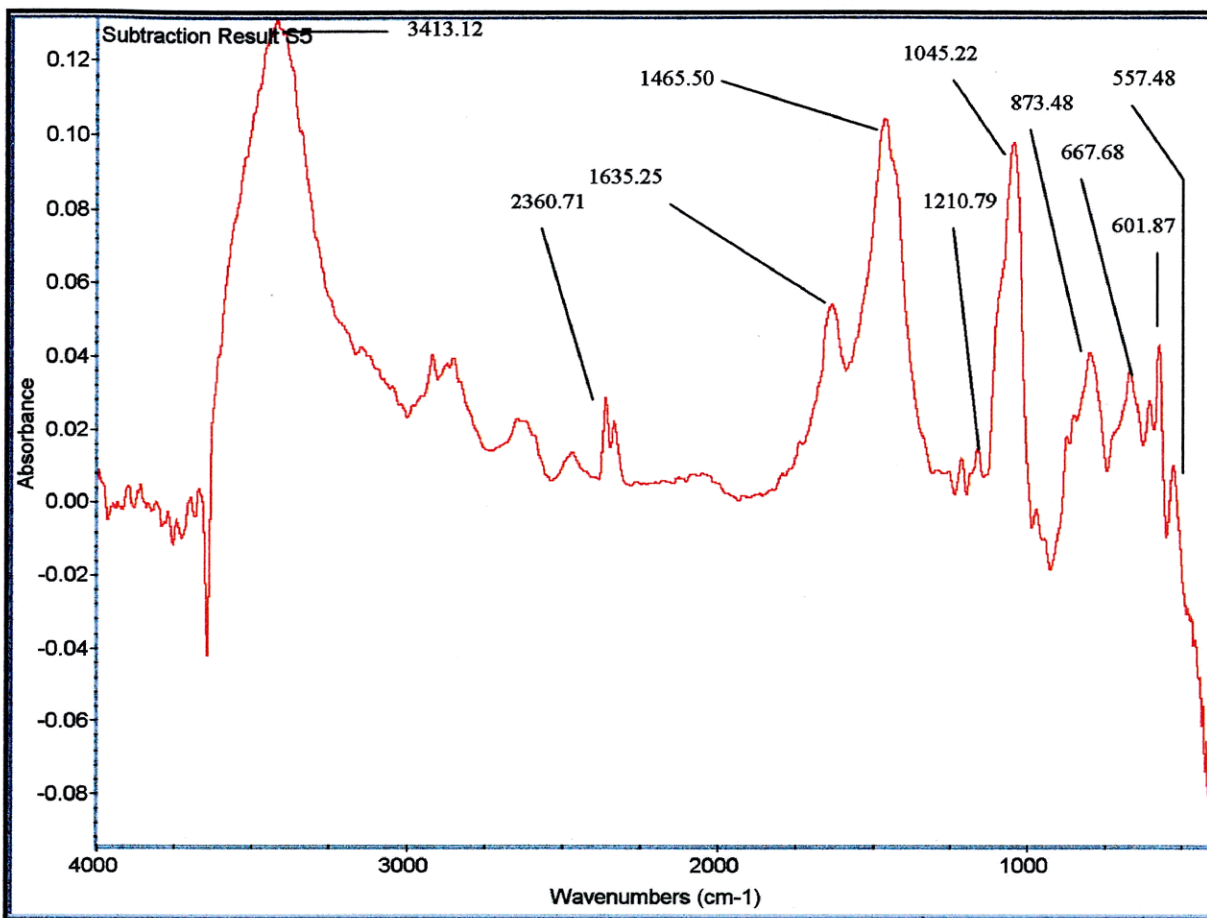


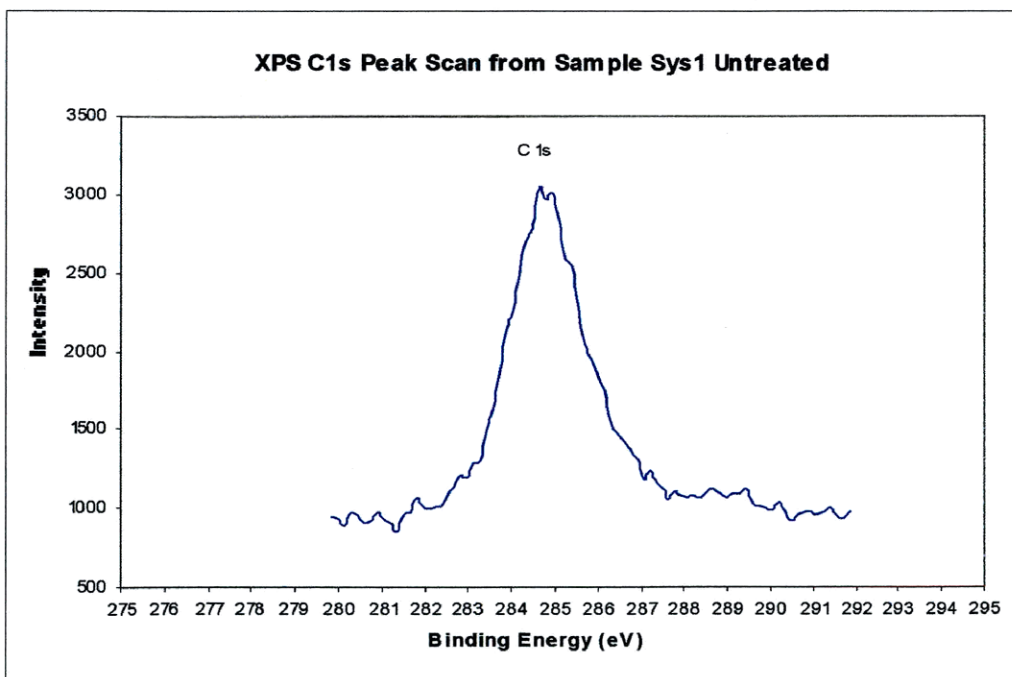
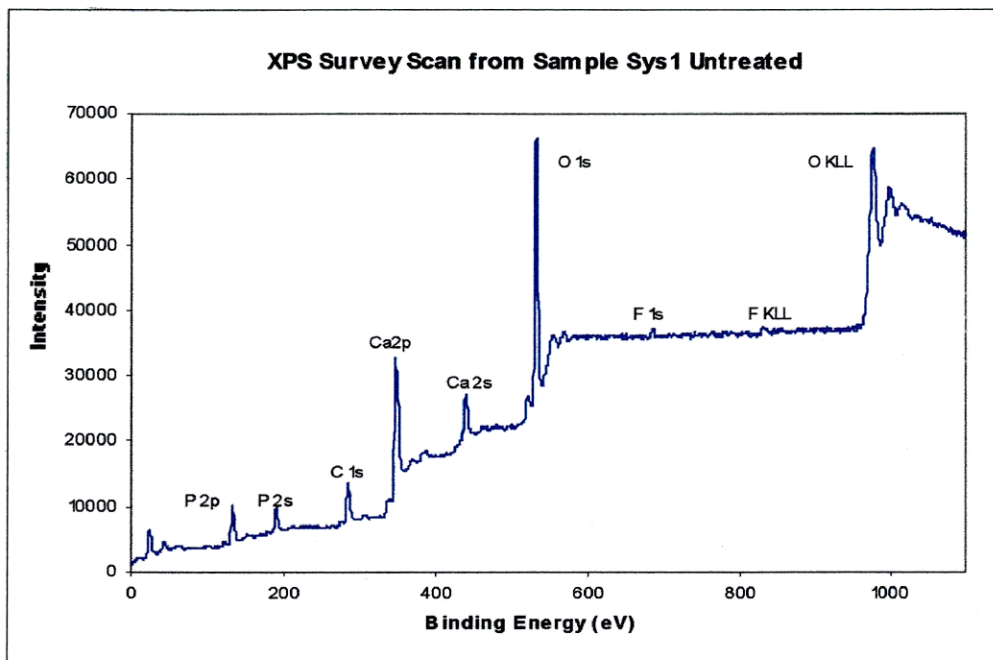
**SUBTRACTED SPECTRA**



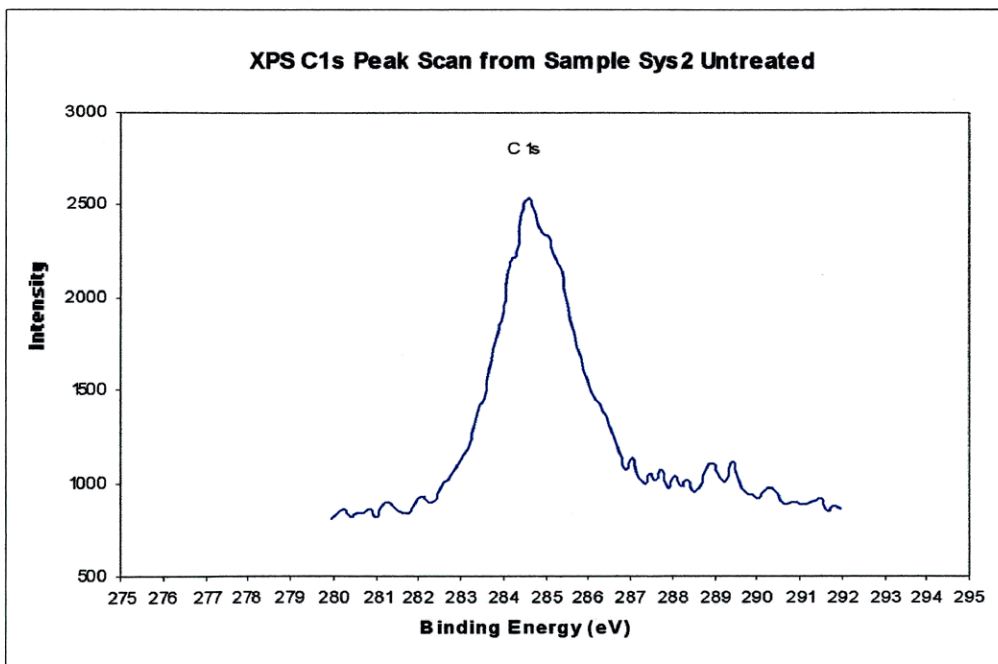
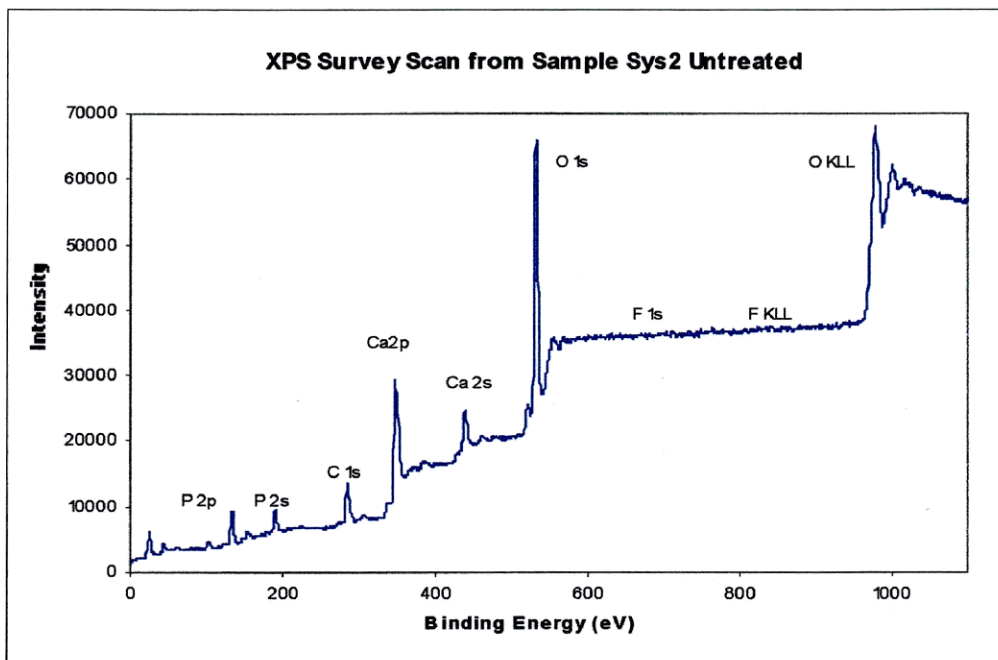


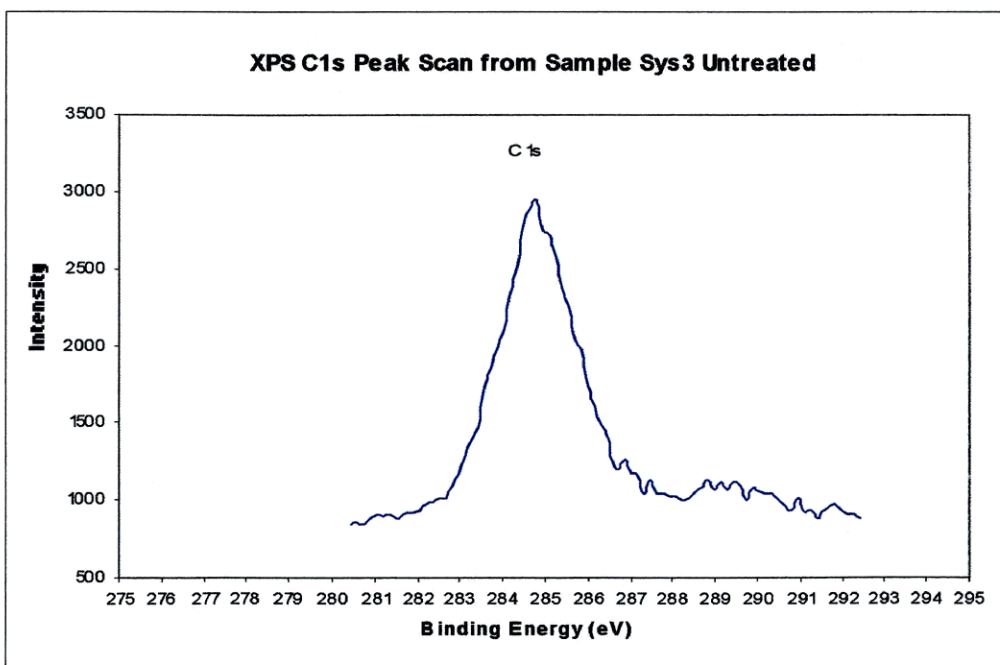
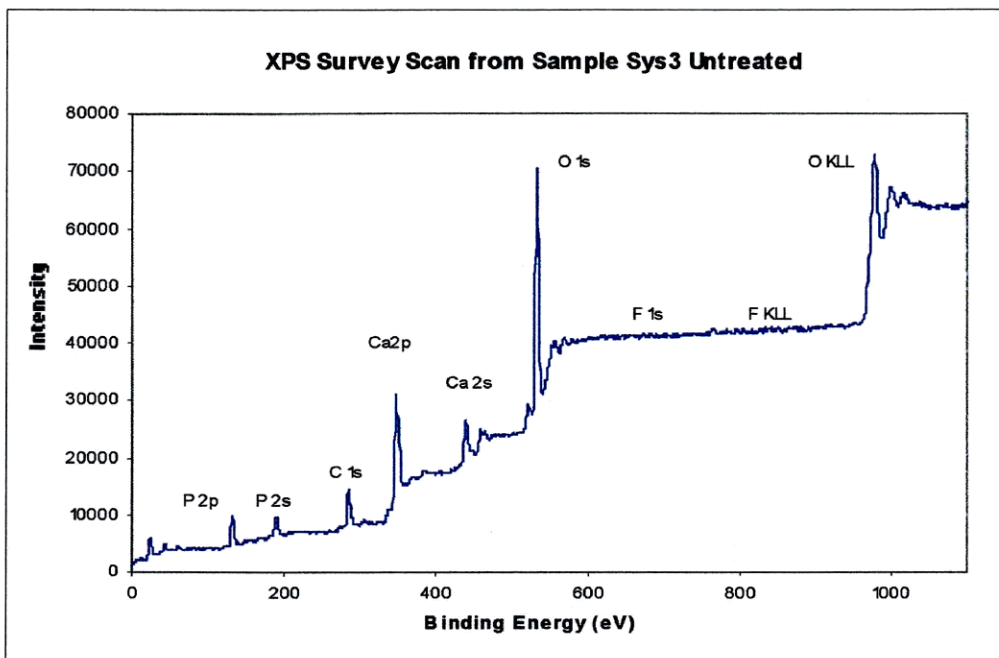


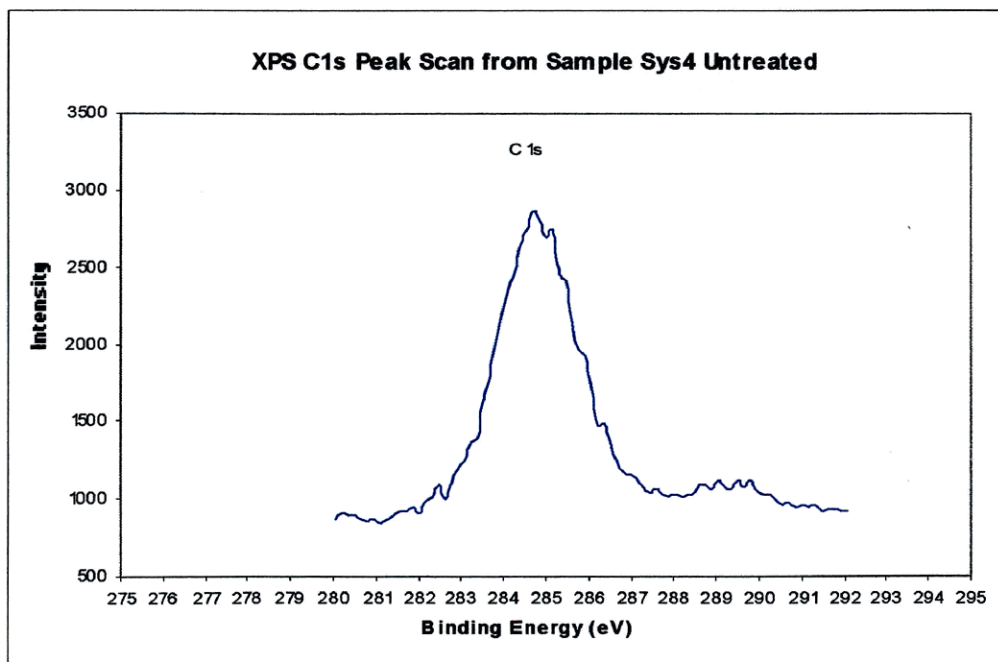
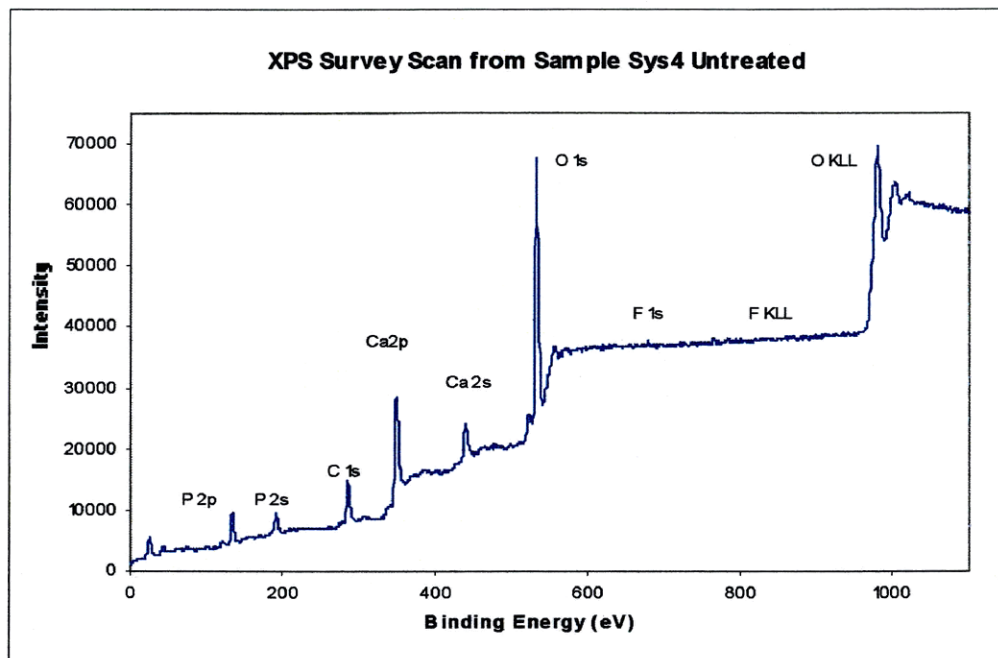


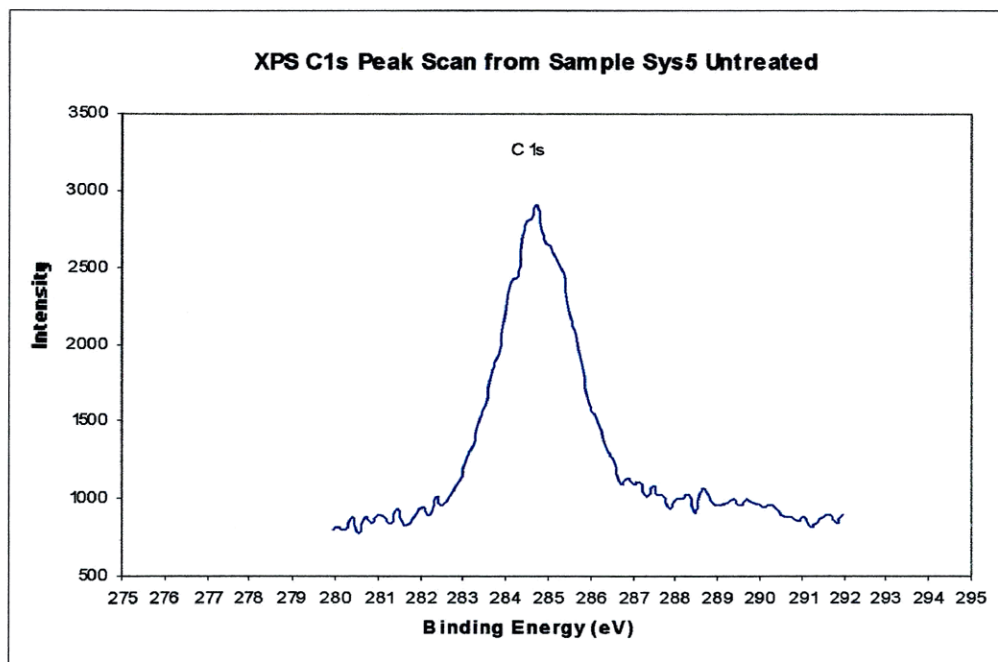
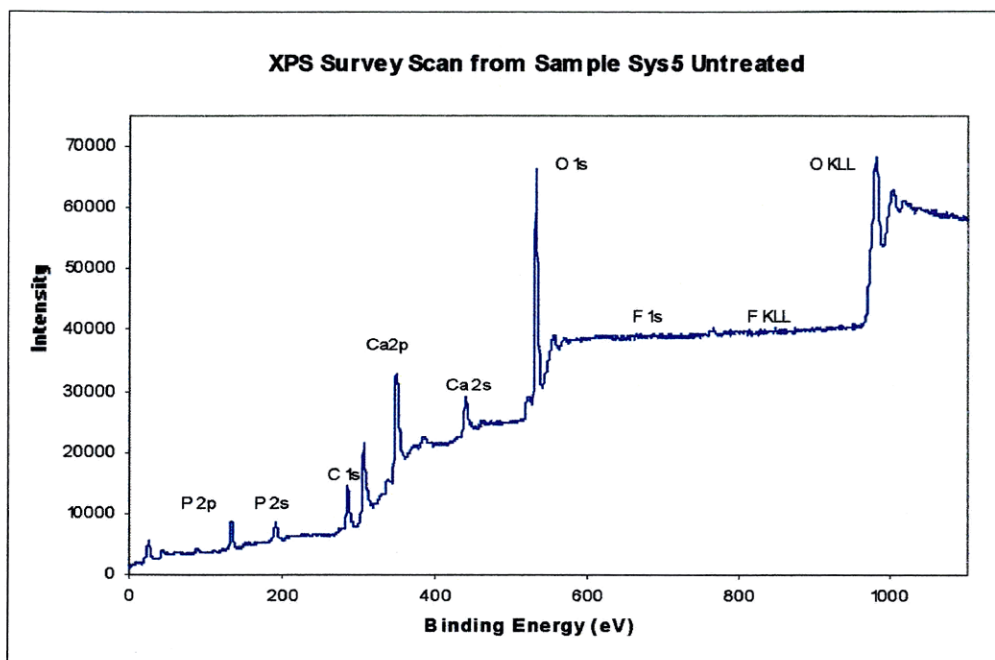
**APPENDIX 4 – XPS DATA**

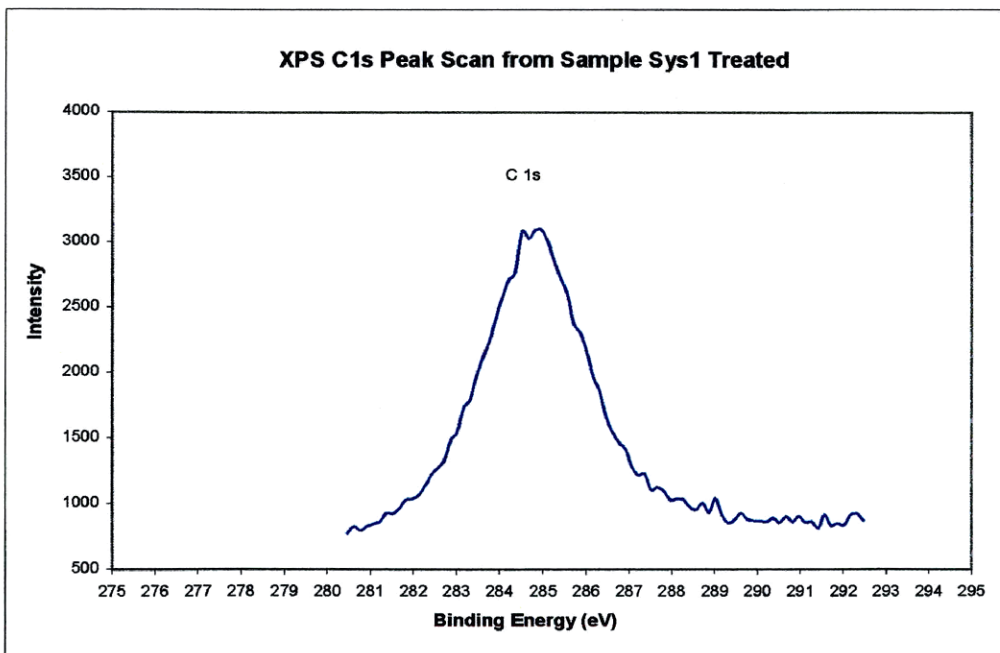
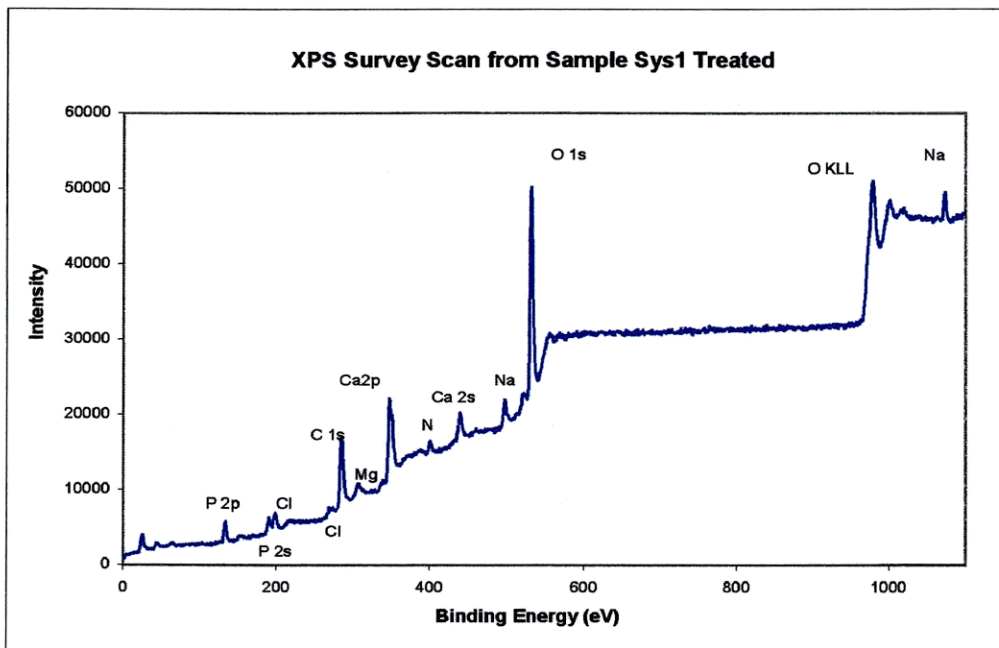


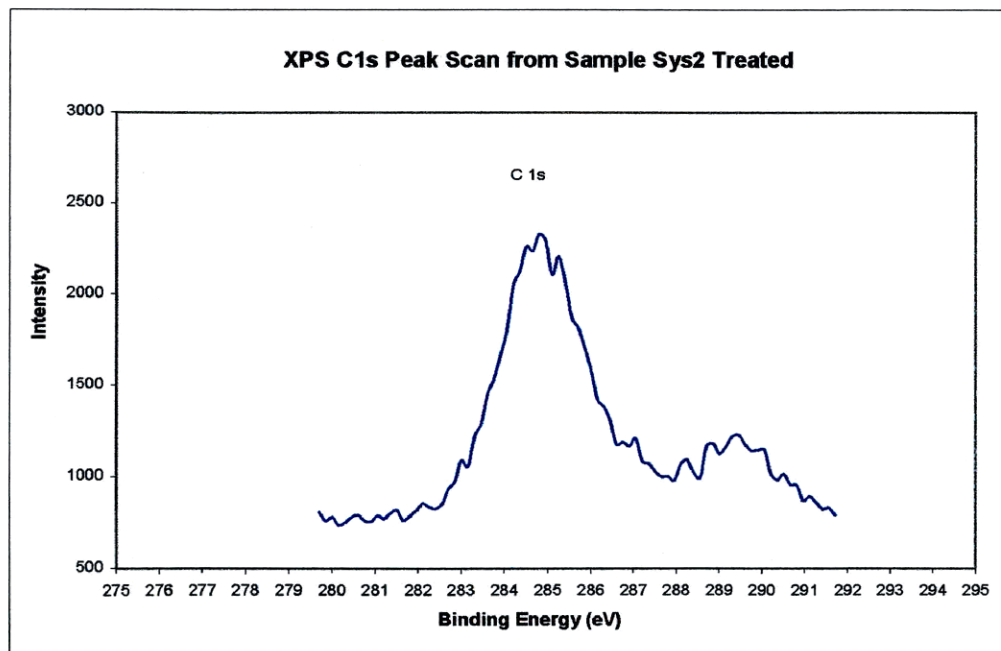
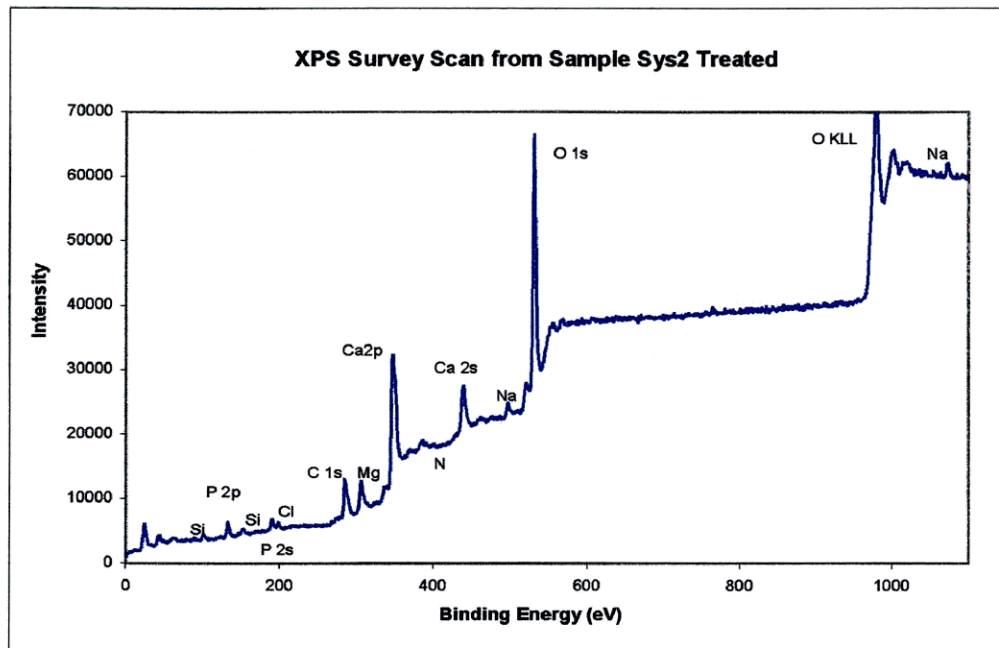


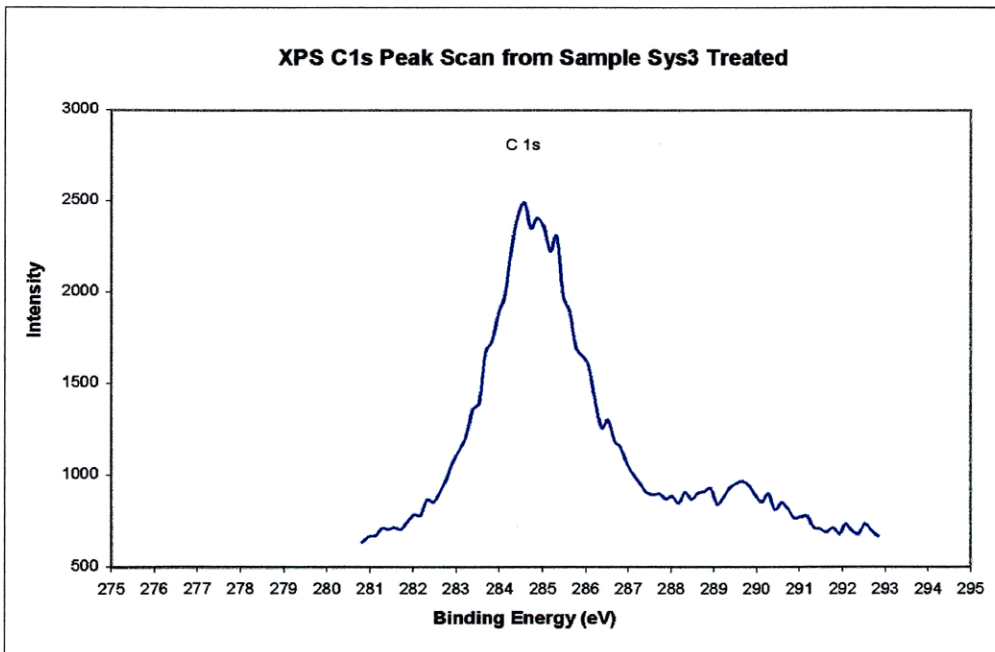
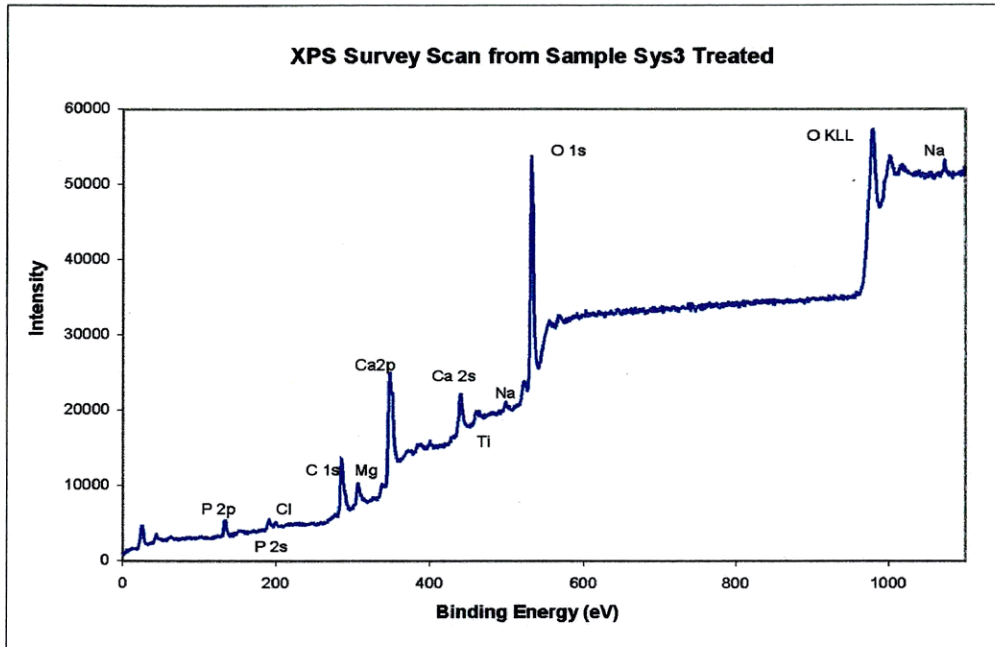


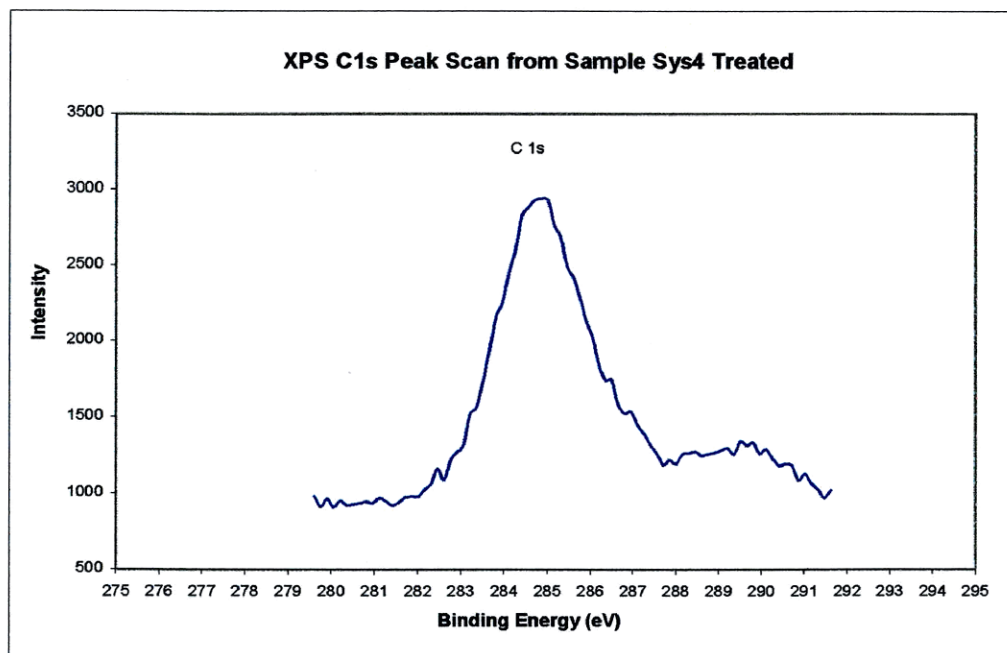
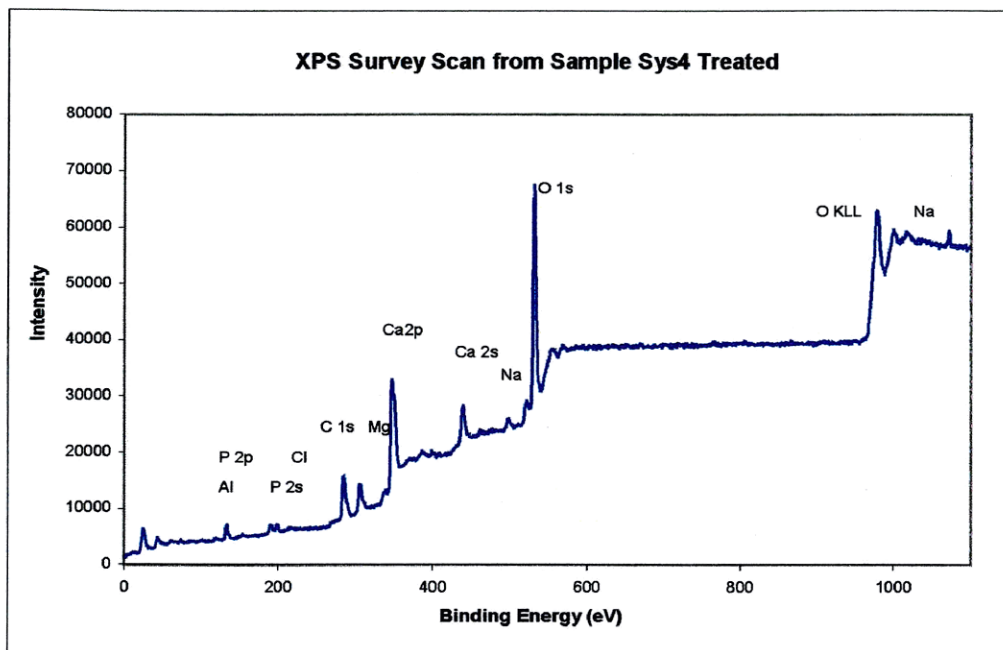




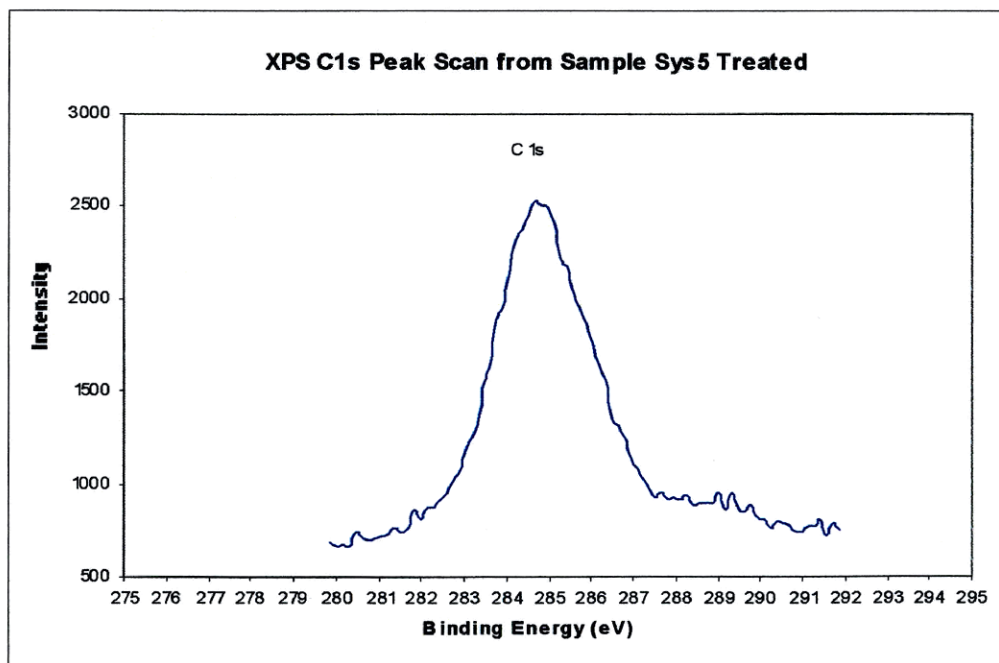
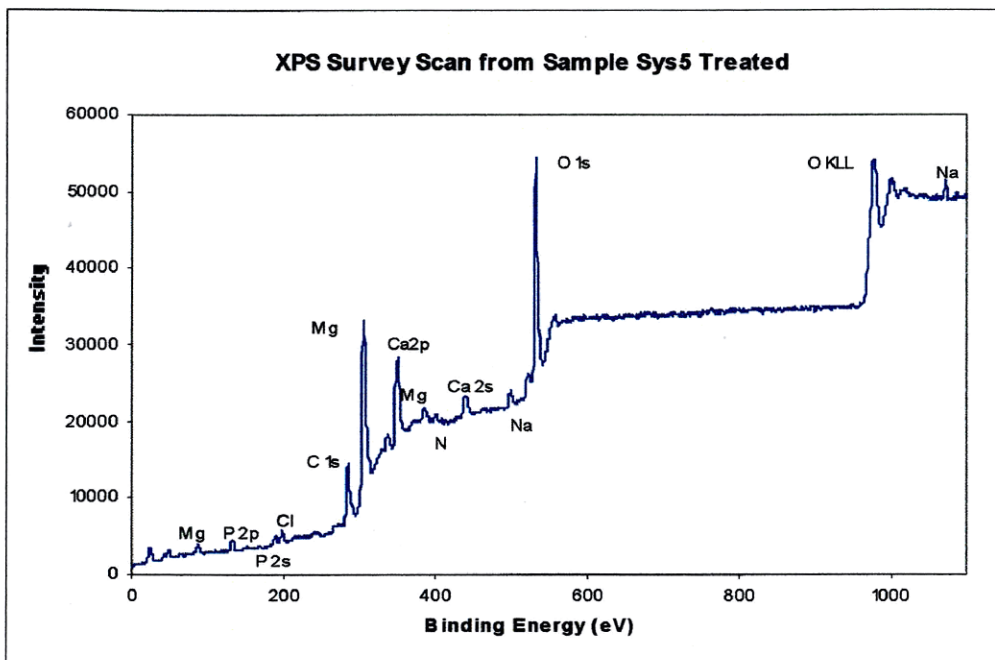












## APPENDIX 5 – ICP DATA

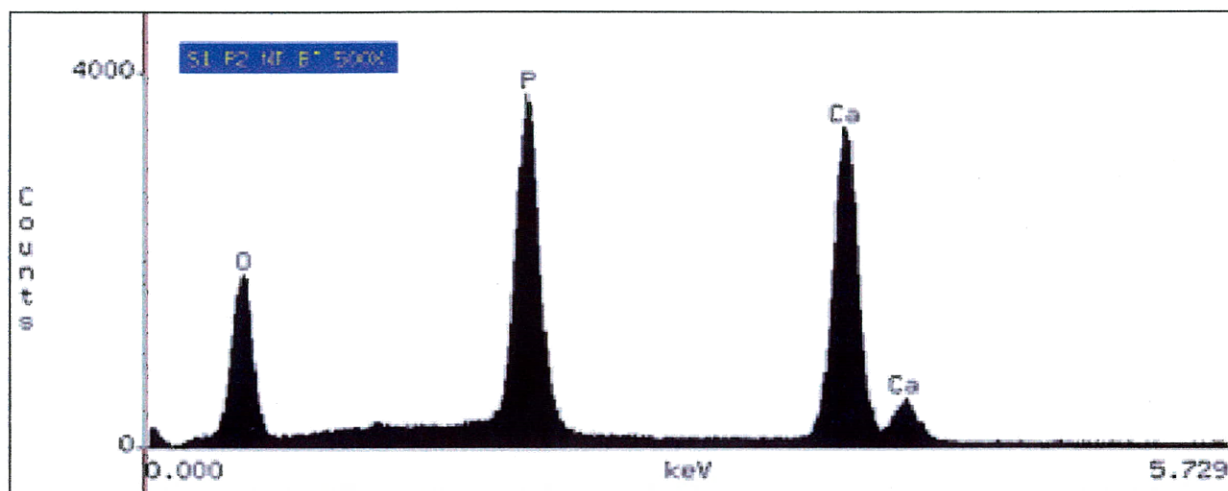
Detection Limits		SBF2	S1P1B SBF2/Dry	S2P1B SBF2/Dry	S3P1B SBF2/Dry	S4P1B SBF2/Dry	S5P1B SBF2/Dry
		0.00338373	1.051705742	1.03073724	1.009150545	1.018152426	0.98648651
0.002691394	<b>Analyte Name</b>	BDL	0.00471808	BDL	0.003137789	BDL	BDL
0.022581326	<b>Sc 361.383</b>	0.877467978	0.042017413	0.036806889	0.058953624	1.053681242	0.05805197
0.047247974	<b>Ag 328.068</b>	BDL	BDL	BDL	BDL	BDL	BDL
0.009257666	<b>Al 308.215</b>	0.029582341	0.04604378	BDL	BDL	BDL	BDL
0.004283973	<b>As 193.696</b>	BDL	0.034513704	0.035752787	0.038701365	0.025645184	0.025041568
0.000243001	<b>B 249.772</b>	0.063750079	BDL	BDL	BDL	BDL	BDL
0.005721125	<b>Ba 455.403</b>	0.01745487	13.59989059	97.81806626	120.3863991	89.24031544	53.26033903
0.001755139	<b>Be 313.107</b>	BDL	BDL	BDL	BDL	BDL	BDL
0.007200193	<b>Ca 317.933</b>	85.29810541	BDL	BDL	BDL	BDL	BDL
0.003261559	<b>Cd 214.440</b>	BDL	BDL	BDL	0.003977726	0.003325287	BDL
0.001366042	<b>Co 228.616</b>	BDL	0.180090986	0.060534587	0.048251727	0.030054075	0.043935603
0.003559353	<b>Cr 205.560</b>	BDL	0.035217352	BDL	0.007123044	BDL	BDL
0.0939912	<b>Cu 324.752</b>	0.138591139	61.29025266	54.16976686	91.45394534	42.25240977	71.29548378
0.001531683	<b>Fe 238.204</b>	0.011760147	0.007818518	0.009300406	0.009825225	0.005500356	0.005281188
0.000254975	<b>K 766.490</b>	302.6427059	1.453993913	4.256883031	6.521511987	3.289784045	Saturated
0.00061573	<b>Li 670.784</b>	0.076541772	0.015865589	0.001392359	0.001684632	0.000840785	0.001583959
0.003034853	<b>Mg 279.553</b>	19.48171053	0.003758389	0.004046483	0.003058496	BDL	BDL
0.012906007	<b>Mn 257.610</b>	Saturated	206.908511	Saturated	Saturated	417.738978	Saturated
0.002731302	<b>Mo 202.031</b>	0.021817389	0.006161381	0.004200325	0.005408628	0.003022921	0.005210204
0.044043248	<b>Na 589.592</b>		14.43005747	2.77545574	11.24639102	3.859091553	4.929220353
0.019596321	<b>Ni 231.604</b>	0.01190983	BDL	BDL	BDL	BDL	BDL
0.042776151	<b>P 177.434</b>	72.17220643	0.981237486	2.797558829	2.446062485	1.688562617	1.691038355
0.024548701	<b>Pb 220.353</b>	BDL	BDL	BDL	BDL	BDL	BDL
0.036018906	<b>S 180.669</b>	2.068581656	BDL	BDL	BDL	BDL	BDL
0.049269473	<b>Sb 217.582</b>	BDL	3.110926859	6.096855442	2.622845478	0.623439814	0.594538553
0.032898569	<b>Se 196.026</b>	BDL	BDL	0.034877886	BDL	BDL	BDL
0.000191509	<b>Si 251.611</b>	0.385773985	0.009820874	0.051733008	0.058130428	0.03876067	0.021700182
0.000505391	<b>Sn 189.927</b>	0.04177712	0.003275189	BDL	0.462487973	0.016026885	BDL
0.001254602	<b>Sr 421.552</b>	0.061969428	BDL	BDL	0.001418502	BDL	BDL
0.00112579	<b>Ti 334.940</b>	BDL	0.493369381	0.023895801	0.037643647	0.022316976	0.030556985
	<b>V 292.402</b>	BDL	0	0	0	0	0





## APPENDIX 6 – EDS DATA

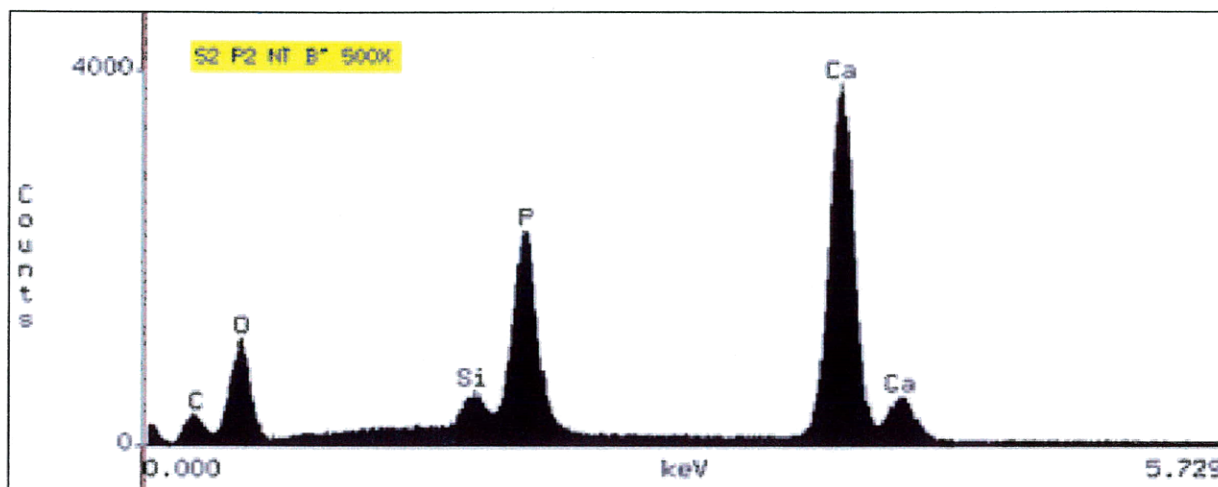
## S1 P2 NT B' 500x



## S1 P2 NT B' Data

Element	k-ratio (calc.)	ZAF	Atom %	Element Wt %	Wt % Err. (1-Sigma)
P -K	0.3142	1.075	39.78	33.79	+/- 0.36
Ca-K	0.6291	1.052	60.22	66.21	+/- 0.43
Te-L	0.0000	1.352	0.00	0.00	+/- 0.00
Total			100.00	100.00	

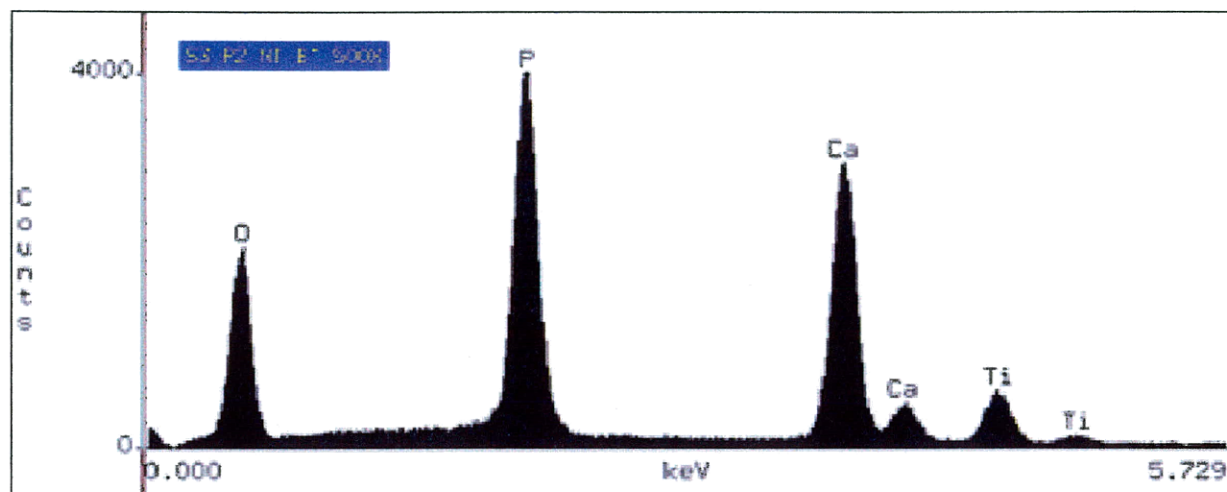
## S2 P2 NT B' 500x



## S2 P2 NT B' Data

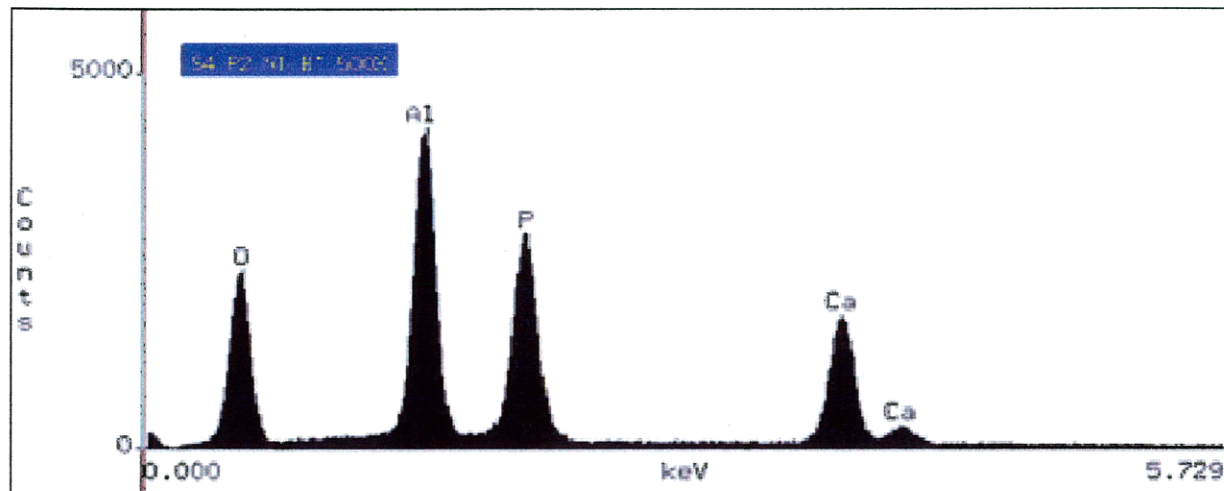
Element	k-ratio (calc.)	ZAF	Atom %	Element Wt %	Wt % Err. (1-Sigma)
Si-K	0.0279	1.118	4.14	3.13	+/- 0.11
P -K	0.1965	1.109	26.18	21.80	+/- 0.34
Ca-K	0.7228	1.039	69.68	75.08	+/- 0.66
Total			100.00	100.00	



**S3 P2 NT B' 500x****S3 P2 NT B' Data**

Element	k-ratio (calc.)	ZAF	Atom %	Element Wt %	Wt % Err. (1-Sigma)
P -K	0.3076	1.075	39.94	33.05	+/- 0.34
Ca-K	0.4942	1.028	47.46	50.83	+/- 0.50
Te-L	0.0000	1.328	0.00	0.00	+/- 0.00
Ti-K	0.1324	1.218	12.60	16.12	+/- 0.26
Total			100.00	100.00	

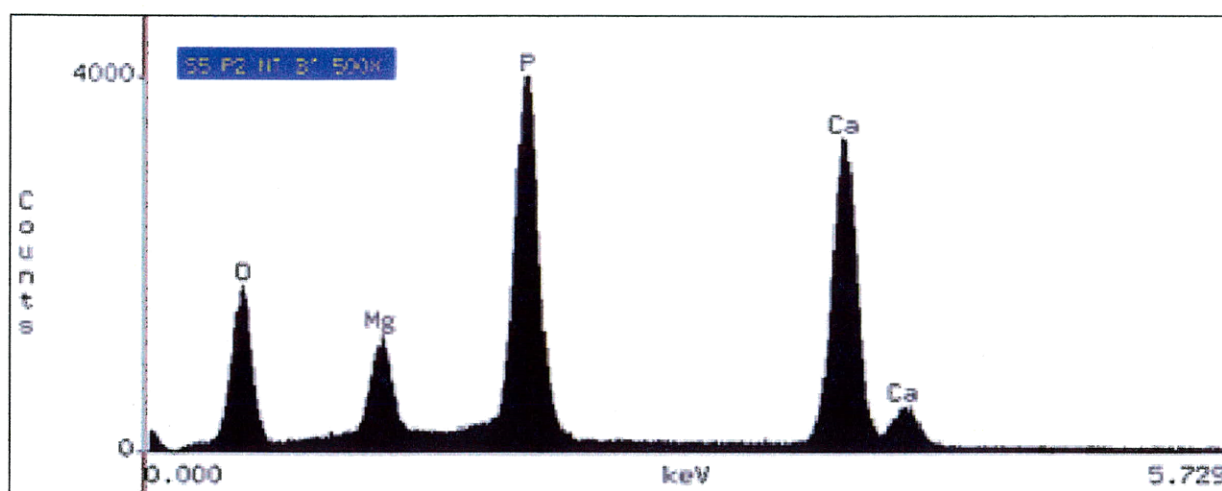
## S4 P2 NT B' 500x



## S4 P2 NT B' Data

Element	k-ratio (calc.)	ZAF	Atom %	Element Wt %	Wt % Err. (1-Sigma)
Al-K	0.2870	1.149	39.19	32.99	+/- 0.25
P -K	0.2533	1.259	33.01	31.89	+/- 0.36
Ca-K	0.3173	1.090	27.67	34.59	+/- 0.33
Te-L	0.0038	1.398	0.13	0.53	+/- 1.02
Total			100.00	100.00	

## S5 P2 NT B' 500x

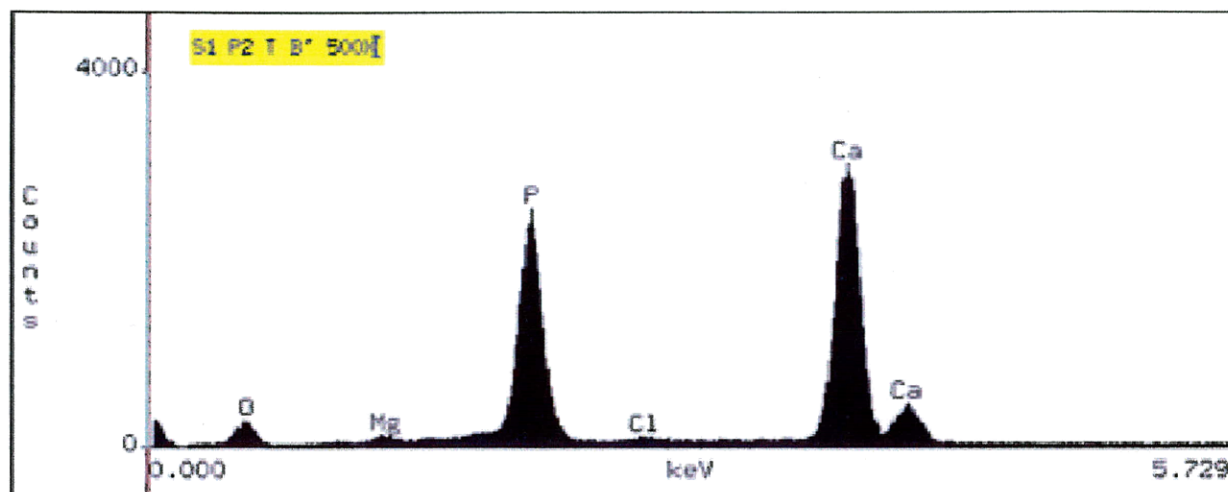


## S5 P2 NT B' Data

Element	k-ratio (calc.)	ZAF	Atom %	Element Wt %	Wt % Err. (1-Sigma)
Mg-K	0.0618	1.395	12.29	8.62	+/- 0.17
P -K	0.3065	1.115	38.23	34.17	+/- 0.34
Ca-K	0.5372	1.065	49.48	57.22	+/- 0.52
Te-L	0.0000	1.364	0.00	0.00	+/- 0.00
Total			100.00	100.00	

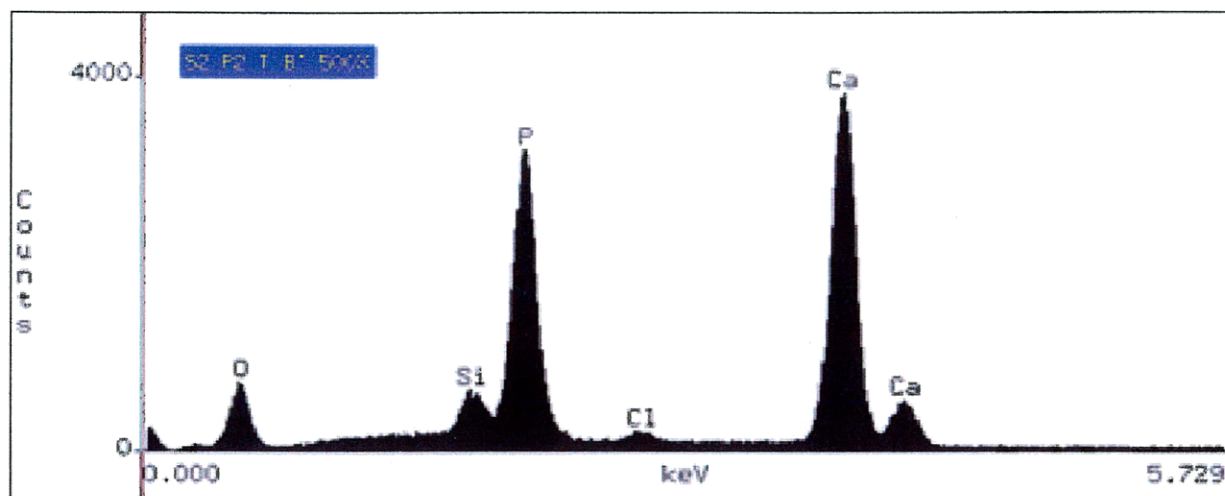


## S1 P2 T B' 500x



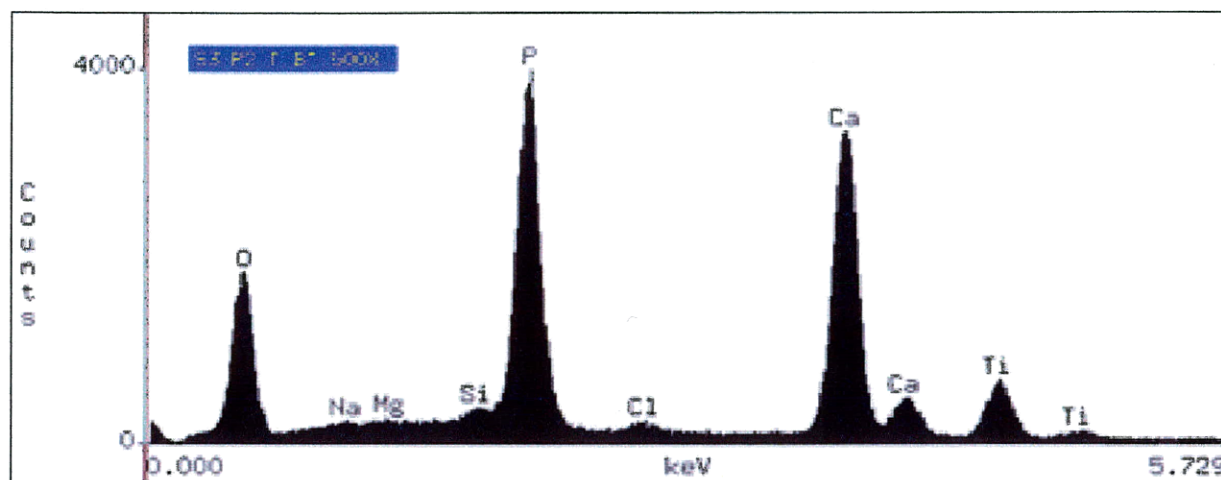
## S1 P2 T B' Data

Element	k-ratio (calc.)	ZAF	Atom %	Element Wt %	Wt % Err. (1-Sigma)
Mg-K	0.0037	1.485	0.84	0.55	+/- 0.11
P -K	0.2573	1.085	33.49	27.91	+/- 0.32
Ca-K	0.6766	1.042	65.36	70.48	+/- 0.80
Te-L	0.0079	1.339	0.31	1.06	+/- 1.44
Total			100.00	100.00	

**S2 P2 T B' 500x****S2 P2 T B' Data**

Element	k-ratio (calc.)	ZAF	Atom %	Element Wt %	Wt % Err. (1-Sigma)
Si-K	0.0348	1.101	4.98	3.83	+/- 0.23
P -K	0.2507	1.107	32.65	27.75	+/- 0.39
Cl-K	0.0119	1.153	1.41	1.37	+/- 0.09
Ca-K	0.6373	1.052	60.97	67.05	+/- 0.57
Te-L	0.0000	1.350	0.00	0.00	+/- 0.00
Total			100.00	100.00	

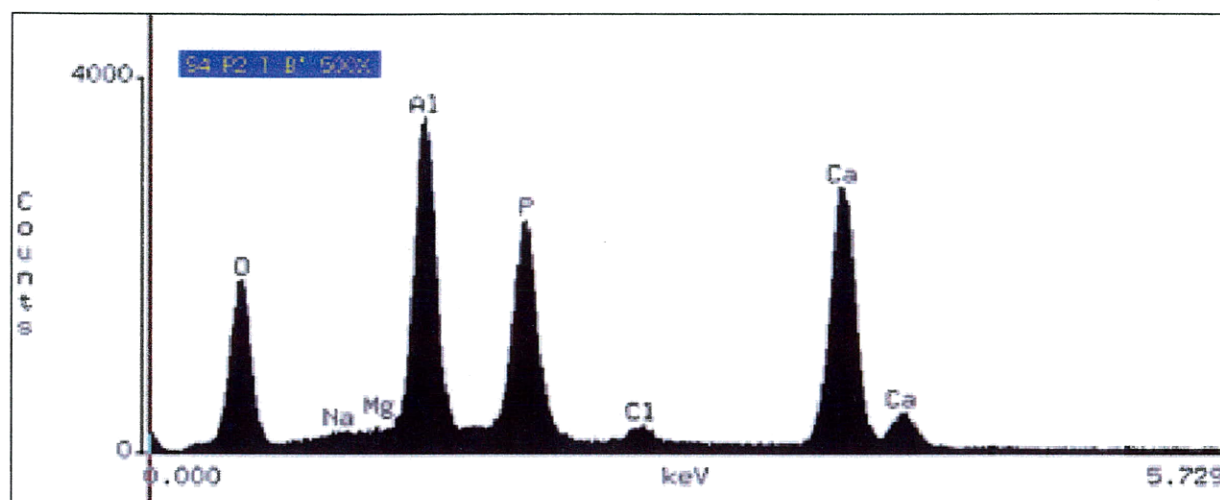
## S3 P2 T B' 500x



## S3 P2 T B' Data

Element	k-ratio (calc.)	ZAF	Atom %	Element Wt %	Wt % Err. (1-Sigma)
Na-K	0.0019	1.993	0.63	0.39	+/- 0.09
Si-K	0.0056	1.107	0.83	0.62	+/- 0.08
P -K	0.2685	1.082	35.26	29.07	+/- 0.32
Cl-K	0.0128	1.142	1.55	1.46	+/- 0.16
Ca-K	0.5117	1.027	49.24	52.54	+/- 0.49
Te-L	0.0000	1.325	0.00	0.00	+/- 0.00
Ti-K	0.1305	1.220	12.49	15.93	+/- 0.40
Total			100.00	100.00	

## S4 P2 T B' 500x

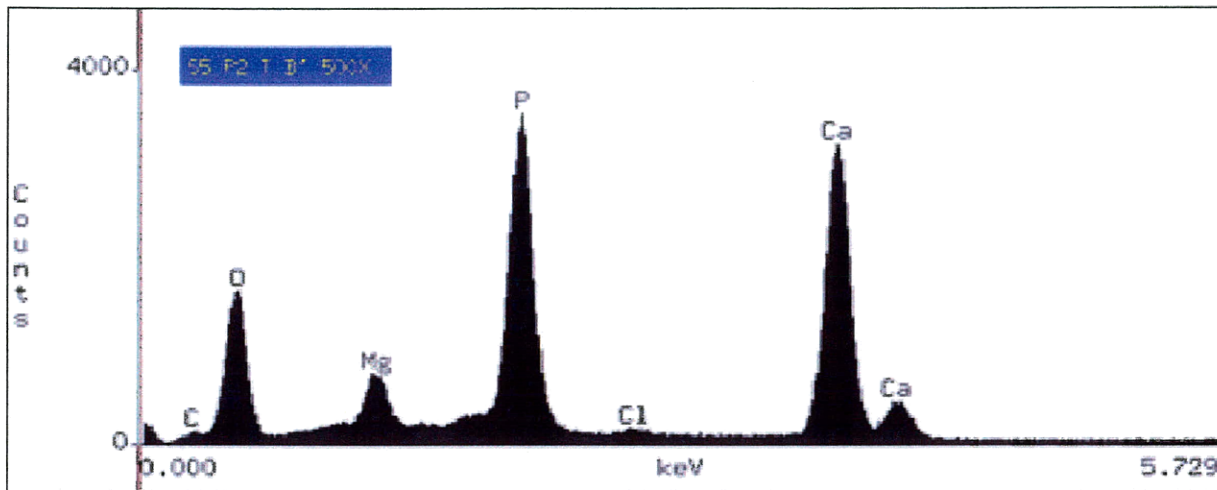


## S4 P2 T B' Data

Element	k-ratio (calc.)	ZAF	Atom %	Element Wt %	Wt % Err. (1-Sigma)
Al-K	0.2038	1.206	30.74	24.58	+/- 0.23
P-K	0.1820	1.218	24.16	22.17	+/- 0.29
Cl-K	0.0200	1.196	2.27	2.39	+/- 0.18
Ca-K	0.4760	1.069	42.83	50.86	+/- 0.50
Te-L	0.0000	1.366	0.00	0.00	+/- 0.00
Total			100.00	100.00	



## S5 P2 T B' 500x



## S5 P2 T B' Data

Element	k-ratio (calc.)	ZAF	Atom %	Element Wt %	Wt % Err. (1-Sigma)
Mg-K	0.0370	1.426	7.70	5.27	+/- 0.18
P -K	0.2936	1.101	37.04	32.32	+/- 0.28
Ca-K	0.5902	1.057	55.26	62.40	+/- 0.41
C -K	0.0000	5.461	0.00	0.00	+/- 0.01
Total			100.00	100.00	

## APPENDIX 7 – AFM DATA

